Nijaz Delić, moj otac.

“Freedom is by no means free.”

Madrugada

Acknowledgements

THANKS are gratefully offered to my supervisor Karina Mathisen for her well-informed scientific suggestions. Her courage and endurance with me was far beyond what I could possibly expect. Your rule is decisive but fair, Princess Leia.

I would like to thank Professor David Graham Nicholson for giving me the opportunity to write this thesis and achieve my Master of Science degree. His original thoughts on science and life in general have inspired a woman to forget her limits.

Utilization of the ESFR and Max-lab synchrotron facilities were financed by Norwegian University of Science and Technology and the Norwegian Research Council. Their contribution is greatly appreciated.

I am also grateful to Dr. Michael Stockenhüber and ELKEM Research, represented by Gunnar Schussler. I could not have carried out the NOx measurements at the University of Newcastle, Australia, without their support.

Jonas Alexander, will you marry me?

My beloved brother, Asmir, your unconditional care moves my heart and gives me comfort when no one else can.

I'm indebted to Syverin Lierhagen for giving me invaluable assistance with the ICP-MS analyses. Your spreadsheets are impossible to understand for a non-magician, but fortunately you were there to help me.

Kari and Gunnar, thank you for always being kind and for providing me with chemicals and all equipment needed for my experiments.

Anlaug, Beate, Inger Lise, Katrine, Mari N., Mari T., Solveig, Tina and Yngvil, thank you all for the cheer times.

Asmira Delić,

Trondheim, May 2009.

ABSTRACT

Transition metal ion-exchanged zeolites are promising heterogeneous catalyst in the selective reduction of NOx in presence of hydrocarbons (SCR-HC). Knowledge about the location and structure of the metal centers is of major importance to understand the catalytic potential of these materials. Both zeolites containing silver and zeolites containing copper are catalytically active for NO_x reduction, but insufficient for practical applications. The redox properties of copper-zeolites are attributed to their catalytic activity in the decomposition/reduction of NO_x, where the Cu(I) species participate in the reaction. A prerequisite for $deNO_x$ activity is stabilization of copper(I) within the structure, together with reversibility of the copper valence state.

In present work, characterization of copper cations in zeolite Y in presence and absence of silver cation has been performed. ICP-MS has been used to investigate how the weight percentages of the cations in the zeolite vary with different copper/silver solution ratios upon ion-exchange. The influence from silver ions on site occupation of copper in zeolite Y has been investigated by EXAFS. Reducibility of copper in presence and absence of copper has been studied by in-situ XAS. XRD and SEM were used to examine the stability and morphology of the zeolite before and after thermal treatments in reducing and oxidizing environments. Conversion of NO_x by the samples has also been measured.

Results show that varying the initial silver(I) nitrate/copper(II) nitrate solution ratio results in different silver/copper ratio in ion-exchanged zeolite Y. By simultaneous presence of silver cations in zeolite Y the immediate coordination of copper is changed, i.e. copper ions occupy different sites in zeolite Y. Upon thermal treatment in hydrogen, reduction of Cu(II) to Cu(I) occurs. The estimation Cu(I) fraction is larger when silver is present. This is attributed to the location of copper at sites more accessible to hydrogen. Exposing the samples to oxidizing environment (NO) after hydrogen treatment leads to formation of copper oxides, more so when silver is present than absent. In the sample with only copper, a larger fraction of reversed Cu(II) is found. The structure and particle size distribution of zeolite Y is unaffected of thermal treatment in reducing and oxidizing environments.

$deNO_x$ measurements show that the co-cation effect does not improve catalytic activity towards NO_x reduction. Conversion of NO_x is very poor both when silver is present and absent.

CONTENTS

PART I

THEORETICAL BACKGROUND AND THE RESEARCH QUESTION

1 INTRODUCTION

This thesis is on characterization of copper in ion-exchanged zeolite Y in presence and absence of silver cations, and the co-cation in relation to catalytic activity upon NO_x reduction. In the following sections an introduction to zeolites is given, with special attention on zeolite Y. Why zeolites are important in catalysis regarding reduction of NO_x is also explained. Based on these theories, in section 1.3 the research questions are defined and explained.

1.1 A Brief introduction to zeolites [1, 2]

Zeolites have been defined by Smith [1] as a "crystalline aluminosilicates with tetrahedral framework structure enclosing cavities occupied by cations and water molecules, both which have enough freedom of movement to permit cation exchange and reversible dehydration". While many naturally occurring zeolites are known, even more zeolites, with controlled structures and high purity, are made synthetically. Because of the widespread use of zeolites for industrial applications, the name zeolite is now fairly well known. Properties making them attractive as hosts for catalytically active species are ion exchange ability, high exchange capability, crystalline structure with regular pores of molecular size, thermal stability and low cost.

1.1.1 General composition and structure of zeolites

The fundamental building unit of all zeolites is a silicon or aluminium ion surrounded by four oxygen anions, i.e. a tetrahedron (Figure 1.1). The tetrahedra are arranged so that each of the oxygen ions, called bridging ions, is shared between neighbouring silicon or aluminium tetrahedra. The resulting crystal lattice extends in three-dimension. The silica tetrahedra are electrically neutral since each silicon ion has its +4 charge balanced by the four surrounding oxygens. Each alumina tetrahedra has a residual charge of –1 because of the trivalent aluminium, and therefore requires a +1 charge from a cation to remain electrically neutral. When manufactured, these cations are usually sodium or protons, which can easily be replaced by other type of cations by ion exchange.

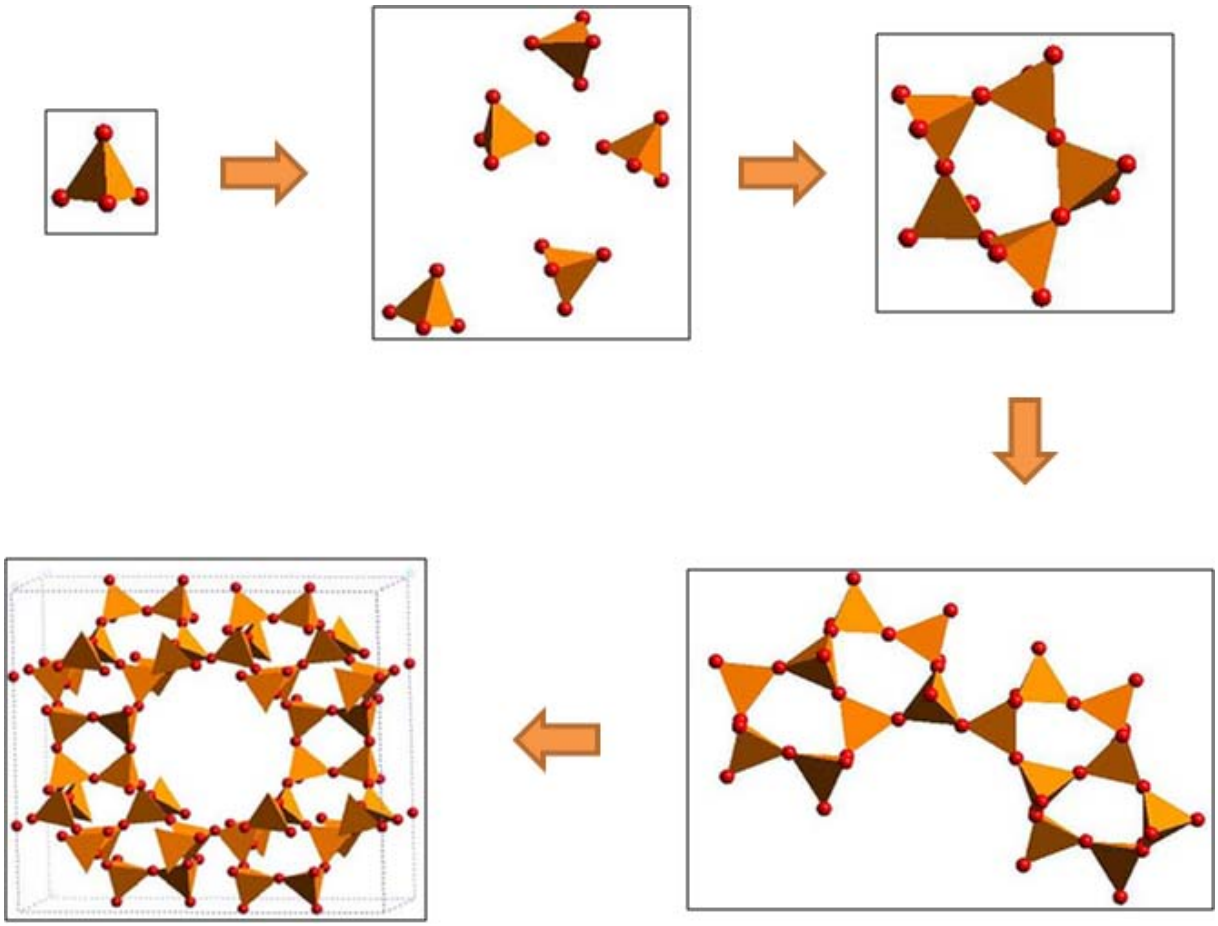

Figure 1.1 Building of zeolites – from tetrahedra to full framework [3].

1.1.2 Zeolite Y (Faujasite) [1, 4, 5, 6]

The chemical formula for zeolite Y is $|(Ca^{2+},Mg^{2+}Na^{+}{}_2)_{29}\ (H_2O)_{240}|$ **[**$Al_{58}Si_{134}\ O_{384}$**]. S**odalite units with hexagonal prisms are connected to four other sodalite units by six bridging oxygen ions. This structure gives a framework characterized by large, empty cavities (supercages), as shown in Figure 1.2. The six-membered oxygen rings of the sodalite cages have a diameter of 2.6 Å, while the void itself is 6.6 Å in diameter. Only small molecules, such as water and hydrogen can enter the sodalite cages. The interior supercage can be entered via twelve-membered rings. The diameter of the supercage itself is 12 Å.

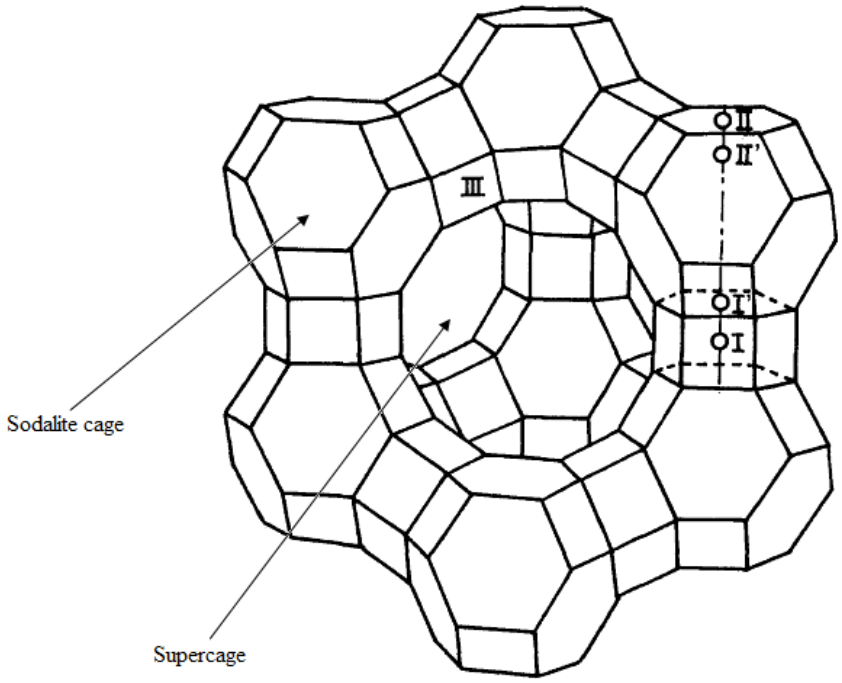

Figure 1.2 Framework of Zeolite [7].

Within zeolite Y, cations may be located at well-defined sites named I, I', II, II', and III (Figure 1.2). In the six-membered ring between sodalite cages three of the oxygen atoms (O_A) are bent inwards and three outwards (O_B) (Figure 1.3 a)). Cations located at site I are found in the centre of the hexagonal prism (Figure 1.3 b)). They have an octahedral coordination environment by binding with the three oxygen atoms O_A of the two six-membered ring base planes. The adjacent I' site, is one of the base planes of the hexagonal prism. Cations at this site are three-coordinated (Figure 1.3 a)). Site II is the hexagonal border between the sodalite and supercharge. Cations located at this site are also are three-coordinated. So are the cations at the adjacent II' site. Cations situated in site III are coordinated to four oxygen atoms (Figure 1.3 c)). This site is closest to supercharge, located at its walls. Simultaneous occupation of adjacent sites is forbidden due to repulsion.

Only cations in site II and site III are accessible to NO molecules, entering through the supercage. The remaining sites are enclosed by the six-membered rings of the sodalite cages. Due to its small diameter, only small molecules such as H_2 will reach cations at these sites. Thus, the ability to direct cations at sites accessible to reactants is essential.

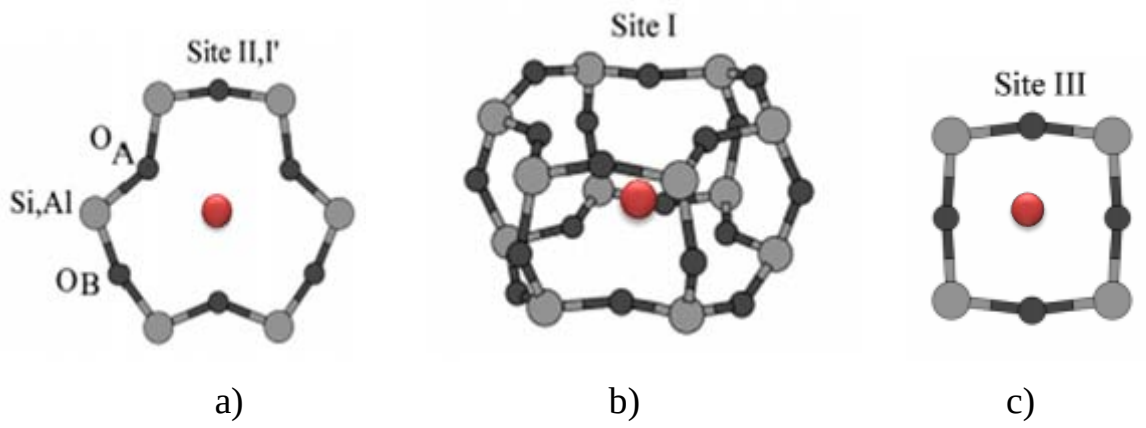

Figure 1.3 Cation (●) exchange sites in zeolite Y [5].

1.2 Ion-exchanged zeolite catalysts in the deNOx reaction [8, 9, 10, 11, 12]

The link between the catalytic properties of ion-exchanged zeolites and the work performed in this thesis lies in the NO_x problem. This is explained in the following.

1.2.1 Zeolite catalysts

So far the term "catalyst" has been mentioned several times, without a proper definition. Fogler [8] defines a catalyst as *"a substance that affects the rate of a reaction but emerges from the process unchanged. A catalyst usually changes a reaction rate by promoting a different molecular path (mechanism) for the reaction."* When the feed is gaseous, the reaction occurs at the gas-solid interface in the heterogeneous catalyst. It is necessary for the interfacial area of the catalyst to be large to obtain a significant reaction rate. A reaction is not catalyzed over the entire solid surface, but only at certain active sites. An active site is defined by Fogler [8] as *"a point on the catalyst surface that can form strong chemical bonds with an adsorbed atom or molecule"*.

The inner porous structure of zeolites supplies the area needed for a high rate of reaction. Catalytic properties of zeolites can be modified by introducing transition metal cations by ion-exchange. For a cation A^{Xa}, initially in a solution and a cation B^{Xb}, initially in a zeolite, the exchange can be written as follows [9]:

$$X_b A^{Xa} + X_a B^{Xb}* \leftrightarrows X_b A^{Xa}* + X_a B^{Xb} \quad (1\text{-}1)$$

Here, Xa and Xb are the valences of the ions. The sign * denotes a cation inside the zeolite crystal. Thermal stability of ion-exchanged zeolites is of course a prerequisite for sufficient catalytic activity and durability in practical applications. Structural collapse leads to catalyst deactivation.

1.2.2 The NO_x problem

Exhaust gases from vehicle engines are mainly carbon dioxide, carbon monoxide, hydrocarbons, nitrogen oxides (NO_x), sulfur dioxide and particulates. NO_x is a term for NO and NO_2. NO_x reacts with hydrocarbon in presence of sunlight, contributing to formation of smog and ground level ozone. Catalytic methods for removal of NO_x from the engine exhaust gas are usually classified into (i) non-selective reduction; (ii) selective reduction, and (iii) decomposition. Non-selective reduction takes place in the three-way catalytic converters in the spark ignition engines. The exhaust gas from these engines contains essentially no excess oxygen, and nitrogen oxides are “non-selectively” reduced by hydrocarbons, carbon monoxide and/or hydrogen.

For the three-way catalysts (TWC) to function it is required that the engine operates within a narrow band of air-fuel ratios, close to a stoichiometric value. Otherwise, the conversion efficiency drops, so it is necessary to maintain sufficiently accurate control of the mixture ratio. But this requirement results in higher fuel consumption than what could be achieved without a TWC.

In contrast to spark ignition engines, lean-burn engines, i.e. diesel engines, operate under highly oxidizing conditions. This improves fuel economy, and increases the demand for diesel engines throughout the world. However, NO_x treatment in oxygen-rich exhaust gas using TWC is of low efficiency. Thus, special treatment of NO_x from diesel engines is needed. This can be accomplished by using hydrocarbons or hydrogen in the exhaust stream as “selective” reducing agents for reduction of NO_x in an oxidizing atmosphere. Such a process is the so-called selective catalytic reduction of nitrogen oxides in presence of hydrocarbons reduction (SCR-HC).

In 1981 Iwamoto et. al. [13] reported that copper ion-exchanged zeolite Y was catalytically active for decomposition of NO to N_2 and O_2. Another breakthrough came in 1990 with the discovery of SCR-HC over copper ion-exchanged zeolites [10, 14]. But neither of the reported catalysts had sufficient activity or durability for practical applications [12, 15]. Yahiro and Iwamoto [15] proposed that the redox properties of copper-zeolites can be attributed to their catalytic activity in the decomposition/reduction of NO_x, where the Cu(I) species participate in the reaction. A prerequisite for deNO_x activity is stabilization of copper(I) within the structure, together with reversibility of the copper valence state [16].

Mathisen [17] has shown that zeotypes containing silver were catalytically active upon NO_x conversion. It was also shown that in one of these materials (AgSAPO) the adsorption of NO_x was too strong. On the other hand, adsorption of NO_x was shown to be too week in copper zeotypes. Both situations result in low conversion of NO_x.

1.3 The research question explained

Based on the above findings and challenges, the work in this thesis explores simultaneous copper and silver ion-exchanged zeolite H-Y. Understanding the catalytic potentials of transition metal ion-exchanged zeolites requires knowledge of coordination and electronic structure of the metal ions, i.e. active sites [5]. Two main research questions are therefore posed:

1. What are the location and structure of copper in presence and absence of silver in zeolite Y prior to and during thermal treatment in reducing and oxidizing environments?

2. Is zeolite Y containing both copper and silver an appropriate catalyst for NO_x conversion?

Research question 1 can be decomposed in the following sub-questions:

1.1 What is the resulting weight percentage ratio of silver/copper when the silver(I)/ copper(II) solution ratio is varied upon simultaneous cation-exchange in zeolite H-Y?

1.2 Will the coordination of copper cations in zeolite Y be influenced by presence of silver co-cation? I.e. will copper cations occupy different sites in zeolite Y in presence compared to absence of silver co-cations? If changed, is the coordination dependent on the copper/silver weight percentage ratio?

1.3 Do the redox properties of copper in zeolite Y change by presence of silver co-cations?

1.4 Is the crystallinity and particle size of the ion-exchanged zeolite Y itself influenced by thermal treatment in reducing and oxidizing environments?

Research question 2 can be decomposed in the following sub-questions:

2.1 Is the catalytic activity for selective reduction of NO_x in presence of hydrocarbons (SCR-HC) improved by simultaneous presence of copper and silver in zeolite Y, compared to zeolite Y containing only copper?

2.2 Is the copper and silver ion-exchanged zeolite Y sufficiently active and durable to be considered for practical applications?

1.4 Structure of this thesis

To answer the main research question 1, different characterization methods have been used. Theory of X-ray Absorption Spectroscopy (XAS) is briefly described in Chapter 2. Here, an introduction to Inductively Coupled Plasma Mass Spectrometry (ICP-MS), X-ray Diffraction (XRD) and Scanning Electron Microscopy (SEM) is also included. General theory and theory of data extraction of Extended X-ray Absorption Fine Structure (EXAFS) is covered in Chapter 3. An introduction to general experimental aspects of X-ray absorption spectroscopy is given in Chapter 4.

Part II consists of the results, discussion and conclusion. ICP-MS results are presented in Chapter 5, and XAS results in Chapter 6. Results from the final characterization methods, XRD and SEM, are given in Chapter 7.

Results from the conversion of NO_x measurements are presented in Chapter 8, giving answer to research question 2. In Chapter 9 discussion of the results is given. The thesis is completed by conclusion and recommendations for future work in Chapter 10 and Chapter 11, respectively.

References

1. Subhash Bhatia, Zeolite catalysis: principles and applications , CRC Press, 1990, Ch. 1, 2 & 6, and references therein

2. K. M. Mackay, R. A. Mackay, W. Henderson , *Introduction to modern inorganic chemistry*, 6th Ed. CRC Press, 2002, p. 527

3. British Zeolite Association, *How zeolites are built*, Avalible at: http://www.bza.org/Bursary04/images/SarwarP_img_5.jpg. Visited: 1.5.2009

4. S G. Turnes Palomino, S. Bordiga, and A. Zecchina, G. L. Marra, C. Lamberti, *J. Phys. Chem. B*, 2000, **104**, 8641-8651

5. A. Delabie, K. Pierloot, M. H. Groothaert, R.A. Schoonheydt, L.G. Vanquickenborne, *Eur. J. Inorg. Chem*., 2002, 515-530

6. The International Zeolite Association, *Framework Type FAU*. Avalible at: http://izasc.ethz.ch/fmi/xsl/IZA-SC/ftc_tm.xsl?-db=Atlas_main&-lay=tm&STC=FAU&-find. Visited 1.5.1009

7. S.Tanabe and H. Matsumoto, *Framework of Zeolite Y*, Bull. Faculty of Liberal Arts, Nagasaki Univ.(Natural Science), 1990, **30**, 55-94

8. H.S. Fogler, *Elements of Chemical Reaction Engineering*, 4th Ed. Pears Education Inc, Massachusetts, USA, 2006, Chapter 10

9. A. Dyer, *An Introduction to Zeolite Molecular Sieves*, John Wiley & Sons, U.K, 1998, Chapter 6

10. Y. Traa, B. Burge and J. Weitkamp, *Microporous and Mesoporous Materials*, 1999, **30**, 3-41 and references therein

11. M.J. Heimrich, *Trans. ASME*, 1996, **118,** 668

12. S. Bhattacharyya , R. K. Das, Catalytic Control of Automotive NO_x : A Review, *Int. J. Energy Res*.,1999, **23**, 351-369

13. M. Iwamoto, S. Yokoo, K. Sakai and S. Kagawa, J. Chem. Soc., Faraday Trans. 1, 1982, **1**(77), 1629

14. Iwamoto, H. Yahiro, Y. Yu-u, S. Shundo and N. Mizuno, Shokubai, 1990, **32**, 430

15. H. Yahiro and M. Iwamoto, Applied Catalysis A: General, 2001, **222**, 163-181

16. K. Mathisen, D. Nicholson, A.M. Beale, M. Sanchez-Sanchez, G. Sankar, W. Bras and S. Nikitenko, *J. Phys. Chem*. 2009, C, 2007, **111**, 3130-3138

17. Karina Mathisen, "*Doctoral Thesis; X-ray absorption spectroscopic studies on active metal sites in zeotypes during the selective catalytic reduction of NO_x with propene in an oxygen rich atmosphere"*, NTNU, Trondheim, June 2005

2 THEORETICAL FOUNDATIONS OF THE CHARACTERIZATION METHODS

In this chapter theories on the characterization methods used in this thesis are briefly explained.

2.1 Theory of X–ray Absorption Spectroscopy

X-ray absorption spectroscopy (XAS) has gained increasing interest during the four past decades, as it provides structural information often impossible to obtain with other conventional methods. Since the physical state of the sample is not a limitation, XAS is applicable to many classes of materials and substances. When it comes to examination of heterogeneous catalysts, this technique is widely used. Through in-situ studies the active species can be "monitored" during the catalytic reactions.

Major part of the characterization is performed in this thesis is by XAS. The reason for utilizing XAS is to investigate the environment of copper when hosted by Zeolite Y in presence and absence of silver cations. The technique can give an answer to research questions 1.2 and 1.3, as it makes determination of the neighbouring atoms, multiplicity and bond distances in the immediate coordination of copper possible. The electronic structure of copper when heated in reducing (H_2) and cooled in oxidizing environments (NO) is monitored by XAS.

2.1.1 X–ray Absorption [1,2]

A monochromatic x-ray beam of energy E and intensity I travelling through a material of thickness x, will always attenuate due to interaction with the atoms. The decay in X-ray beam intensity dI is proportional with the original intensity I and the distance x:

$$dI = -\mu I dx \qquad (2\text{-}1)$$

The proportionality constant μ is the linear absorption coefficient. Integrating Eq. (2-1) gives

$I/I_0 = \exp(-\mu X)$ (2-2)

where I and I_0 are the intensities of the incident and transmitted x-ray beam upon movement through a homogenous sample of thickness x.

Figure 2.1 illustrates the absorption coefficient plotted as a function of the incident photon energy, E. As the photon energy gradually increases (or the wavelength λ of the X-rays gradually decrease), the absorption coefficient μ shows a general decrease interrupted by a sharp rise at certain energies, called edges. At these points the photon energy, denoted E_0, is sufficient to eject an electron from a core shell of an atom, and the absorption coefficient increases.

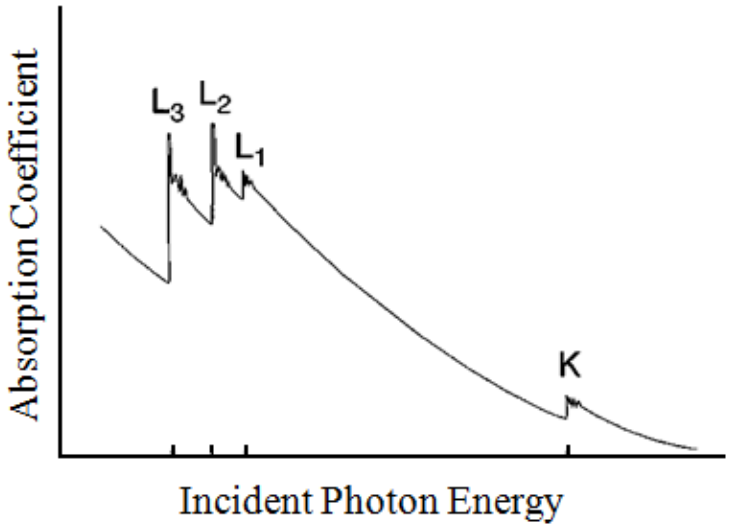

Figure 2.1 Schematic view of x-ray absorption coefficient as a function of incident photon energy. Four x-ray edges are shown: *K*, *L*1 , *L*2 , and *L*3 [2].

The nomenclature for x-ray absorption refers to the origin of the core orbital. Transitions that excite the innermost 1s electron are denoted as *K* edges. L_I, L_{II} and L_{III} edges correspond to transitions that excite the 2s electron, the $2p_{1/2}$ electron and the $2p_{3/2}$ electron, respectively. The resulting excited electron is often referred to as a photoelectron. The transition is always to unoccupied states, i.e., to states with a photoelectron above the Fermi energy, which leaves behind a core hole [2]. The edge energies (or ionization energies) are characteristic for the type

of atom absorbing the x-ray. Therefore, the edges can be regarded as signatures of the atomic species present in a material, making XAS an element specific technique.

X-ray absorption spectra are usually divided into four distinctive regions:

- Pre-edge
- Absorption edge
- X-ray absorption near edge structure (XANES)
- Extended x-ray absorption fine structure (EXAFS)

An X-ray absorption spectrum with K–edge of copper metal is shown in Figure 2.2 with these four regions indicated. In the following sections, each of them is briefly described. EXAFS is of major importance and is described in greater details in Chapter 3.

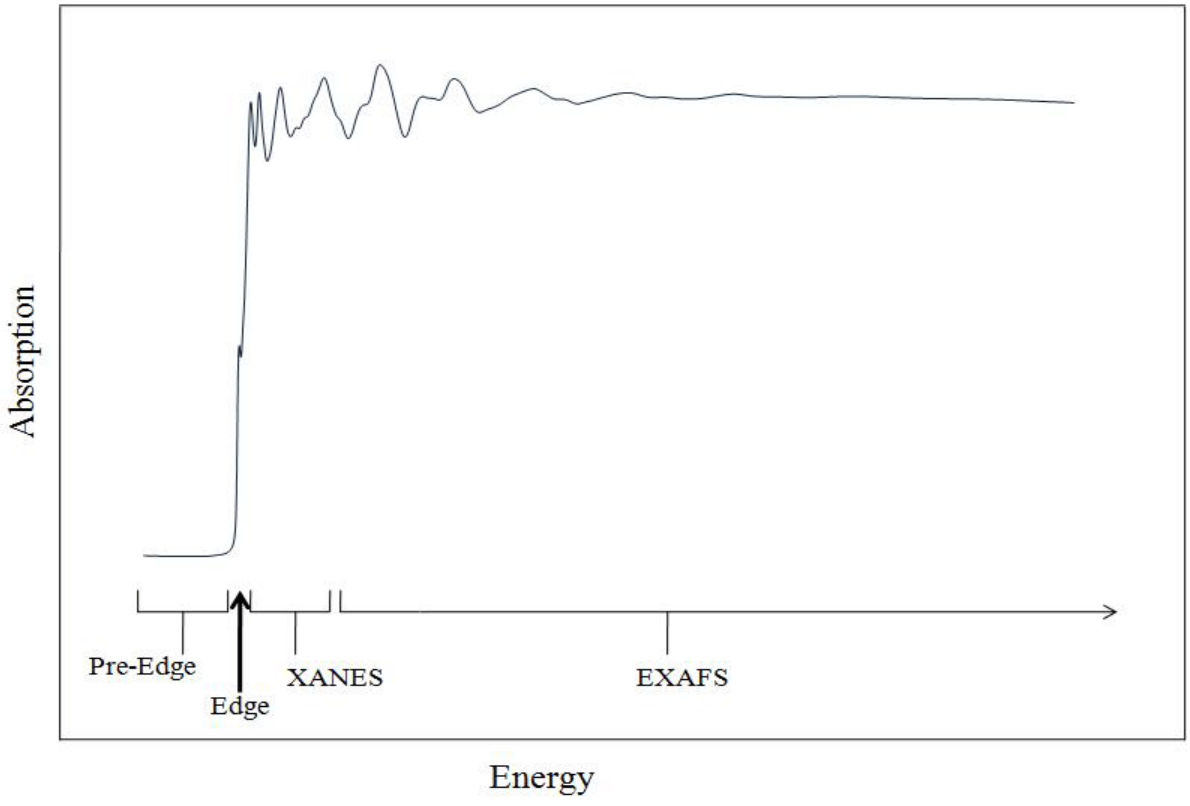

Figure 2.2 Normalized X-ray absorption spectrum (*K*–edge of Copper metal) with the four regions.

2.1.2 The Pre-Edge Region [3, 4, 5]

Compounds of the 3d transition metals may exhibit an increased absorption already below the edge. These pre-edge features can give information on the imitate coordination about the metal and its valence state. Occurrence of the pre-edge features is governed by the electric dipole selection rules, stating which transitions are allowed and which are forbidden. Transitions between orbitals of same symmetry are forbidden, while transitions between orbitals of different symmetry are allowed. Thus, s → d transitions are forbidden, whereas s → p transitions are allowed.

If the absorbing 3d transition metal has a tetrahedral environment, a distinctive pre-edge feature due to 1s → 3d will be observed below the edge. The transition is to a p-d hybridized orbital, and therefore allowed. The intensity of the pre-edge feature is dependent on the number of 3d electrons. d^0 compounds give peaks of higher intensity than d^9 compounds. With decreasing number of the 3d electrons, the hybridized p-d orbital adopts more of a p character, resulting in a higher pre-edge peak. For the same reason, the intensity of the pre-edge features depends on coordination number of the absorbing atom. The intensity for a two-coordinated 3d transition metal is much greater than for four-coordinate.

For 3d transition metals in centrosymmetric sites, the pre-edge is very weak or absent. If they occur, it is due to distortion of the symmetry imposed by the environment, or asymmetrical vibration, destroying the centre of inversion.

An illustrative example is the pre-edge seen at 8979 eV for CuO (see section 6.2.1). This feature is characteristic for many copper(II) compounds with centrosymmetric environment [4]. It arises due to the dipole forbidden 1s → 3d transition. Such pre-edges are observed due to hybridization of the 3d states with ligand p-states, as transitions from s to p states are dipole-allowed.

2.1.3 The Absorption Edge [2, 6]

In general, the wavelengths at which absorption edges occur depend on separation of the atomic energy levels, which in turn depend on atomic number. Absorption edges are therefore element specific and may be used for identification purposes. The position of the edge for an element also depends on its oxidation state. Positive metal ions have a higher energy threshold than the corresponding neutral atom, since core electrons in the former are more tightly bound to the nucleus due to effective nuclear charge.

2.1.4 XANES [7, 8]

XANES is a loosely defined spectral range, but it is usually defined as a region lying approximately 50 eV beyond the edge. It arises from a variety of physical effects, for instance multiple scattering experienced by excited electrons of low kinetic energy and many-body interactions. Electron states of low energy are of particular interest since they bond the system together and determine its electronic properties. Extracted from the XANES region is electronic and geometric structure information on the absorbing atom, such as site symmetry, bond angle and electronic configuration.

Even though it is possible to gain a great deal of structural information from XANES in addition to EXAFS, for instance information on bond angles which is contained in the multiple scattering processes, the complexity of the analysis is great.

2.1.5 EXAFS [1, 2, 9]

When an atom absorbs an X-ray photon with sufficient energy to eject a core electron, the outcome can be presented as an outgoing spherical wave with origin at the central atom. When other atoms are in the vicinity of the absorbing atom, they will backscatter the wave, giving an incoming wave. Interference between the outgoing and incoming wave arises, which is the source of the oscillatory variation or the ripples in the X-ray spectrum called EXAFS, shown in Figure 1.2. They start somewhat past an absorption edge and extend about 1000 eV further. This part of XAS provides structural information on the local three-dimensional environment, including average interatomic distances and the number and chemical identities of neighbours within 5 to 6 Å of the absorbing atom. A wider discussion on EXAFS is given in Chapter 3.

2.2 Inductively Coupled Plasma Mass Spectrometry

Inductively coupled plasma mass spectrometry (ICP-MS) is utilized for trace elemental analysis of many different materials. This technique offers low detection limits down to subpart per billion (ppb). In this thesis ICP-MS was used to answer research question 1.1, i.e. to determine amounts of copper and silver resulting in Zeolite Y as a consequence of varying ratio of the initial copper(II) and silver(I) solutions upon ion-exchange.

2.3 X-ray Powder Diffraction [6, 9]

For identification of crystalline materials, X-ray diffraction (XRD) is one of the most useful and frequently applied techniques. To obtain a diffraction pattern from crystals, it is necessary to use radiation with a wavelength in the same size order as the distances between atoms in the crystals, i.e. 10^{-10} m or 1 Ångstrøm. It follows that x-rays are suitable since they have the appropriate wavelength. This technique can give an answer to research question V, regarding the stability of ion-exchanged zeolite Y crystallinity when thermally treated in reducing and oxidizing environments. Comparing diffraction patterns of the as-prepared sample with diffraction patterns of the sample after treatment can show possible changes in the crystalline structure of zeolite Y, which gives an answer to research question 1.4.

A conventional X-ray source consists of a metal target, often copper. When a beam of accelerated electrons hit the target, some of the copper 1s electrons will be ionized, leaving a core hole in the *K* shell. This vacancy will rapidly be occupied by an electron from an outer orbital (2p or 3p) under emission of an X-ray quantum. The Cu Kα line arises from the 2p→1s transition, while the Cu Kβ line is assigned to 3p→1s transition. The wavelengths are 1.5418 Å and 1.3922 Å, respectively. Kα radiation is used in diffraction experiments because it occurs much more frequently and it is also more intense than Kβ radiation.

A powdered zeolite sample consists of many, randomly orientated crystallites. Incident X-ray beams will be reflected off the different planes within a crystal. For the reflected beams, constructive interference will occur when Bragg's law is satisfied:

$$n\lambda = 2d \sin \theta \qquad (2\text{-}3)$$

where d is the is the distance between adjacent planes within a crystal, θ is the beam angle relative to the sample surface, λ is the X-ray wavelength and n is a whole number of wavelengths. Each reflection has certain intensity at a particular Bragg angle, giving rise to characteristic patterns for different crystalline compounds.

2.4 Scanning Electron Microscopy (SEM)

SEM is used to produce magnified images of bulk materials with three-dimensional print. It is convenient for surface studies and measurement of particle size in powdered samples. SEM is used to give an answer to the research question 1.4 regarding changes in particle size and morphology of zeolite Y when undergoing thermal treatment in reducing and oxidizing environments.

References

1. B.K. Teo, D.C. Joy, *EXAFS Spectroscopy Techniques and Applications*, Plenum Press, New York and London, 1981, Ch. 1 and X

2. J. J. Rehr, R.C. Albers, *Theoretical approaches to x-ray absorption fine structure*, Reviews of Modern Physics, 2000, 72 (3), 621-654

3. T. Yamamoto, *X-ray Spectrom*., 2008, **37**, 572-584

4. K. Mathisen, D. Nicholson, A.N. Fitch and M. Stockenhüber, J. Mater. Chem., 2005, **15**, 204–217

5. Karina Mathisen, "*Doctoral Thesis; X-ray absorption spectroscopic studies on active metal sites in zeotypes during the selective catalytic reduction of NO_x with propene in an oxygen rich atmosphere"*, NTNU, Trondheim, June 2005, Chapter 2

6. A. R West, *Solid State Chemistry and its Applications*, John Wiley & Sons, U.K. (1984), Ch. 3 and 5

7. D.C. Koningsberger, R Prins, *X-Ray Absorption – Principles, Applications, Techniques of EXAFS, SEXAFS AND XANES*, John Wiley & Sons, 1988, Ch. 2

8. P. Behrens, *Trends in Anal. Chem*.,1992, **11**(7), 237-244

9. E.A.V. Ebsworth, D.W.H. Rankin and S. Cradock, *Structural Methods in Inorganic Chemistry*, 2nd ed., Blackwell Scientific Publications, Oxford (U.K) 1991, Ch. 8

3 EXTENDED X-RAY ABSORPTION FINE STRUCTURE (EXAFS); GENERAL THEORY AND THEORY OF DATA EXTRACTION

When measuring the X-ray absorption coefficient μ as a function of photon energy, the energy is first tuned to the binding energy of some atom type core level within the sample. The absorption edge occurs due to ejection of a core electron. Beyond the edge the absorption coefficient as a function of photon energy decreases monotonically for isolated atoms. On the other hand, for atoms in molecules a variation in the absorption coefficient is displayed when fine structure is observed. This oscillatory variation is called EXAFS. Such fine structure may extend up to 1000 eV above the absorption edge, and contains information on neighbouring atoms, multiplicity and bond distances in the immediate coordination of copper, needed to answer research question 1.2.

There are several different mathematical models correlating the resulting EXAFS function to characteristic quantities for the environment of the absorbing atom. Here, brief introduction to the theoretical expression of EXAFS developed by Sayers, Stern and Lytle [1] is given. The raw experimental data must be reduced to properly normalized EXAFS data for analysis. This is a multistep procedure. The programs *ATHENA* and *EXCURV98* were used for this purpose, and are described in this chapter.

3.1 Theory [2, 3, 4]

When a target atom absorbs an X-ray photon with energy greater than the absorption threshold E_0 (Figure 3.1 i), a photoelectron is ejected and as an outgoing wave (Figure 3.1 ii). The kinetic energy E of the photoelectron is the difference between photon energy ($E_{h\upsilon}$) and E_0:

$$E = E_{h\upsilon} - E_0 \qquad (3\text{-}1)$$

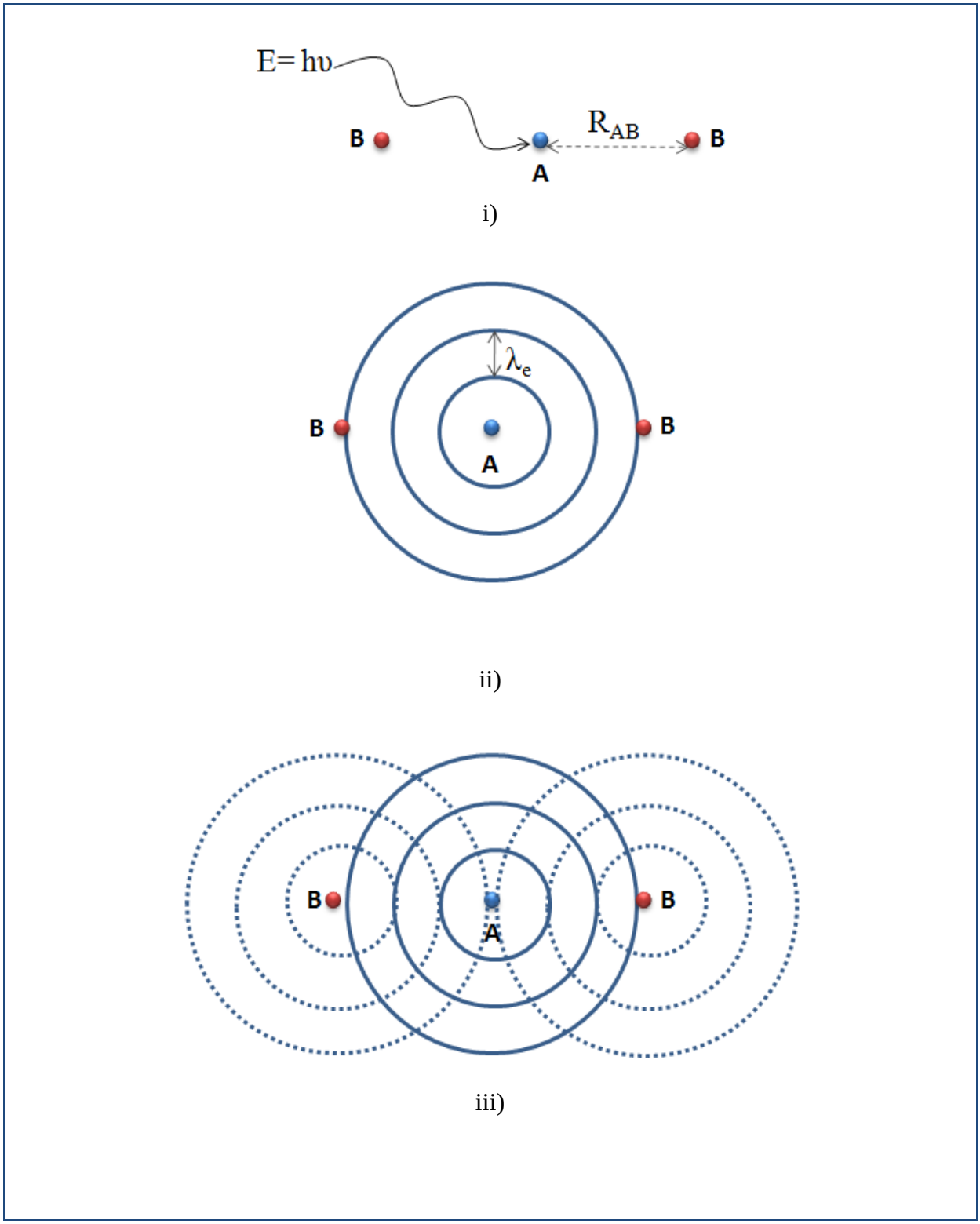

Figure 3.1 The scattering process occurring when the X-ray photon transfers its energy to excite a photoelectron[4]

If no neighbouring atoms are present, the outgoing spherical wave will spread outwards with wavelength $\lambda = 2\pi/ k$ where

$$k = \sqrt{\frac{8\pi^2 m}{h^2}(E_{h\nu} - E_0)} \qquad (3\text{-}2)$$

m - the rest mass of the electron,

h - Planck's constant

$E_{h\upsilon}$ - the energy of the incident photon and

E_0 – the threshold energy needed to eject a core electron from an atom at the given absorption edge

When neighbouring atoms are present, the outgoing wave is backscattered. The backscattered wave interferes with the outgoing wave (Figure 3.1 iii), giving oscillations in the X-ray absorption spectrum.

Only the oscillatory part of the X-ray absorption spectrum is considered in the theory of EXAFS. The normalized fraction of the spectrum is termed $\chi(E)$, where the oscillations are separated from the background absorption:

$$\chi(E) = \frac{\mu(E) - \mu_0(E)}{\mu_0(E)} \qquad (3\text{-}3)$$

$\chi(E)$ – modulation of the absorption rate in EXAFS

$\mu(E)$ – the total measured absorption at a given X-ray wavelength

$\mu_0(E)$ – the smooth background absorption

$\mu_0(E)$ cannot be measured experimentally, except for monatomic gases. Physical isolation of the sample atoms in a condensed state is not possible, therefore $\mu_0(E)$ is approximated by a smooth curve determined numerically.

3.2 The EXAFS equation [2, 5, 6, 7, 8]

In order to relate $\chi(E)$ to structural parameters, it is converted from the energy scale (eV) to the photoelectron wave vector or k scale ($Å^{-1}$) via Equation 3-3. This requires for E_0 to be known, but it can often be problematic to exactly point out this value in the absorption spectrum. To choose E_0 arbitrary near the edge is adequate; a small error is not fatal and can also be corrected during data analysis. The EXAFS equation, being a theoretical expression described in terms of structural parameters, is consequently achieved by the transformation of $\chi(E)$ in E space to $\chi(k)$ in k space where

$$\chi(k) = \sum_j N_j S_i(k) F_j(k) e^{-2\sigma_j^2 k^2} e^{\frac{-2r_j}{\lambda_j(k)}} \frac{\sin(2kr_j + \phi_{ij}(k))}{kr_j^2} \qquad (3\text{-}4)$$

In Equation 3-4 the EXAFS is defined in terms of sets of identical scattering atoms referred to as shells. A shell contains N_j identical scattering atoms. The mean distance between the central atom and neighbouring atoms in jth shell is denoted as r_j. Each of the neighbouring atoms in the jth shell has a backscattering amplitude, $F_j(k)$. The backscattering amplitude is not depended on the absorber; it is a function of the scatterer atom type only (atomic number Z). The amplitude of $F_j(k)$ at high k shows a general increase with increasing atomic number of the backscatter. The position of the amplitude maximum moves to higher k under the same circumstance.

The $\sin(2kr_j + \phi_{ij}(k))$ fraction of Equation 3-4 is the total phase function of the backscattered photoelectron wave at the central atom. The photoelectron travels a distance $2r_j$; out to the backscatter atom and back to the absorber atom. $2r_j/\lambda_e$ is the number of wavelengths that covers this distance. Here, λ_e is the wavelength of the photoelectron, which corresponds to its kinetic energy, E. This leads to a phase change given by $(2\pi \cdot 2r_j/\lambda_e)$. Since $k = 2\pi/\lambda_e$, the phase change is expressed as $2kr_j$ in Equation 3-4. This is the first contributing part to the total phase shift.

The photoelectron moves through varying potentials (i.e. the potential of the excited absorber and the potential of the neutral neighbour) in the backscattering process. These potentials give additional phase shifts, accounted for in the second part of the total phase as $\phi_{ij}(k)$.

Because of the thermal vibrations or structural disorder, the neighbours in a given coordinating shell will not all be at the exactly same distance. The contributions from these atoms to the interference will not be exactly in phase. This dephasing is accounted for by the term $e^{-2\sigma_j^2 k^2}$ in Equation 3-4. Here, σ_j is the Debye-Waller factor, defined as root mean square deviation from the average distance r_j.

Only elastically scattered electrons can take part in the interference process. This is accounted for by $e^{-2r_j/\lambda_j(k)}$, a damping factor approximating the inelastic losses in the scattering process due to excitation of the neighboring environment. Here, $\lambda_j(k)$ is the elastic mean free path of the photoelectron. Finally, the losses in $F_j(k)$ due to due to multiple excitations at the absorber are accounted for by the amplitude reduction factor $S_i(k)$. I.e. it is a measure of the proportion of the absorption events resulting in just a single photoelectron.

Equation 3-4 can only be applied to photoexcitations of an s state electron, i.e. K and L_I edges. For excitations from a p or any other states, a different kind of expression for $\chi(k)$ must be used. Basis for the EXAFS equation is the *plane-wave* approximation, assuming that the atomic radii are much smaller than the interatomic distance. The outgoing or the incoming *spherical* electron waves are approximated by *plane waves*, neglecting the curvature of the wave at the scattering atom. This simplifies the resulting $\chi(k)$ expression. The plane-wave approximation is best suited when high energy data is utilized ($E \geq 60$ eV or $k \geq 4$ Å^{-1}), but brakes down at lower energies. The calculated phase of $\chi(k)$ may contain errors when low photoelectron energy is used, which in turn can lead to incorrect determination of the interatomic distances (r). In such cases, it may be useful to use so-called curved-wave approach.

The exact curved-wave theory can be found in Lee and Pendry [9]. Mathematically it is very complicated and difficult to apply in data analysis. Gurman, Binsted and Ross [10] have

developed a simplified version, which the program EXCURV98 used in this thesis, is based on.

3.3 Data processing

EXAFS is quite simple when it comes to data collection. Extraction of information on the other hand can serve a great deal of difficulties since it involves many steps needed to reduce the raw experimental data to properly normalized EXAFS data for analysis. Therefore, a consistent approach when it comes to data processing is required. In the following sections a basic description is given on operations necessary to access the parameters of interest in a material.

3.3.1 Primary data reduction [2, 5, 6]

The first step in data reduction removes of the underlying absorption background from the overall X-ray absorption spectrum. A polynomial curve is fitted to pre-edge region and extrapolated to the end of the spectrum. Subsequently the curve is subtracted from the spectrum.

To extract $\chi(E)$, $\mu_0(E)$ must be removed from $\mu(E)$. $\mu_0(E)$ cannot be measured experimentally, except for monatomic gases. Physical isolation of the sample atoms in a condensed state is not possible, therefore $\mu_0(E)$ is approximated numerically for the post edge background. Several methods can be applied to this operation. The most recommended is subtraction of a cubic least-squares-spline approximant to the data [5], although any kind of background removal has the potential of data distortion.

In the second step, the photon energy E is converted to the photoelectron wave vector k via Equation 3-2. For E in eV and k in Å-1,

$$k = \sqrt{0.2625\ (E_{h\upsilon} - E_0\ )} \qquad (3\text{-}5)$$

E_0 is usually noticed in the first derivative of the experimental absorption curve (i.e. the edge position). Exact determination of E_0 is not necessary, because E_0 is allowed to vary in the final analysis.

3.3.2 Presentation of the main features of ATHENA [11, 12, 13]

Athena is first and foremost a program for data processing and preparation for analysis. It includes a large number of operations, but here the focus will be put on those used during this thesis. In a broad sense, the processing can be divided into three main parts [1]:

- Import raw data and convert it to $\mu(E)$
- Normalize the data
- Determine the background function and subtract it from the data to make χ(k)

Other details, such as merging data, energy calibration, deglitching, truncating and fitting linear combinations of standards to XANES is also discussed.

The raw data consist of columns of energy, I_0, I_1, etc. Athena contains a menu for column selection upon data importing which needs to be set correctly in order to convert to $\mu(E)$.
Occasionally, the measured data need to be calibrated. This is done by selecting a point in the data as the edge energy and applying an energy shift, such that the selected point is at a specific value. The energy-scale calibration is done most satisfactory by measuring the metal foil in parallel to the sample. Since the edge position of metals is known, finding the energy shift and applying it to the unknown sample is quite simple.

Normalizing implies regulation of data with respect to sample thickness, absorber concentration and detector settings, so that data can be compared regardless of the details of the experiment. Athena performs edge-step normalization by regressing a line to the data in the pre-edge range and a polynomial to the data beyond the edge. The pre- and post-edge lines are extrapolated to the edge energy E_0. The difference between these two lines is the normalization constant $\mu_0(E_0)$ in the definition of $\chi(E) = [(\mu(E) - \mu(E_0)] / \mu_0(E_0)$.

Background is a part of $\mu(E)$ data that contains low frequency Fourier components, while the data consist of the remaining, higher frequency Fourier components. Background removal is a default behaviour of ATHENA aiming to reduce the low frequency components.
To obtain $\chi(k)$, the x-coordinates of $\chi(E)$ are converted by Equation 3-2.

E_0 is usually automatically determined by Athena as the position of the first large peak in the derivative of the $\mu_0(E)$ spectrum. It is also possible to set E_0 interactively, for instance to the position of half the edge step height.

Sometimes the data may contain "false" points, the so-called glitches, which are obviously different from the surrounding points. Large glitches may impact data processing, and should be removed. This is done by simply removing these point(s) in ATHENA. No interpolation from the surrounding points is performed, the points are only deleted.
If the data is of poor quality with much noise at the end of the scan, the easiest solution might be to truncate. ATHENA allows chopping data after a selected point in order the remove the noisy part.

After performing the above described steps, the data are ready to be exported such that input can be made to other programs. When aiming for analysis in EXCURV98, the data from ATHENA are exported as column data files $\chi(E)$ and changed from absolute to relative energy.

Linear combination fitting

Qualitative XANES analysis can be carried out by linear combination fitting, a tool available in ATHENA. This method is based on least-square minimization of the quadratic difference between the sample spectrum and a linear combination of reference spectra [3]. The purpose of using the linear combination in this thesis is to determine quantities of different copper species in the unknown samples during in-situ measurements. In such a procedure, each intermediate spectrum is fitted as a linear combination of a selection of standards, including reference compounds. The fitting is done using the normalized $\mu(E)$ spectra. There is an option in ATHENA of forcing the fitted weights to sum 1, which was always chosen for the linear combination fitting of data included in this thesis. The R-factor reported after fitting is

$$R = \frac{\sum((\text{data} - \text{fit})^2)}{\sum((\text{data})^2)} \qquad (3\text{-}6)$$

where the sums are over the data points in the fitting region. A large R is an indication of poor fitting.

This fitting method for XANES analysis requires some knowledge of the number and the chemical composition of the chemical species hosting the element under analysis. Thus, the reference compounds used in linear combination fitting should be chosen with care.

3.3.3 Presentation of the main features of EXCURV98 [5, 14, 15, 16, 17, 18, 19]

Analysis of data by EXCURV98 [14] yields values of inter-atomic distances, coordination number and Debye-Waller factors in the sample under study. The original EXCURV program was written in 1982. It was based on the rapid, exact curved-wave theory, later published by Gurman, Binsted and Ross (1984) [10], which is a simplification of the EXAFS theory by Lee and Pendry (1975) [9]. The simplified, exact curved-wave theory is also basis for the 1998 version.

Reading in spectrum

The input for analysis in EXCURV98 is the background-subtracted and normalized absorption spectrum given in terms of eV above the edge position. The energy is relative to the edge, i.e. E_0 equals 0. Next, the central atom type is defined together with the initial state (e.g. Cu K-edge). Further on, all the scattering atoms need to be defined. A scatterer of the same element type as the absorber is also required, since EXCURV98 calculates excited and scattering atom phaseshifts slightly differently.

Fourier transform of $k\chi(k)$ results in a series of peaks, each corresponding to a shell of atoms contributing to the EXAFS. EXCURV98 displays both the experimental and calculated spectra of either EXAFS or its Fourier transform. However, in the Fourier transform, the peaks will be shifted from the true interatomic distance by the impact of total phase shift. To move all peaks close to their true interatomic distances, the phaseshifts for the central atom and the defined backscatters must be calculated by EXCURV98.

Refinement

Data analysis by EXCURV98 is a least-squares fitting process aiming to minimize the difference between the experimental and calculated values by varying the parameters defining the immediate environment of the absorbing atom. These varying parameters are typically the correlated pairs (E_0, r_j) and (Nj, σ_j^2), Others, such as AFAC are obtained from model compounds or theoretical calculations and held fixed (definition of these parameters is given below). Due to correlation, simultaneous refinement of the parameters is often necessary. The refinement is repeated until a good fit is achieved. This means a satisfactory reliability factor and small uncertainties on the fitted parameters.

There are a large number of other parameters governing the theory calculation and refinement. The definition of the parameters utilized upon analysis of EXAFS in this work is as follows:

Ns – The number of shells (sets of identical scattering atoms) used for calculations.

Nn – The number of atoms in shell n

Tn – Element type in shell n

Rn – The radial distance between the absorber and shell n

An – Debye–Waller factor for shell n, defined as $2\sigma^2$, where σ^2 is the root mean square deviation from the average distance *Rn*

EF – correction of the E_0 value. EF oscillates about zero (Since E_0 is set to 0) and can be negative or positive and normally $-15 < EF < 15$

AFAC – amplitude reduction factor; approximates losses in the amplitude due to multiple electron excitations at the absorbing atom. AFAC should be approximately 1

EMIN – Minimum energy above the edge for EXAFS theory calculations

EMAX – Maximum energy above the edge for EXAFS theory calculations

KMIN – Minimum wave vector for EXAFS theory

KMAX – Maximum wave vector for EXAFS theory. Changing EMIN/MAX automatically changes KMIN/MAX and vice versa

The statistical term R-factor gives an indication of the quality of the fit to the experimental spectrum in k-space, and is defined as

$$R_{exafs} = \sum_i^N 1/\sigma_i \, (|\chi_i^{exp}(k) - \chi_i^{th}(k)|) \times 100\% \qquad (3\text{-}7)$$

Values of around 20% are considered as reasonable fits, while values of 10 % or less are difficult to obtain.

Weighting

The attenuation of EXAFS amplitude at high *k* values can be compensated for by multiplying χ(k) by some power of k to give $k^n\chi(k)$. The region at high *k* values gains exponentially higher weighting. This operation prevents the larger amplitude oscillations to dominate the smaller ones when interatomic distances are to be determined. For data in the range of k = 4 – 15 Å^{-1}, it is recommended by Teo and Lee [16] to use the weighting schemes of $k^3\chi(k)$ for backscatters with atomic number $Z \leq 36$, $k^2\chi(k)$ for backscatters with atomic number $36 \leq Z \leq 57$ and $k\chi(k)$ for backscatters with atomic number $57 \leq Z \leq 86$. EXCURV98 allows any of these options to be selected.

Inappropriate weighing might produce imprecise EXSAFS spectra. The heavier the backscatter the higher number of peaks will be seen in *k* space, and hence in the Fourier transform. High power of weighting (i.e. $k^3\chi(k)$) can lead to mistake some of these peaks as a separate distances. Peak heights and positions in the Fourier transforms may be influenced by weighting. When comparing unknown samples with models same weighting scheme should be used.

The effect of weighting in EXCURV98 is clearly demonstrated in Figure 3.2. In the k^3–weighted EXAFS spectrum, the amplitude is enhanced in great magnitude. A drawback is that the noisy part of the data, seen at about k = 14 Å^{-1}, is also enhanced. Here, the noise is not severely distorting the rest of the data. However, in cases of poor data, the weighting scheme of $k^3\chi(k)$ might result in highly enhanced noise.

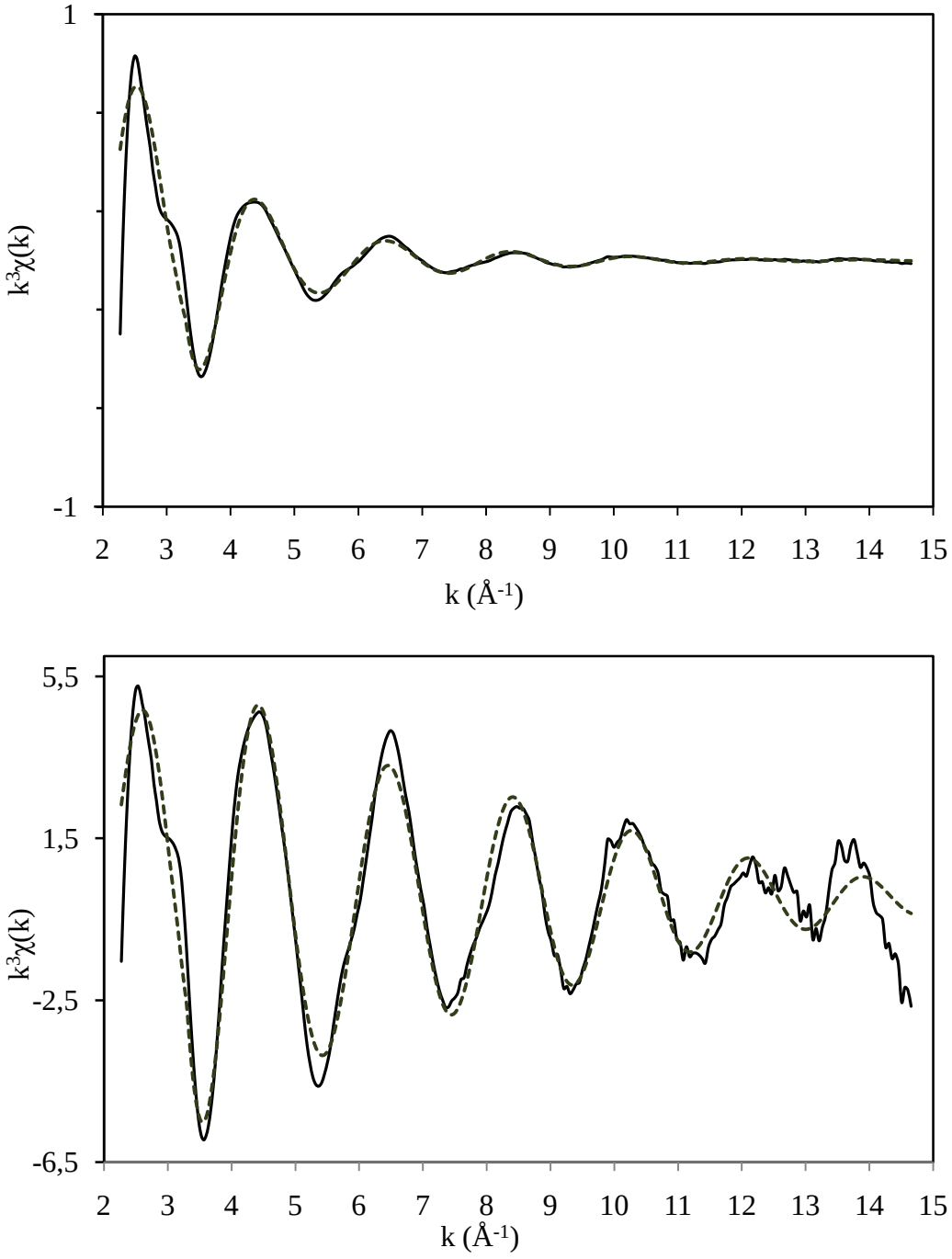

Figure 3.2 k–weighted (upper) and k^3–weighted (lower) EXAFS spectra for copper(II) –Tutton salt.

The amplitude reduction factor – AFAC

Multiple excitations at the absorbing atom will reduce the amplitude of the XAS signal, since these processes contribute to the absorption but not to the interference. In the EXAFS equation (3-4), this is accounted for in the $S_i(k)$ term. But this term is difficult to determine. In EXCURV98, $S_i(k)$ is considered independent through the amplitude reduction factor AFAC. In order to find AFAC, analysis by EXCURV98 starts off with a model compound of known structure. The absorbing atom in the model compounds is of the same valence state as in the unknown, and ideally resembles the structure of the unknown samples as well. The multiplicities are held fixed, while E_0, r_j and σ_j^2 are refined until satisfactory fit is achieved and the interatomic distances obtained are in agreement with results from for instance XRD. Thereafter, the refinement is alternated between AFAC and parameters E_0, r_j and σ_j^2, until the values stabilize. AFAC should be close to 1. The obtained value from the models is transferred to the unknown.

To get the most out of the analysis a suitable model compound should be found for comparison. But finding a resembling reference in a sense implies that one must know the answer to find the answer. Sometimes, finding a suitable model compound is not possible. To use a model that is unsuitable when determining AFAC may lead to introduction of systematic errors in the analyses of the unknown samples.

References

1. D. E. Sayers, E. A. Stern and F. W. Lytle, *Phys. Rev. Lett*., 1971, 27, 1204 – 1207

2. M. J. Fay, A Proctor, D. P. Hothnann and D. M. Hercules, *Analytical Chemistry*, 1988 **60** (21), 1225-1243

3. J. J. Rehr, R.C. Albers, *Theoretical approaches to x-ray absorption fine structure*, Reviews of Modern Physics, 2000, **72** (3), 621-654

4. Karina Mathisen, "*Doctoral Thesis; X-ray absorption spectroscopic studies on active metal sites in zeotypes during the selective catalytic reduction of NO_x with propene in an oxygen rich atmosphere*", NTNU, Trondheim, June 2005, Chapter 2

5. D.C. Koningsberger, R Prins, *X-Ray Absorption – Principles, Applications, Techniques of EXAFS, SEXAFS AND XANES*, John Wiley & Sons, 1988, Ch. 1 and 6

6. B.K. Teo, D.C. Joy, *EXAFS Spectroscopy Techniques and Applications*, Plenum Press, New York and London, 1981, Chapter 4 and 6

7. P. A. Lee, P. H. Citrin, P. Eisenberger and B.M. Kincaid, *Rev. Mod. Phys*., 1981, **53**, (4) Part I

8. S.J. Gurman, J. *Synchrotron Rad*., 1995, **2**, 56-63

9. P. A. Lee and J. B. Pendry, *Phys. Rev. B*, 1975, **11**, 2795 - 2811

10. S. J. Gurman, N. Binsted and I. Ross, *J. Phys. C: Solid State Phys*., 1984, **17**, 143-151

11. B. Ravel and M. Newville, *J. Synchrotron Rad*., 2005, **12**, 537-541

12. B. Ravel, *ATHENA User's Guide*, Document version 1.3 for Athena version 0.8.54, August 31, 2007

13. M. Fernandez-Garcia, *Catalyst Reviews*, 2002, **44** (1), 59-121

14. Binsted N. (1998) EXCURV98: CCLRC Daresbury Laboratory computer program

15. N. Binsted, *EXCURV98 The Manual*. Available at: http://srs.dl.ac.uk/xrs/Computing/Programs/excurv97/e61.htm. Visited: 14.5.2009

16. B.K. Teo and P. A. Lee, *J. Am. Chem. Soc.*, 1979, **101** (11), 2815-2832

17. Richard W JoyneriS, Kenneth J Martin and Peter Meehan, *J. Phys. C: Solid State Phys.*,1987, **20**, 4005-4012

18. M. Roy and S. J. Gurman, *J. Synchrotron Rad*., 2001, **8**, 1095-1102

19. S.J. Gurman, J. *Synchrotron Rad*., 1995, **2**, 56-63

4 AN INTRODUCTION TO GENERAL EXPERIMENTAL ASPECTS OF X-RAY ABSORPTION SPECTROSCOPY

4.1 X–rays [1, 2]

X-rays are electromagnetic radiations having wavelengths roughly in within the range from 0.01Å to 100Å. This high-energy part of the electromagnetic spectrum is of great usefulness when it comes to structural studies and characterization of chemical compounds. Diffraction and absorption are two of several main techniques for X-rays utilization. This thesis is by far concerned with absorption.

Absorption techniques imply measurement absorbed X-rays when passing through a sample at energies in the region of absorption edge. It is a powerful tool for local structure probing, but accessibility for most people is limited since a synchrotron radiation source is needed.

4.1.1 Synchrotron Radiation [3, 4, 5]

Electromagnetic radiation emitted when charged particles travel in curved paths is referred to as synchrotron radiation. It offers unique properties not attainable from conventional laboratory sources, and it is required in an XAS experiment for several important reasons3:

1. In order to obtain high signal-to-noise data in a reasonable time frame, high photon flux is needed. Compared to conventional laboratory x-ray sources, synchrotron sources provide x-rays of five or more orders of magnitude grater flux.
2. Its extreme intensity over a broad range of wavelengths (from 10^{6} to 10^{-2} Å) is very beneficial since a typical x-ray absorption spectrum covers about 1000 eV. An appropriate energy range for a specific experiment is chosen with a tunable monochromator.
3. The storage ring provides high stability in flux, energy and beam position, which are all required to achieve satisfactory data.

In addition, synchrotron radiation is highly polarized with high beam brightness (light density) and coherence, making it superior to conventional radiation sources. It is also time structured (flashes; nanoseconds pulses separated by micro- or milliseconds) meaning that time resolved experiments can be carried out.

4.1.2 A brief description of a synchrotron facility and an experimental station [4, 6, 7, 8, 9, 10, 11]

A synchrotron radiation facility consists principally of an electron gun, a linear accelerator (linac), a booster synchrotron and a storage ring. These are built up of many advanced technical components, which are described elsewhere (se under). Here, only a short description of the radiation generation is given, with the ESFR synchrotron facility illustrated in Figure 4.1.

The electron gun consists of a cathode which is heated up to high temperatures to liberate electrons from the surfaces. The linac accelerates the particles at the rate of about 15 MeV/m. When the electron beam enters the booster synchrotron (with constant orbit radius), the magnetic field is increased with time as the energy of the electrons increases. Here the beam is recycled several times through the same acceleration section, allowing final energies of many GeV. Reaching the storage ring, the electron current will circulate at essentially the speed of light on a closed orbit for periods of several hours. The stored beam circulates in a vacuum chamber equipped with bend magnets, which guide the electron beam around. The produced x-ray photons can leave the ring through tangential ports called beam lines, allowing radiation to reach experimental stations located outside the ring.

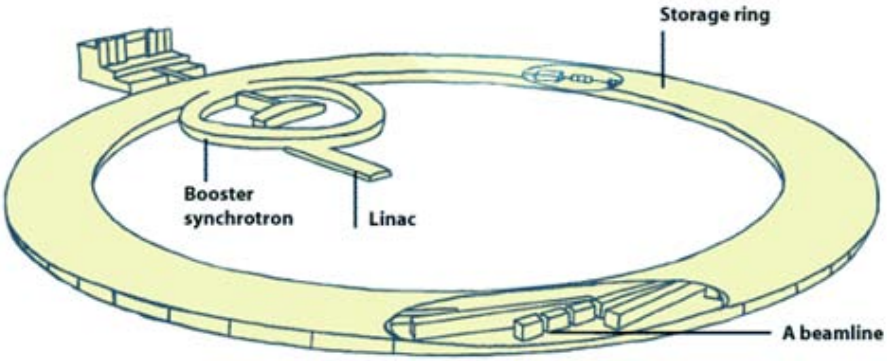

Figure 4.1 A synchrotron facility [6].

Experimental station

X-ray absorption can be measured in several modes; transmission, fluorescence, Auger or partial electron yield, depending on the degree of dilution of the sample. The copper and silver concentrations in all the samples in present work were adequate for the transmission mode, which measures the transmitted X-ray intensity directly. In contrast to e.g. fluorescence mode, significantly greater signal compared to the absorption background is achieved with the transmission mode. Figure 4.2 depicts schematically an experimental setup for XAS in this mode.

The experimental components include x-ray optics (such as monochromators), sample stage and detectors (ion chambers) for data recording. These are placed in radiation shielding interlocks called *hutches* to protect the users against radiation exposure. Settings and data acquisition for a specific experiment are controlled by computers stationed outside the hutch.

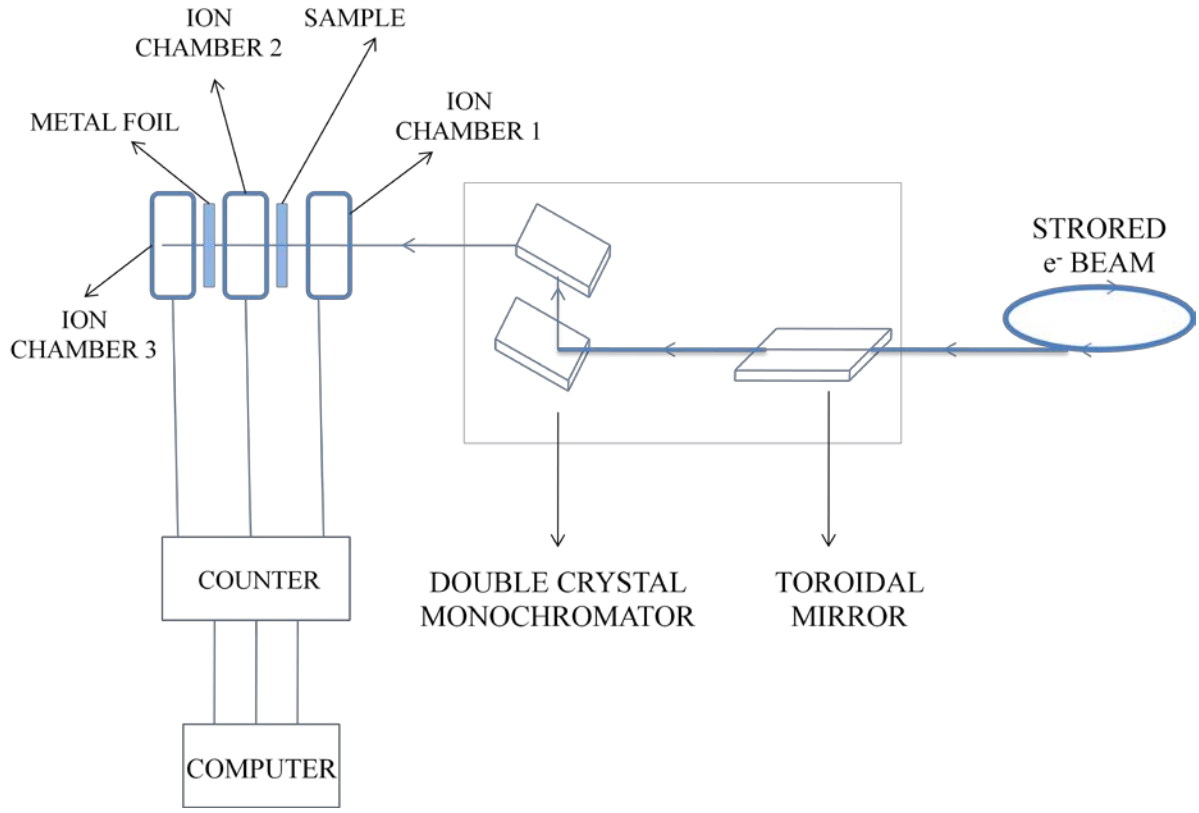

Figure 4.2 Schematic view of the experimental components for data collection in transmission mode.

The white beam from the storage ring is focused by a toroidal mirror onto the parallel double-crystal monochromator, which only diffracts X-ray photons of a certain wavelength. Which wavelengths are diffracted is governed by Braggs diffraction condition:

$$\lambda = 2d_{hkl} \sin(\theta) \qquad (4\text{-}1)$$

Hence, the desired X-ray photon wavelengths are diffracted when the input beam makes a certain angle θ with the Bragg plans of the first crystal with spacing d_{hkl}. The role of the second crystal is simply to direct the monochromatic beam parallel to the incident beam. The water-cooled double-crystal monochromator utilized at the Swiss-Norwegian beamline consists of flat Si(111) pair and Si(311) pair crystals. This monochromator is followed by two flat mirrors with Cr and Au surfaces for harmonic rejection.

The goal of an XAS experiment is to measure the X-ray absorption of a sample as a function of energy. Ion chambers are widely used for intensity measurements in the X-ray regime. The first ion-chamber (Figure 4.2) measures beam intensity before it passes through the sample. Only a small fraction of the beam intensity is allowed to be reduced before it continues further on to the sample. The second ion chamber measures the transmitted beam. The third ion chamber detects the transmitted beam through metal foil. Filled with a gas or a mixture of gasses, contained by two X-ray transparent windows, an ion chamber functions by measuring photoion current.

The sample holder is mounted on a movable sample stage, so it can be adjusted with respect to the incident beam. A successful data collection requires correct sample preparation. It is important for the sample to be as homogeneous as possible, meaning for the sample to have been grounded thoroughly before placed in sample holder. The sample thickness should be uniform. Pinholes in the sample may lead to erroneous results, and it is therefore crucial to avoid these when pressing the powdered sample into the holder. The sample holder itself should be made of other materials than the ones in the samples, so that signal-interference is avoided. This is avoided by well adjusted sample holder and a large enough sample area.

References

1. A. R West, *Solid State Chemistry and its Applications*, John Wiley & Sons, U.K. (1984), Chapter 3

2. B.K. Teo and D.C. Joy, *EXAFS Spectroscopy, Techniques and Applications*, Plenum Press, New York and London (1981), p. 37

3. R.E. Van Grieken, A.A. Markowicz, *Handbook of X-ray Spectrometry*, 2nd ed. Marcel Dekker, Inc, New York, (2002) Chapter 8

4. H. Winick, *Synchrotron Radiation Sources*, World Scientific Publishing Co.Pte. Ltd., Singapore (1994) Chapter 1

5. Brown, Gordon E. Jr.; Waychunas G. A. *X-ray Absorption Spectroscopy: Introduction to Experimental Procedures*. Stanford Synchrotron Radiation Laboratory XAS Procedures, 3.11.99

6. The European Synchrotron Radiation Facility ESRF Virtual Tour. Available on: http://www.esrf.eu/AboutUs/GuidedTour Visited: 10.5.2009

7. G. Bunker, *Introduction to Synchrotron Radiation and XAS Data collection*, Illinois Institute of Technology. Available on: http://cars9.uchicago.edu/xafs/NSLS_2002/ Visited: 26.4.2009

8. The European Synchrotron Radiation Facility, Station Bending magnet (BM1B), Available on: http://www.esrf.eu/UsersAndScience/Experiments/CRG/BM01/bm01b Visited: 1.5.2009

9. U. Bonse, G. Materlik, W. Schröder, *J. Appl. Cryst.*, 1976, **9**, 223

10. P. A. Lee, P. H. Citrin, P. Eisenberger and B.M. Kincaid, *Rev. Mod. Phys*., 1981, **53** (4), Part I

PART II

RESULTS, DISCUSSION AND CONCLUSION

5 ICP-MS RESULTS

Experimental details about sample preparation and treatment of the samples prior to the ICP-MS analysis are given in section 5.1. The results from ICP-MS are presented in section 5.2.

5.1 Experimental section

5.1.1 Preparation of the samples

Zeolite H-Y, with Si:Al ratio of 30 (supplied by Zeolyst International) was used for ion-exchanging. Solutions of 0,134 M $Cu(NO_3)_2$ (supplied by Merck KGaA) and 0,134 M $Ag(NO_3)$ (supplied by VWR/BDH Prolabo) were made using distilled water. Determined masses of the solutions were weighed out and mixed to give ratios listed in Table 4.1. Quantity of Zeolite Y for each ion-exchange was in an approximate ratio of 1:40 to the total weight of the mixture. Exact amounts of the solutions in the mixture and the corresponding weight of zeolite Y are listed in Table 4.1.

Zeolite Y was mixed with the $Cu^{2+}(aq)$ and $Ag^{+}(aq)$ mixture. On one sample, only copper solution was used. The ion-exchange was carried out conventionally for 23 hours under continuous stirring at room temperature. Excess solution from each sample was removed. The samples were washed three times using centrifuge for water-sample separation. Drying at 100 °C for 24 hours made the samples ready for calcination. This was done at 550 °C for 1000 minutes, using a ramp rate of 1 °C/min upon both heating and cooling. Under the entire process the samples were protected from light by coverage with aluminium foil, due to the sensitivity of silver to light.

Table 5.1 Masses of zeolite Y, Ag^{+}(aq) and Cu^{2+}(aq) solutions used for ion-exchanging.

Sample	Ag^{+} (aq) /g	Cu^{2+} (aq) /g	Zeolite Y /g	Ag^{+} (aq) / Cu^{2+} (aq)
1	11,41	163,15	4,25	1:14
2	43,13	43,78	2,00	1:1
3	83,34	20,39	2,50	4:1
4	172,52	10,20	4,25	1:17
5	345,02	5,09	8,13	1:70
6	-	20,41	0,50	-

5.1.2 Treatment of the samples prior to the ICP-MS analysis

The zeolite Y samples containing silver and/ or copper needed to be decomposed before the element analysis could be carried out. The procedure was to weight out 0.010 g sample, add 1.13 g concentrated hydrofluoric acid (HF) and 0.7 g concentrated nitric acid (HNO_3). This mixture was contained in a Teflon tube, heated to 240 °C at 50 bar in a Milestone UltraClave. After the decomposition, 0,47 g 0.1M HNO_3 was added to the mixture, before it was diluted with 120 ml distilled water. The element analyses were performed on a Finnigan Element 2 High-Resolution ICP-MS, with a sensitivity limit down to 10^9 ppm.

5.1.3 Results from the ICP-MS analysis

Results from the ICP-MS analysis are listed in Table 5.2. Obviously, varying the ratio of the solution results in varying weight percentages of silver and copper in zeolite Y.

Table 5.2 Weight percentage of silver and copper in the samples after ion exchange.

Sample	Ag (wt%)	Cu (wt%)
1	0,188	1,266
2	0,384	1,048
3	0,704	0,650
4	1,570	0,217
5	2,387	0,077
6	-	0,955

Figure 5.1 illustrates the ratio between the Cu^{2+}(aq) and Ag^{+}(aq) solutions upon ion-exchanging, and the resulting weight percentage ratio of copper and silver in zeolite Y.

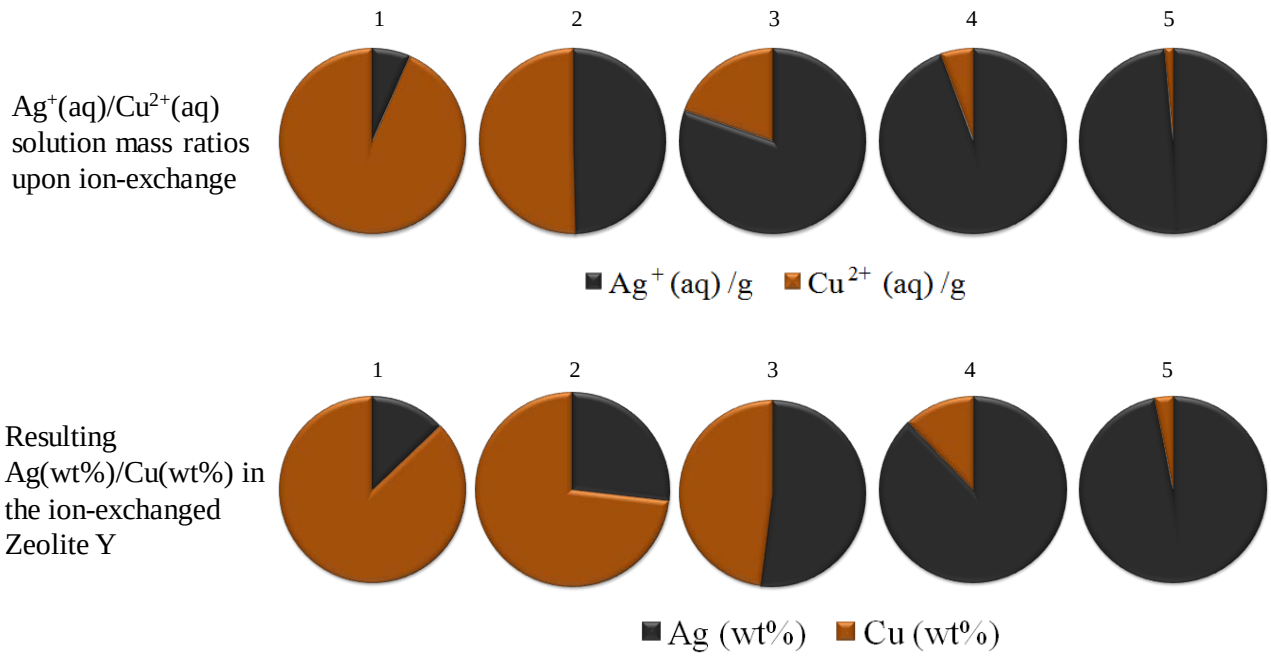

Figure 5.1 Ag^{+}(aq)/Cu^{2+}(aq) solution mass ratio with the resulting Ag/Cu wt.% ratio in zeolite Y for the 5 ion-exchanged samples.

Throughout the remaining text, the samples in Figure 5.1 are abbreviated as AgCu-Y, accompanied by the percentage share of the total ion content in the in the zeolite Y, i.e.:

1 = $Ag^{0.1}Cu^{0.9}$-Y
2 = $Ag^{0.3}Cu^{0.7}$-Y
3 = $Ag^{0.5}Cu^{0.5}$-Y
4 = $Ag^{0.9}Cu^{0.1}$-Y
5 = $Ag^{0.95}5Cu^{0.05}$-Y
The sample only containing copper is abbreviated as Cu-Y.

From Figure 5.1 it can be seen that same amount of the aqueous $Cu(NO_3)_2$ and $Ag(NO_3)$ upon ion-exchanging zeolite Y, does not lead to same weight percentages of silver and copper in the zeolite (sample 2, $Ag^{0,3}Cu^{0,7}$-Y). It was found that a mixture of 0,134 M Ag^{+}(aq) and

0,134 M Cu^{2+}(aq) in a ratio of 4:1 gives approximately equal weight percentages of silver and copper in Zeolite Y, with 0.704 wt.% and 0.650 wt.%, respectively (sample 3, $Ag^{0,5}Cu^{0,5}$-Y). Based on these results, it is reasonable to assume that silver governs the degree of copper loading in the $Ag^{x}Cu^{z}$-Y samples.

6 XAS RESULTS

In this chapter, the experimental aspects of XAS data collection are explained in section 6.1. Presentation of XAS results of the reference compounds is given in section 6.2, separately for the XANES and EXAFS regions in subsections 6.2.1 and 6.2.2, respectively.

Possible differences in the coordination of copper as a consequence of different copper and silver loadings are examined by EXAFS of the as-synthesized and in air calcined Cu-Y, $Ag^{0.1}Cu^{0.9}$-Y and $Ag^{0.5}Cu^{0.5}$-Y in section 6.3.

The redox properties of copper in Cu-Y and $Ag^{0.5}Cu^{0.5}$-Y samples were examined by in-situ XAS, exposing the samples to hydrogen while heated and subsequently to NO while cooled. Both qualitative and quantitative XANES analysis was performed by comparison with the reference compounds. These results are presented in section 6.4.

EXAFS from different temperature stages during hydrogen treatment was analyzed to examine change in multiplicity and bond lengths of copper upon reduction in the Cu-Y and $Ag^{0.5}Cu^{0.5}$-Y samples. The results are given in section 6.5.

6.1 Experimental section

6.1.1 X-ray absorption data collection

The samples were prepared as described in section 5.1.1. XAS data for samples containing both silver and copper (Ag^xCu^z-Y) were collected at the Swiss-Norwegian Beamline (BM1B) at the European Synchrotron Radiation Facility (ESFR). The Cu K-edge data were measured in transmission mode. The synchrotron was operating at 6 GeV. The BM1B station was equipped with a water-cooled double-crystal monochromator, with flat Si[111] pair and flat Si[311] pair monochromator crystals. Higher order harmonics were removed with Cr coated mirror during Cu K-edge scan collection.

The BM1B station was also supplied with 30 cm long ionisation chambers for transmission experiments. When Cu K-edge data were collected, intensity detector for the incident beam

was filled with 100% N_2. Intensity detectors for the transmitted beam from the sample and the foil were both filled with 65 % N_2 and 35% air.

XAS data for the sample only containing copper (Cu-Y) were collected at Materials Science Beamline I811, MAX-lab in transmission mode. The I811 station was equipped with a water-cooled double-crystal monochromator, with interchangeable pairs of Si[111] and Si[311] monochromator crystals. Higher order harmonics were removed with Rh coated mirror during Cu K-edge scan collection.

Grounded samples, for which data were collected at ambient temperature and atmosphere, were placed in aluminium holders with a thickness of 2 mm. The sample was sealed and held in place by X-ray transparent Kapton tape. An illustration of a prepared sample is shown in Figure 6.1.

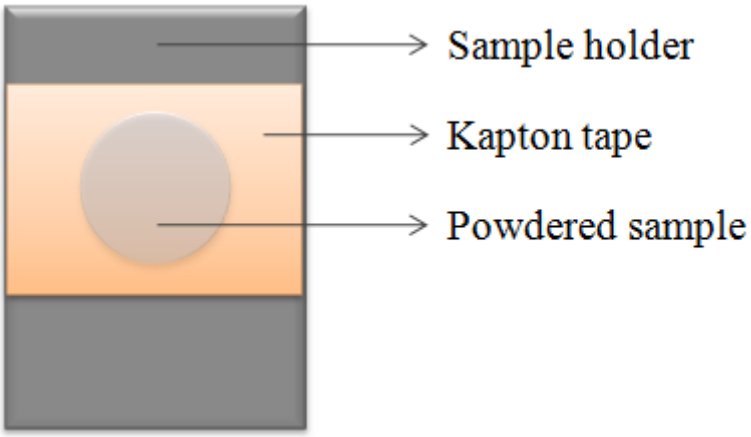

Figure 6.1 Prepared sample for room-temperature data collection

In-situ measurements [1]

Real systems with a catalyst put into operation can be simulated by an in-situ experimental setup. Such a setup allows various conditions to be applied to a sample; both the temperature and altered gas flows can be carefully controlled. The experimental setup is illustrated in Figure 6.2. The in-situ cell is connected to a temperature controller and a gas tube. For all in-

situ measurements performed in this work, the cell illustrated in Figure 6.3 was used for the in-situ measurements. The sample catalyst was grounded to small particles before pressed into the sample container of the cell. On each side of the powdered sample, quartz wool was placed in order to prevent clogging of the gas inlet and outlet. Graphite windows were used to hold the sample in place.

To remove water and clear the pores, the sample was heated in helium to 160 °C. The gas flow was thereafter switched to hydrogen (5% H_2 + 95 % He) with gradual heating up to 500 °C. At this temperature, the gas was switched to NO (5% NO + 95 % He) while the sample was cooled to room temperature. The gas flow rate was 15 ml/min. XAS scans were collected at different temperatue stages. All XANES spectra were energy corrected against a copper-foil (8979 eV) calibration.

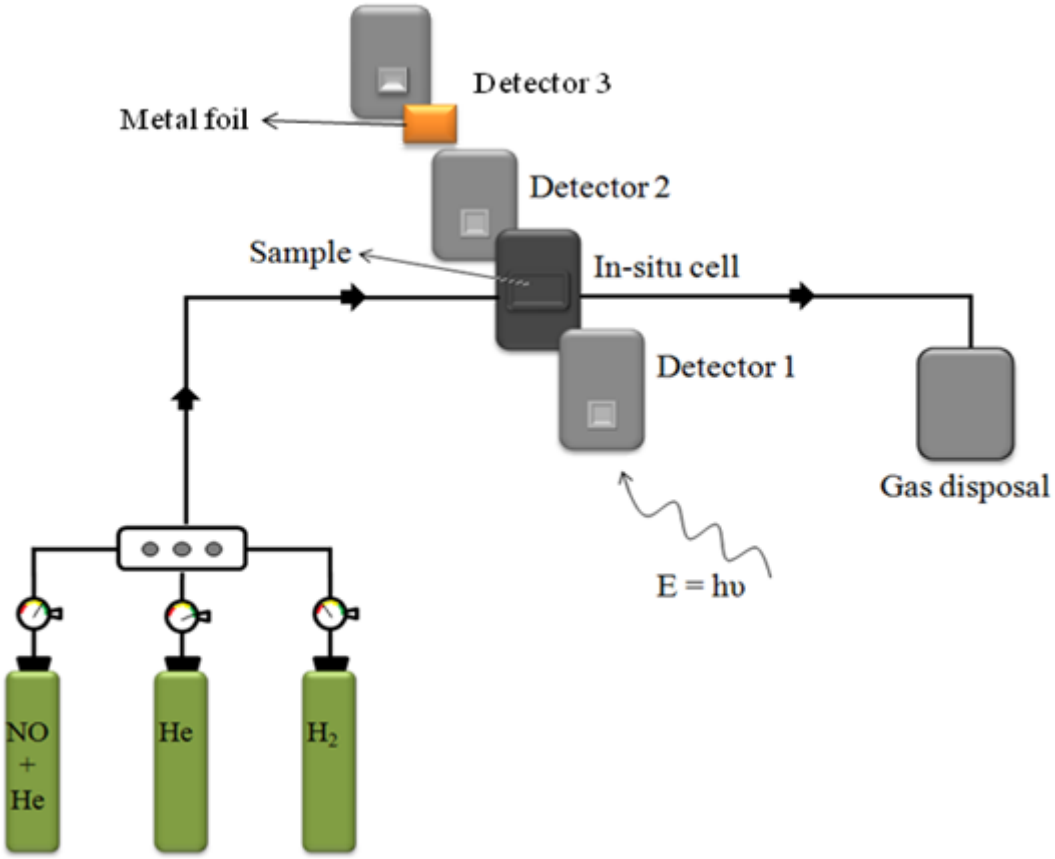

Figure 6.2 Experimental setup for in-situ measurements.

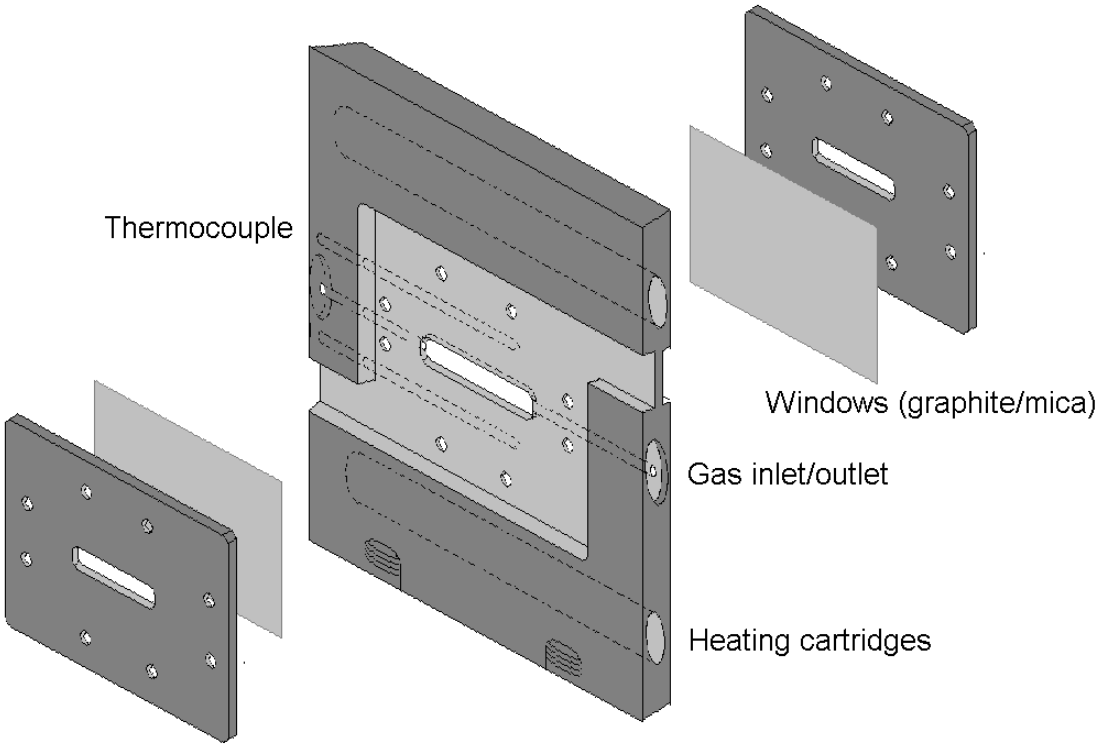

Figure 6.3 In-situ cell with the graphite windows. Unpublished illustration by Karina Mathisen.

6.2 XAS Results of the Model Compounds

In order to determine the oxidation state of copper in the unknown samples during the in-situ measurement, it is necessary to compare XANES regions of the unknown with XANES of appropriate reference compounds.

When it comes to EXAFS analysis, it is usual to start off with several model compounds of known structure. Ideally, the models are close related to the unknown samples regarding types of backscatters and structure. When the EXAFS of a model compound was refined in EXCURV98, the multiplicities were taken from references and were held fixed during refinement. The obtained value of amplitude reduction factor, AFAC, was subsequently transferred to the unknown samples.

6.2.1 XANES of the model compounds

For qualitative and quantitative analysis of the Cu K-edge XANES data, copper(II) oxide (CuO), copper(I) oxide (Cu_2O), copper(II)–Tutton salt ($Cu(NH_4)_2(SO_4)_2 \cdot 6H_2O$) and diamminecopper(I) ($[Cu(NH_3)_2]^+$) were used as reference compounds. Figure 6.4 shows normalized Cu K-edge XANES and their first derivatives of these references, in addition to copper foil. The environment of copper in Copper(II)–Tutton salt was chosen because it bears closest resemblance to the copper environment in the as-prepared samples. When the samples were exposed to thermal treatment in reducing and oxidizing environments, copper species formed were closest resembled by copper foil and copper oxides.

The very weak 8979-eV peak seen in XANES of both CuO and copper(II) – Tutton salt (Figure 6.1 a) and b) respectively) is associated with the formally forbidden 1s→ 3d transition [2,3]. The low intensity of this peak is an evidence of a centrosymmetric copper environment, e.g. tetragonally-distorted octahedral [4]. In addition, CuO exhibit a broad peak on the absorption edge petering out below 8985 eV. This feature is assigned to either 1s→ 4s or 1s → 4p, as it remains controversial [2].

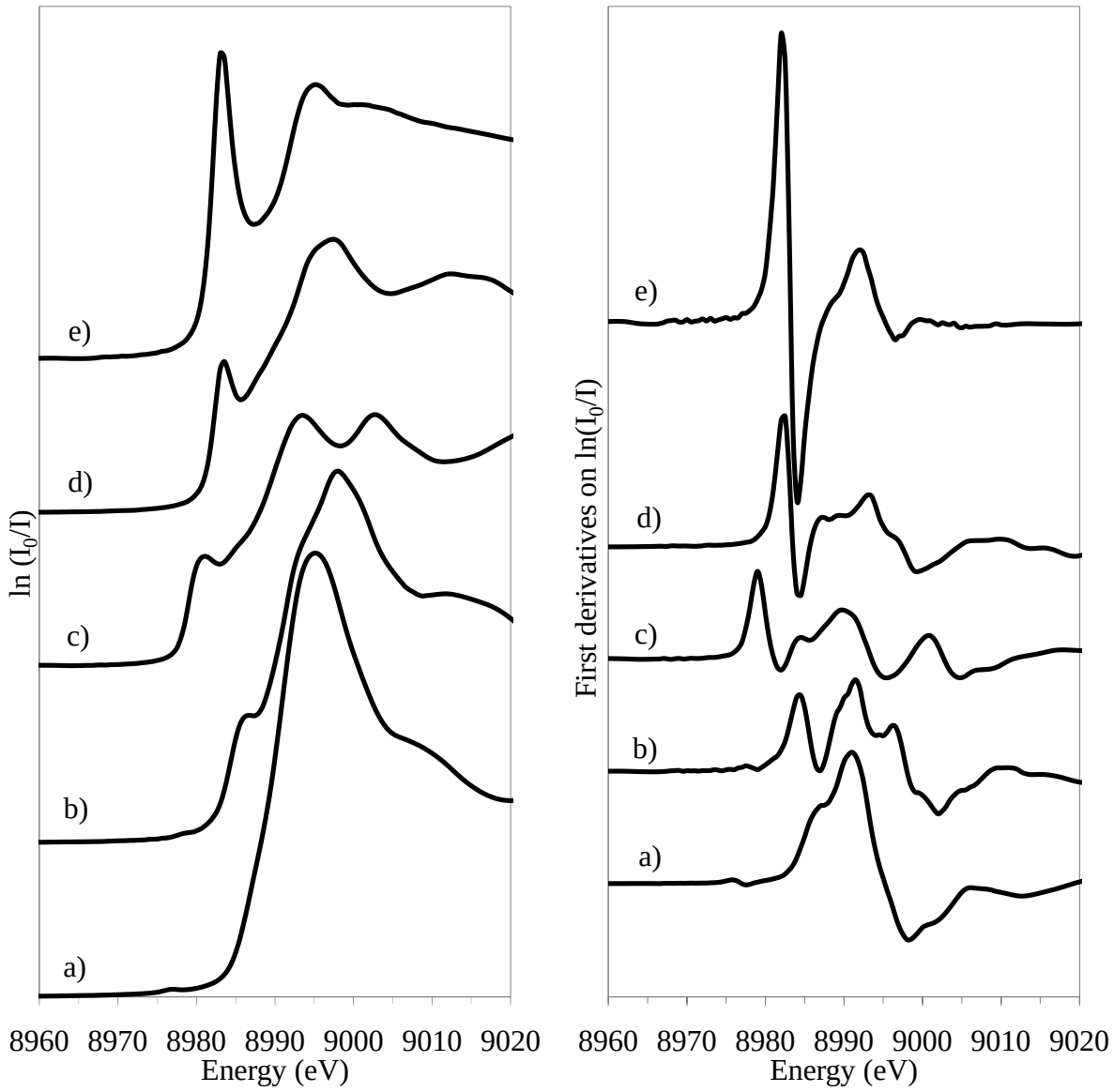

Figure 6.4 Normalized Cu K-edge XANES and first derivatives of (a) copper(II) – Tutton salt; (b) copper(II) oxide; (c) copper foil; (d) copper(I) oxide and (e) diamminecopper (II).

XANES spectra of the Cu(I) and Cu(II) reference compounds are readily distinguished as the former exhibit a pre-edge peak within the range 8983-8984 eV. The intensities and accurate positions are correlated with coordination number. Pre-edge features in the range 8983-8984 eV are seen in XANES for both copper(I) oxide and diamminecopper(I) (Figure 6.1 d) and e) respectively). These peaks are assigned empirically as a ~~C~~u4s1stransition, and

correspond to a two-coordinate and linear structure in both compounds [5]. Thus, Cu_2O is coordinated by two oxygen atoms, whilst $[Cu(NH_3)_2]^+$) is coordinated by two nitrogen atoms.

6.2.2 EXAFS of the model compounds

XAS data of the unknown samples were collected at Swiss-Norwegian Beamline (BM1B) and MAX-lab. To establish the amplitude reduction parameter AFAC, copper(II) oxide and copper(II)–Tutton salt were used as model compounds. XAS data of these models were collected under the same settings as for the samples. The k^3-weighted curve-fitted EXAFS (and the corresponding Fourier transform) of the models extracted from XAS data collected at SNBL are shown in Figures 6.5 and 6.6. XAS data recorded at MAX-lab are shown in figure 6.7 and 6.8 for the two models. The refined parameters from the analyses are listed in Table 6.1 and 6.2.

Table 6.1 Refined parameters for Cu K-edge data for CuO and copper – Tutton salt. AFAC = 0.8631 for CuO and 0.8208 for Cu-Tutton Salt. k-range: 2-12 $Å^{-1}$. (Data collected at SNBL).

Sample	Shell	N[a]	r (Å)	r, XRD (Å)[a]	$2\sigma^2$ ($Å^2$)	R (%)
CuO	Cu–O	4.0	1.958 (6)	1.96	0.009 (1)	37.21
	Cu–O[b]	2.0	-	2.78		
	Cu···Cu	8.0	2.936 (9)	2.90	0.026 (2)	
	Cu···Cu	2.0	3.137 (7)	3.08	0.007 (1)	
	Cu···Cu	2.0	3.45 (4)	3.42	0.026 (9)	
$Cu(NH_4)_2(SO_4)_2 \cdot 6H_2O$	Cu–O	4.0	1.971(5)	2.02	0.0119 (9)	25.62
(Cu-Tutton Salt)	Cu–O	2.0	2.23 (2)	2.23	0.036 (1)	

[a] The fixed multiplicities and crystallographic distances are taken from reference [3]. [b] Not fitted.

As seen from Tables 6.1 and 6.2, the AFAC values for CuO and copper – Tutton salt from both synchrotron stations are within the 0.8 – 1 range. The EXAFS results of copper(II) oxide agree fairly well with the crystallographic data. CuO has a well-defined structure where the copper atom is surrounded by four close coplanar and two distant oxygen atoms, giving a distorted octahedron [6]. The elongated Cu–O of 2.78 Å was not fitted. In the Fourier transform, this distance is not noticeable. Trying to include the elongated Cu–O distance when fitting, lead to high R-factor and Debye – Waller factor.

Table 6.2 Refined parameters for Cu K-edge data for CuO and copper – Tutton salt. AFAC = 0.9000 for CuO and 0.8330 for Cu-Tutton Salt. k-range: 2-12 $Å^{-1}$. (Data collected at MAX-lab).

Sample	Shell	N[a]	r (Å)	r, XRD (Å)[a]	$2\sigma^2$ ($Å^2$)	R (%)
CuO	Cu–O	4.0	1.963(6)	1.96	0.009(1)	37.03
	Cu–O[b]	2.0	-	2.78		
	Cu···Cu	8.0	2.950(9)	2.90	0.027(2)	
	Cu···Cu	2.0	3.140(8)	3.08	0.006(1)	
	Cu···Cu	2.0	3.3(1)	3.42	0.04 (3)	
$Cu(NH_4)_2(SO_4)_2 \cdot 6\ H_2O$	Cu–O	4.0	1.976(6)	2.02	0.012 (1)	27.72
(Cu-Tutton Salt)	Cu–O	2.0	2.23(2)	2.23	0.03(1)	

[a] The fixed multiplicities and crystallographic distances are taken from reference [3]. [b] Not fitted.

The copper atom in copper–Tutton salt also has a six–coordinated structure, with water molecules as ligands, with four equatorial and two axial Cu–O bonds [4]. The latter Cu–O bonds are shorter than in copper(II) oxide, and cannot be resolved from the four equatorial Cu–O bonds in the EXAFS spectra. However, they were still fitted in the EXAFS, agreeing with the crystallographic data. The fitted EXAFS of the four Cu–O equatorial bonds gave a distance of 1.971 Å (SNBL) and 1.976 (MAX-lab). These values are slightly low compared to the crystallographic data. The fitting procedure in EXCURV98 of copper–Tutton offered a few complications when it came to obtaining reasonable values. The somewhat low Cu–O distances might be due to the correlation between the R and E_F parameters. Taking into account that the standard deviation for small bonding distances is ±0.01 in case of high correlations, and comparing these values to the one of 1.980 Å obtained by Mathisen et.al. [4], they can be said to be within an acceptable range.

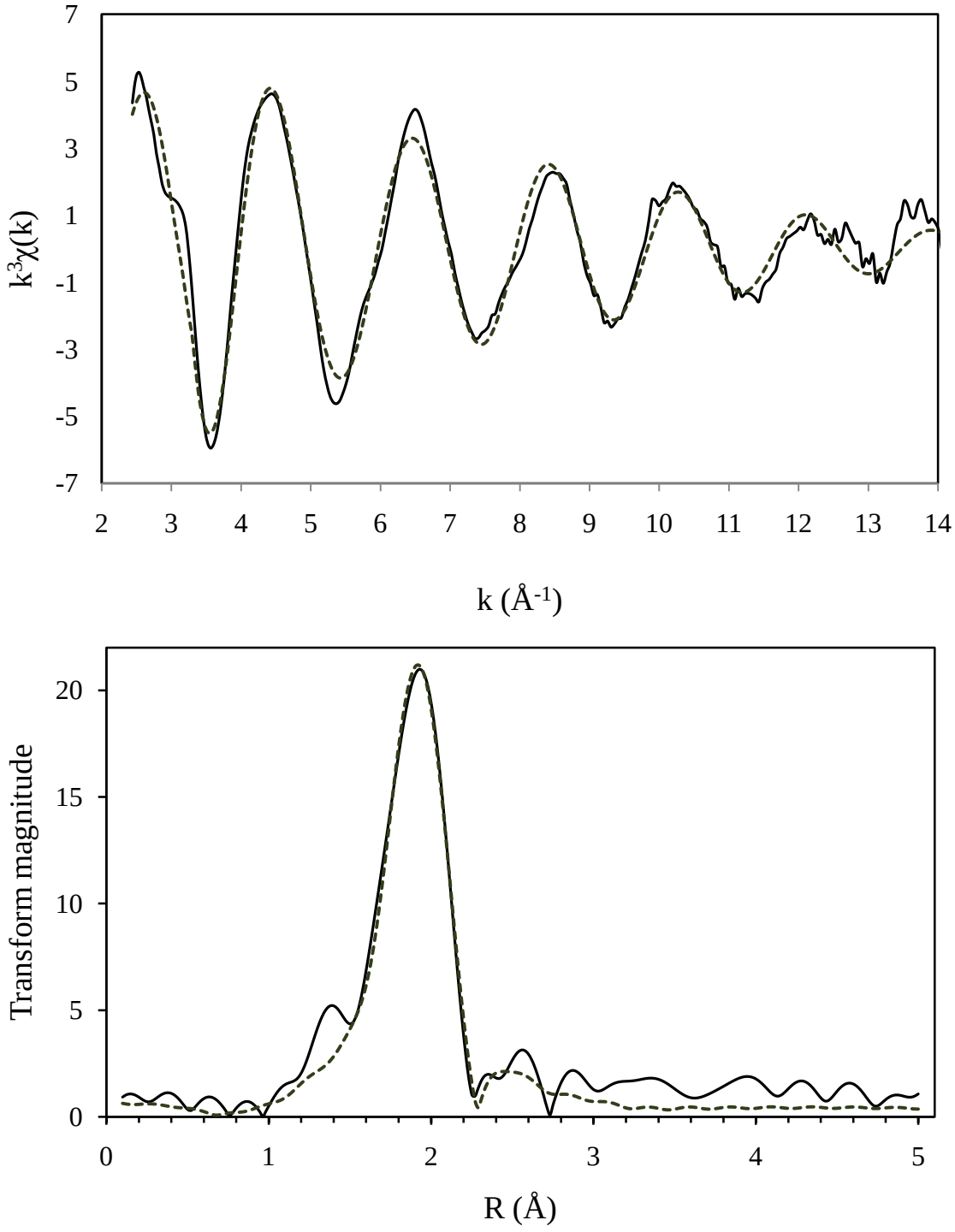

Figure 6.5 Background subtracted and k^3-weighted EXAFS spectrum and its Fourier transform for copper(II) –Tutton salt. Experimental (—) and calculated (---). (Data from SNBL).

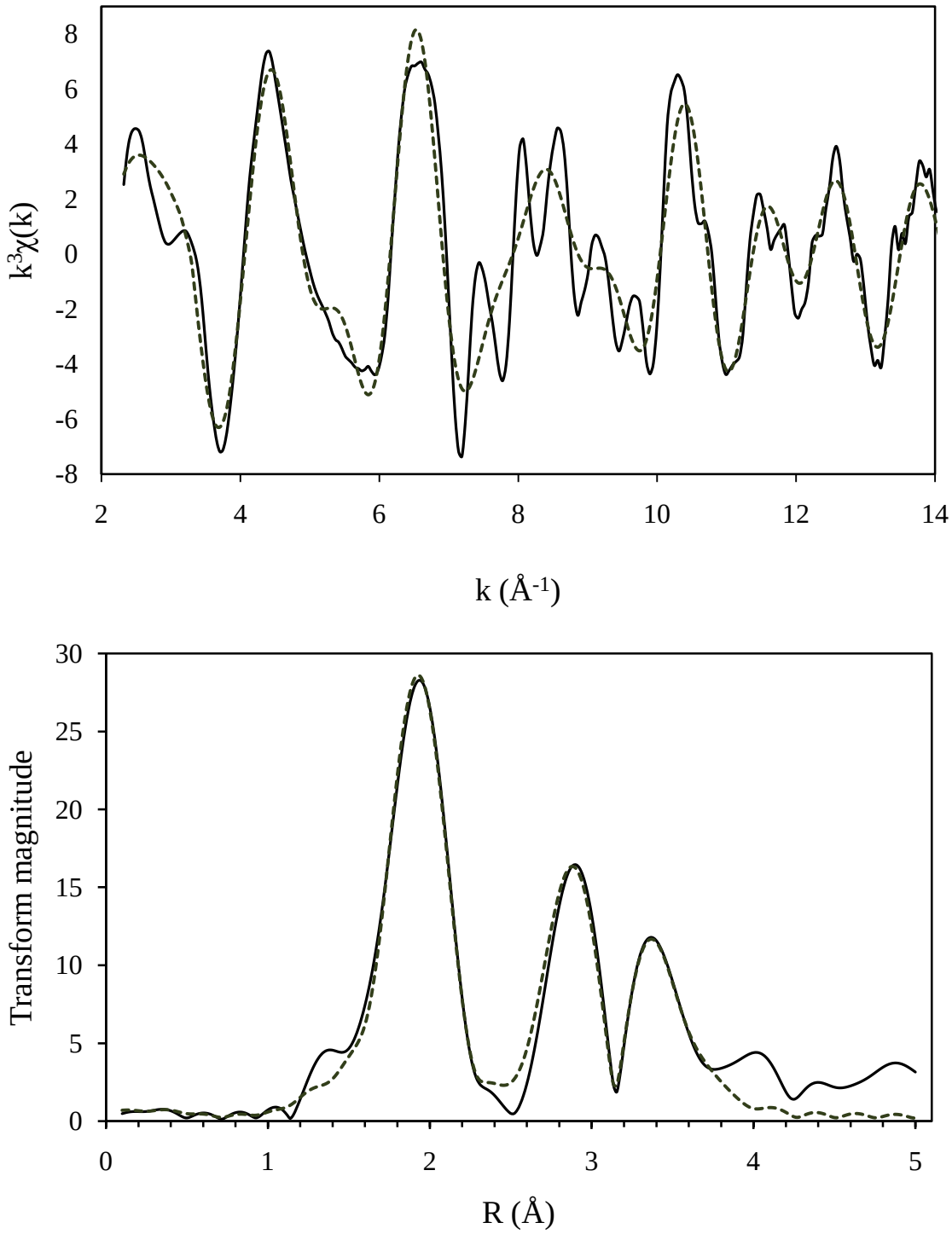

Figure 6.6 Background subtracted and k^3- weighted EXAFS spectrum and its Fourier transform for CuO. Experimental (—) and calculated (---). (Data from SNBL).

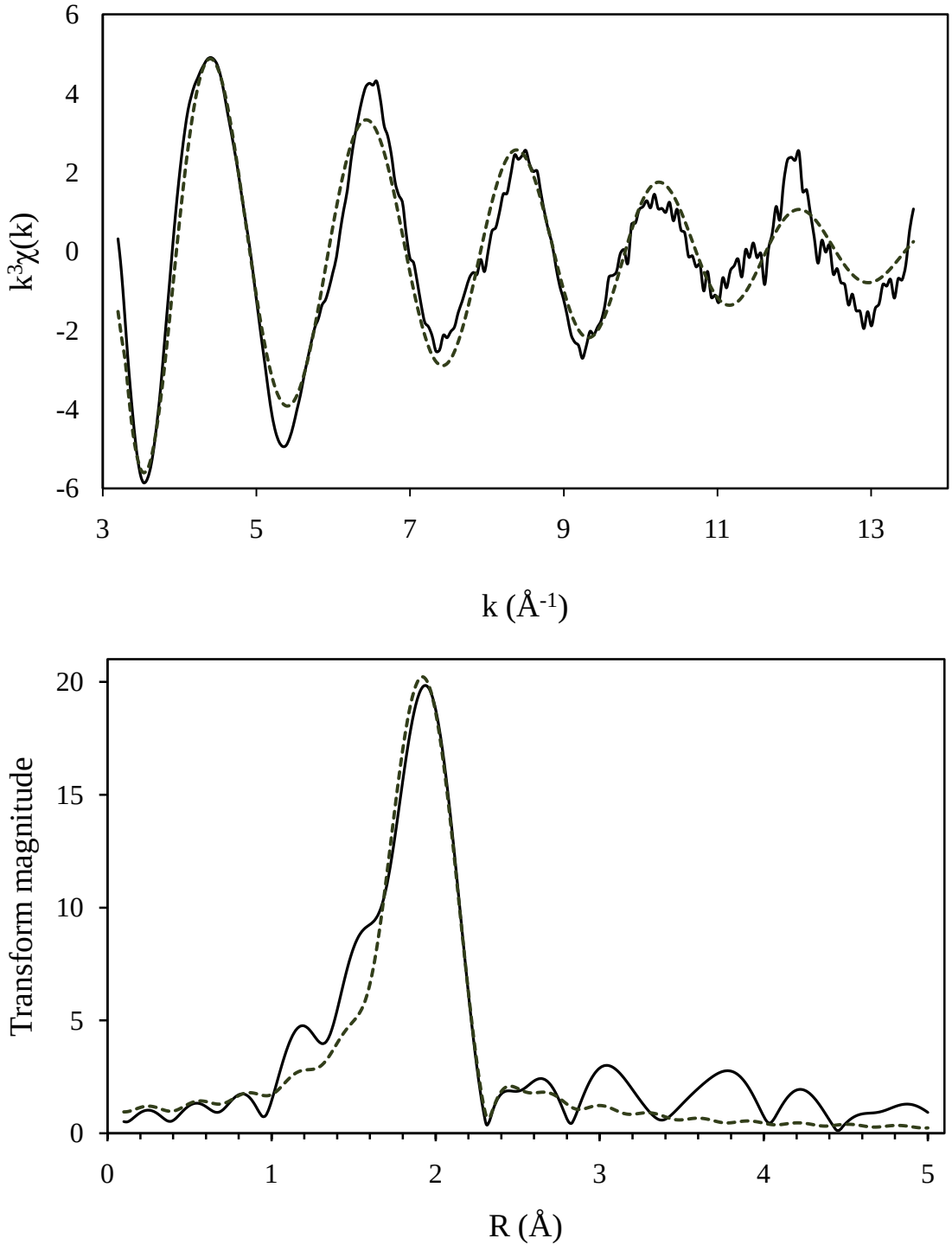

Figure 6.7 Background subtracted and k^3 -weight EXAFS spectrum and its Fourier transform for copper(II) –Tutton salt. Experimental (—) and calculated (---). (Data from MAX-lab).

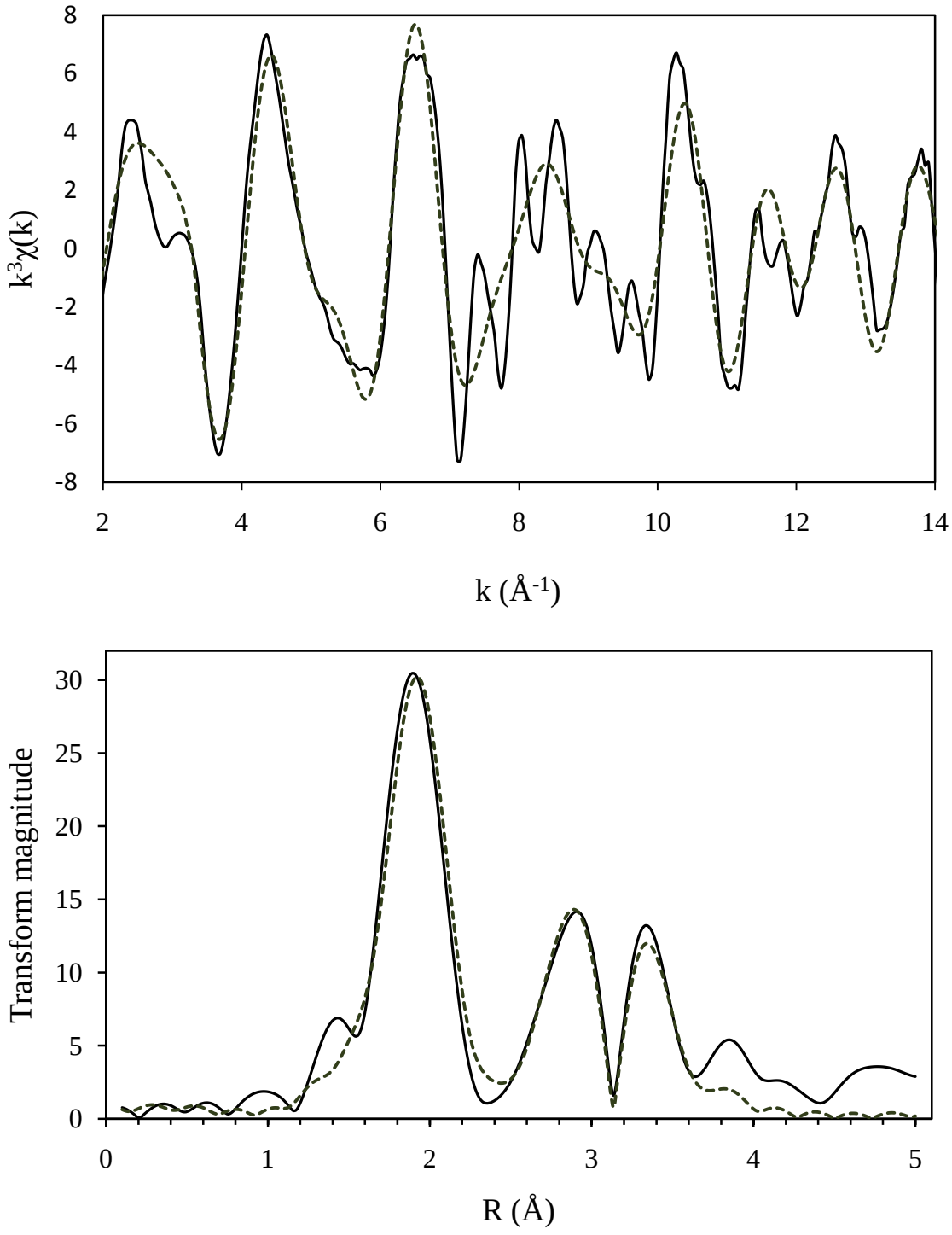

Figure 6.8 Background subtracted and k^3- weighted EXAFS spectrum and its Fourier transform for CuO. Experimental (—) and calculated (---). (Data from MAX-lab).

6.3 EXAFS of Cu-Y, $Ag^{0.1}Cu^{0.9}Y$, and $Ag^{0.5}Cu^{0.5}Y$

In order to examine possible differences in the coordination of copper as a consequence of different copper and silver loadings, XAS data of the as-synthesized and in air calcined Cu-Y, $Ag^{0.1}Cu^{0.9}$-Y and $Ag^{0.5}Cu^{0.5}$-Y samples were collected at ambient temperature and atmosphere. The k^3-weighted curve-fitted EXAFS of the samples with Fourier transforms are shown in figures 6.9, 6.10 and 6.11. Parameters from the least-square analyses of the EXAFS are listed in table 6.3 for all three samples.

Table 6.3 Table 6.7 Parameters from the Least Squares EXAFS analysis for as-synthesized and calcined Cu-Y, $Ag^{0.1}Cu^{0.9}$-Y and $Ag^{0.5}Cu^{0.5}$-Y[a,b)]

Sample	Shell	N	r (Å)	$2\sigma^2$ (Å^2)	R (%)
Cu-Y	Cu–O	2.8(2)	1.946(7)	0.002(2)	31.96
$Ag^{0.1}Cu^{0.9}$-Y	Cu–O	4.6 (2)	1.951 (4)	0.012(5)	15.31
$Ag^{0.5}Cu^{0.5}$-Y	Cu–O	4.6(3)	1.948 (5)	0.013(2)	17.55

a) k – range: 2 – 10 Å^{-1}. b) Standard deviation in the last significant digit as calculated by EXCURV 98 is given in parentheses.

EXAFS of Cu-Y shows 2.8(2) Cu–O distances at 1.946(7) Å. This is in accordance with the findings of Palomino et.al. [7], who also found a multiplicity of 2.8 in copper exchanged zeolite Y, although with a longer Cu–O bond (1.99 Å). This excludes copper to be found at sites I and III, as the copper cation in these sites is six-coordinated and four-coordinated, respectively (see section 1.2.2). Cations in the remaining sites of zeolite Y (I', II and II') are three-coordinated. Thus, copper in the Cu-Y sample is located in one of these sites. The exact location is not possible to determine from these results only. Further examination by EXAFS is needed. Choosing the aluminum as the target atom in the Cu-Y could give more extensive information about copper. Unfortunately, data about aluminum in the samples were not collected in this thesis due to late discovery of the need for doing so.

Simultaneous ion-exchange with silver and copper yields different coordination about copper in zeolite Y. EXAFS reveals 4.6 Cu–O distances when silver is present. Differences in this bond distance are minor for the Cu-Y and Ag^xCu^z-Y samples. With the multiplicity of 4.6,

copper cannot be excluded from the sites I and III, nor the remaining I', II and II' in the Ag^xCu^z-Y samples.

Comparing the $Ag^{0.1}Cu^{0.9}$-Y and $Ag^{0.5}Cu^{0.5}$-Y samples there is no difference in the multiplicities. In both, copper is coordinated to 4.6 oxygen atoms, with a minor difference in the bond distances (1.951(4) and 1.948(5), respectively). Provided that silver is present, copper adopts the same coordination, independently of the copper or silver loading in zeolite Y. However, the least squares fitting of $Ag^{0.1}Cu^{0.9}$-Y EXAFS gives a lower *R*-factor than $Ag^{0.5}Cu^{0.5}$-Y. This is due to lower copper content in the latter, resulting in lower signal to noise ratio.

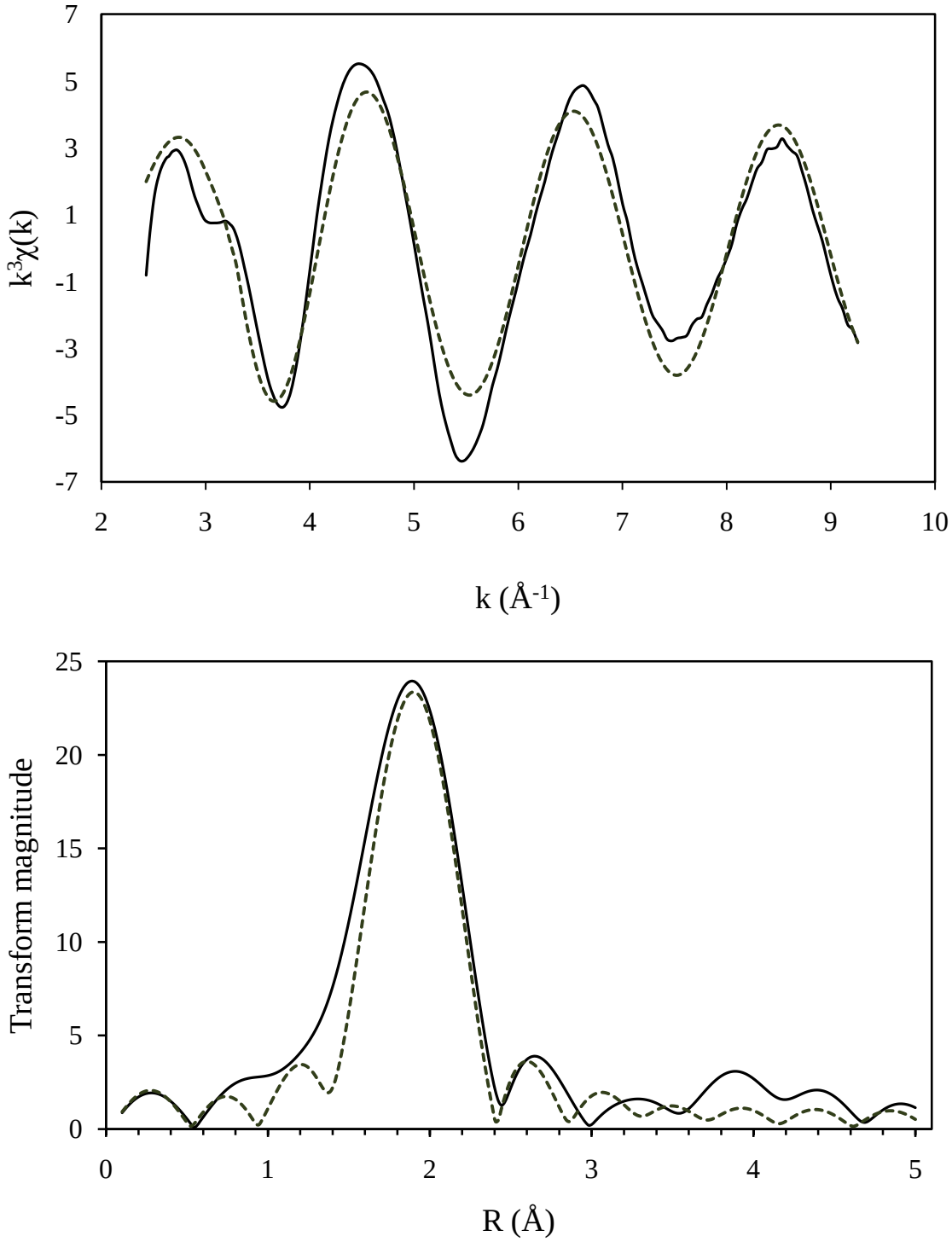

Figure 6.9 Experimental (—) and calculated (---) k^3-weighted EXAFS and its Fourier transform for Cu-Y as-prepared.

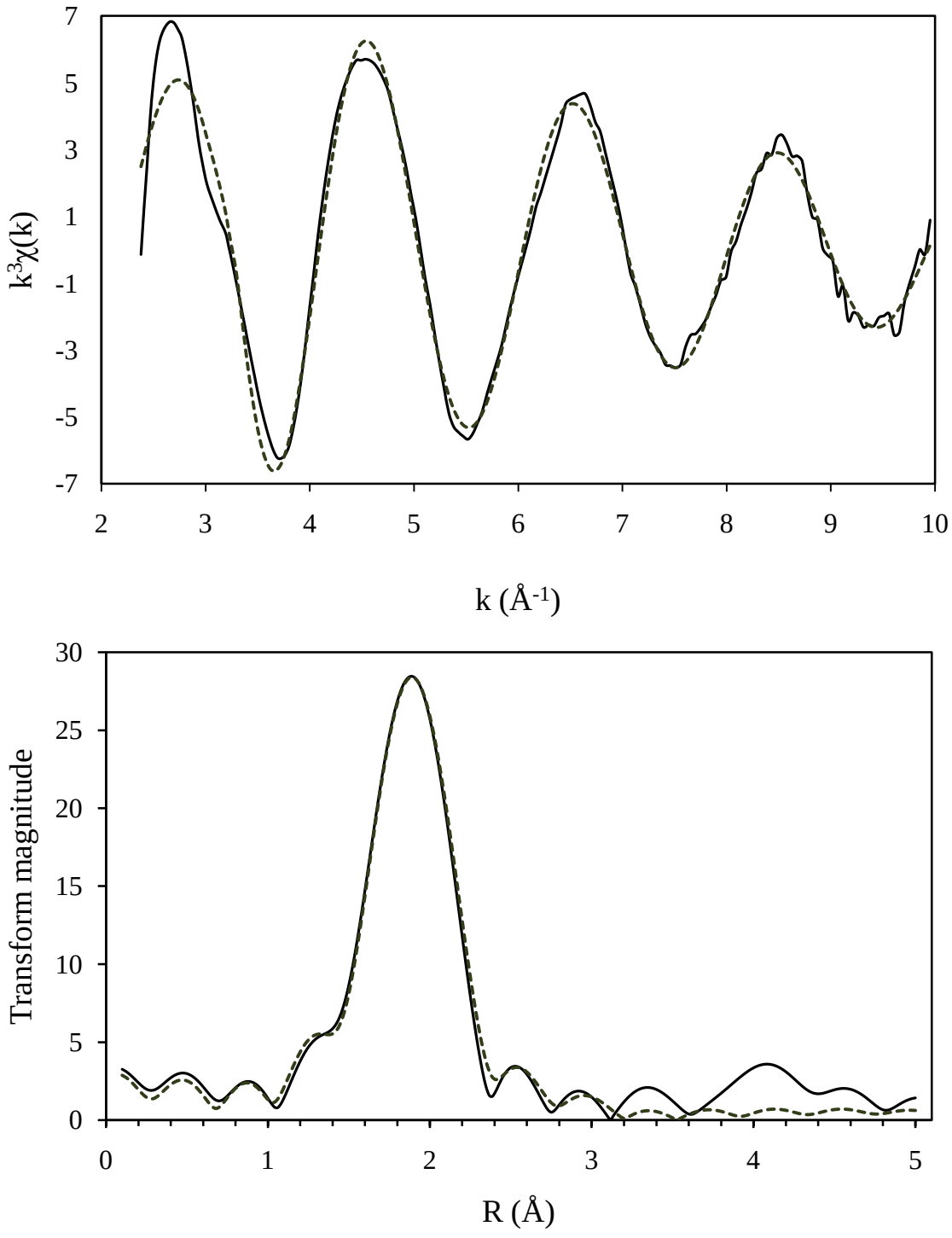

Figure 6.10 Experimental (—) and calculated (---) k^3-weighted EXAFS and its Fourier transform for $Ag^{0.1}Cu^{0.9}$-Y as-prepared.

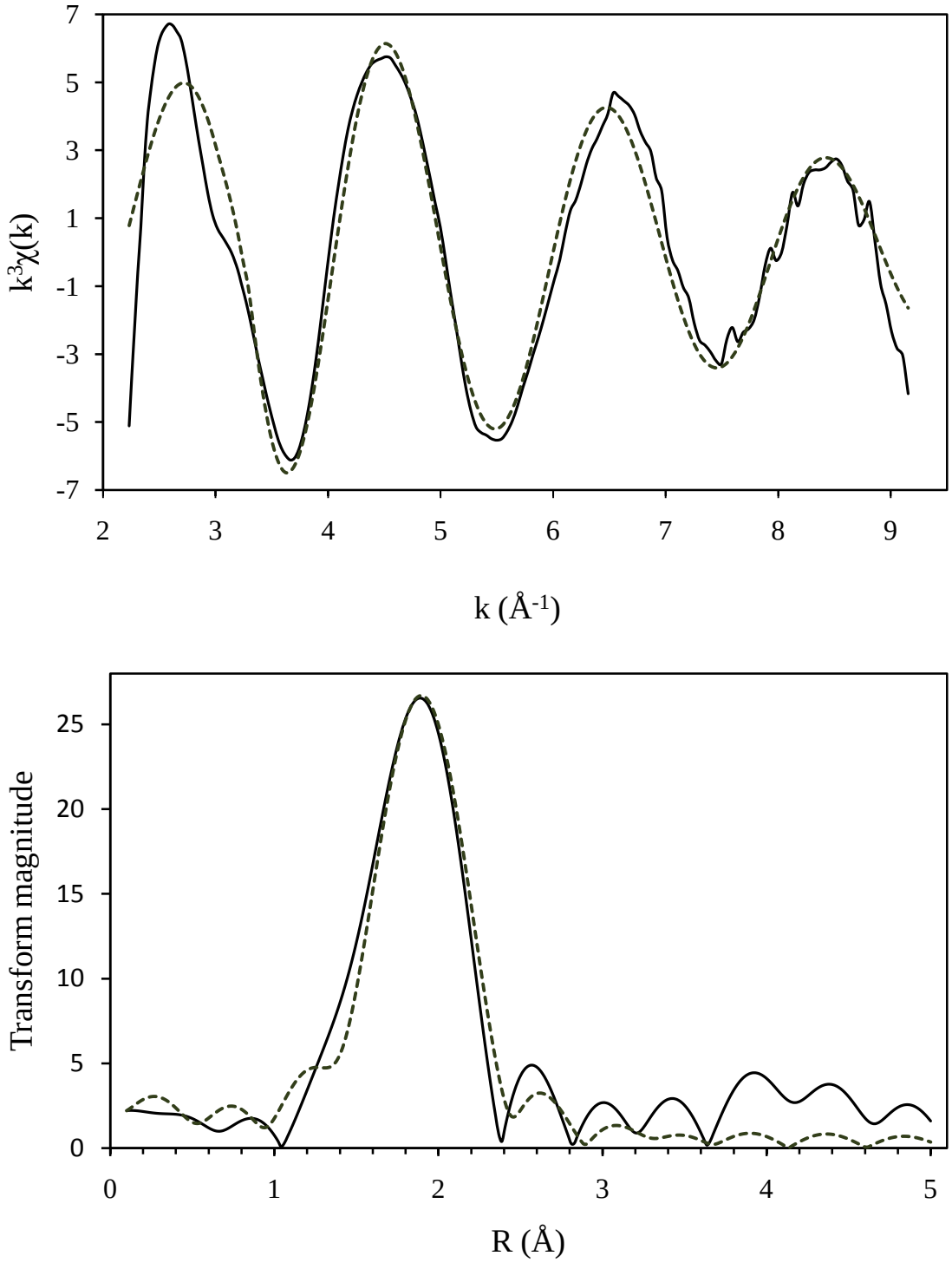

Figure 6.11 Experimental (—) and calculated (---) k^3-weighted EXAFS and its Fourier transform for $Ag^{0.5}Cu^{0.5}$-Y as-prepared.

6.4 XAS results from the In-Situ measurements of Cu-Y and $Ag^{0.5}Cu^{0.5}$-Y

Yahiro and Iwamoto [8] proposed that the redox properties of copper-zeolites can be attributed to their catalytic activity in the decomposition/reduction of NO_x, where the Cu(I) species participate in the reaction. The redox properties of copper in Cu-Y and $Ag^{0.5}Cu^{0.5}$-Y samples were examined by in-situ XAS, exposing the samples to hydrogen and subsequently to NO. The results can give an indication of the reducibility and reversibility of the copper valence state in presence and absence of silver. Procedure for in-situ XAS measurements was described in section 6.1.1.

From the samples with both silver and copper, the sample with equal weight percentage of copper and silver ($Ag^{0.5}Cu^{0.5}$-Y) was chosen in order to eliminate effects of a dominating ion. This makes comparison with Cu-Y more reasonable. Results from the in-situ measurements are presented in following sections.

6.4.1 Qualitative analysis of XANES from in-situ measurements of Cu-Y

XANES spectra from the in-situ measurements of Cu-Y are divided into three parts following the experimental sequence. Normalized Cu-edge XANES and first derivatives from the initial reaction stage, when heated in helium (20 – 130 °C), are shown in Figure 6.12. Figure 6.13 shows the normalized Cu-edge XANES and their first derivatives when heated in hydrogen (120 – 500 °C). Normalized Cu-edge XANES and their first derivative upon cooling in nitrogen oxide (500 – 20 °C) is shown in Figure 6.14. A vertical line at 8985 eV is drawn in the figures 6.13 and 6.14 to distinguish the Cu(I) from the Cu(II) pre-edge feature.

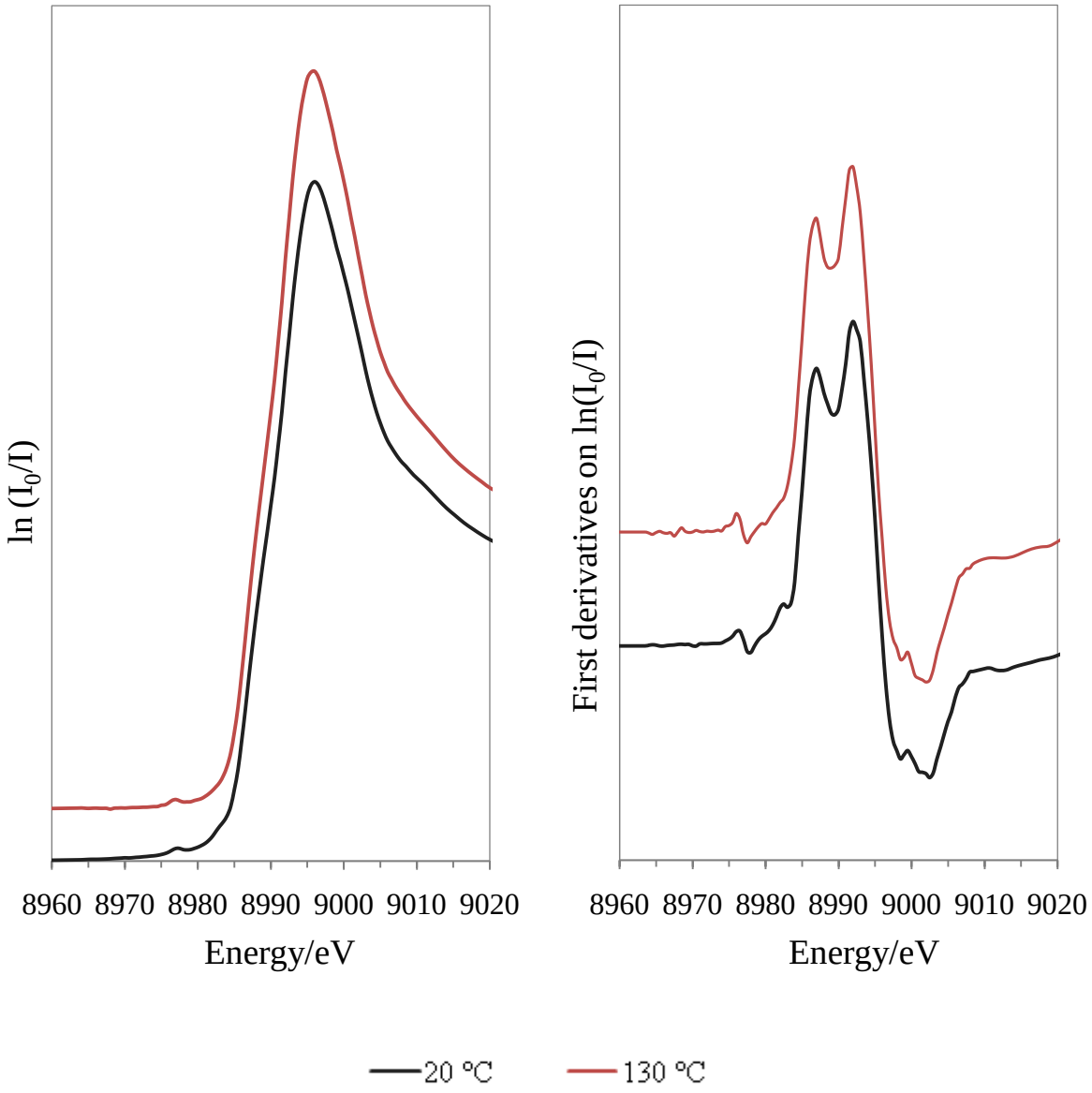

Figure 6.12 Normalized Cu-edge XANES and first derivatives of Cu-Y during thermal treatment in helium (20 – 130 °C).

Upon heating Cu-Y in helium, two spectra were recorded. The weak rise in absorption at about 8977 eV is attributed to the dipole-forbidden 1s → 3d transition. Therefore, the copper present in the sample is in oxidation state of +2.

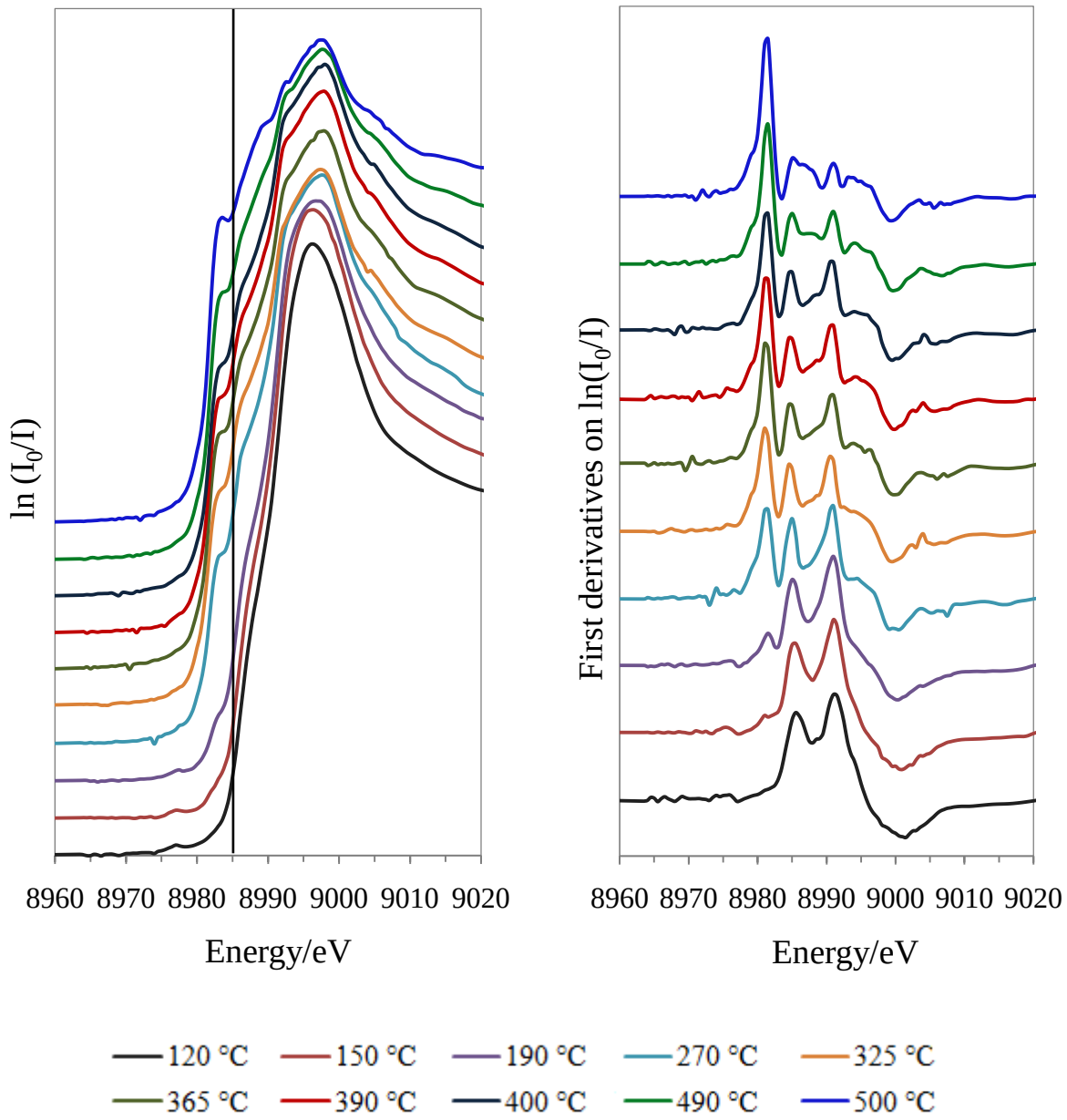

Figure 6.13 Normalized Cu-edge XANES and first derivatives of Cu-Y during thermal treatment in hydrogen (120 – 500 °C).

The weak absorption at 8977 eV is found in the first three XANES of thermal treatment in hydrogen (Figure 6.13), evidencing presence of Cu(II). In the XANES of 190 °C, the weak absorption at 8977 eV is no longer apparent. Next spectrum (270 °C) shows a distinctive change from the previous as a shoulder appears at 8983 eV on the absorption edge. This shoulder is seen in the remaining spectra with increasing temperature, with highest intensity in the XANES of 500 °C. The 8983 eV pre-edge is characteristic for Cu(I), implying

reduction of Cu(I) in Cu-Y. Formation of metallic copper is not evident in the XANES from the hydrogen stage. The shapes of the 500 °C XANES and XANES of copper foil (Figure 6.4) do not match very well.

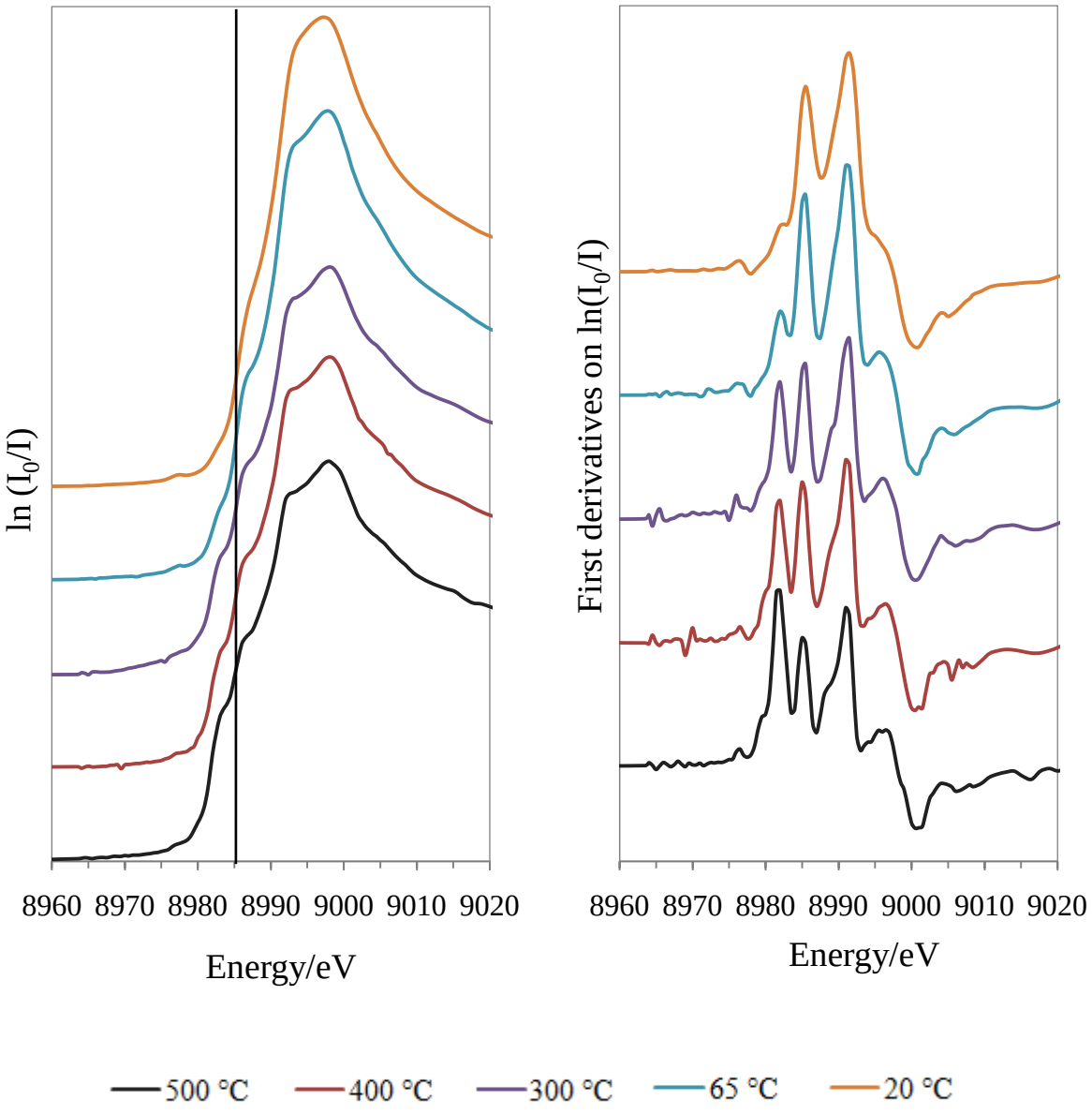

Figure 6.14 Normalized Cu-edge XANES and first derivatives of Cu-Y during cooling in NO (500 – 20 °C).

Concerning the XANES from cooling in NO (Figure 6.14), it is clear from the spectrum of 500 °C, and especially its derivative, that multiple valence states are present. In this spectrum, both the Cu(I) and Cu(II) characteristic pre-edges are present at 8983 eV and above 8985 eV,

respectively. The shoulder of Cu(I) disappears upon cooling and is no longer visible at the XANES of 65 °C. The feature of Cu(II) at 8985 eV remains present in all of the XANES. This is an indication of copper(I) being re-oxidized to the divalent state. Re-emergence of the weak 8977 eV peak, characteristic for Cu(II) compounds, is seen in XANES of 65 °C and 20 °C. Also worth noticing is the Cu-Y XANES of 20 °C; its derivative matches the one of 20 °C in helium in Figure 6.12. These are all indication of copper being re-oxidized.

6.4.2 Qualitative analysis of XANES from in-situ measurements of $Ag^{0.5}Cu^{0.5}$-Y

XANES from the in-situ measurements of $Ag^{0.5}Cu^{0.5}$-Y are divided into three parts, in accordance with the experimental sequence. Figure 6.15 shows the normalized Cu-edge XANES and their first derivatives during treatment in helium with increasing temperature (20 – 160 °C). Figure 6.16 shows the normalized Cu-edge XANES and their first derivatives during thermal treatment in hydrogen (95 – 490 °C). Figure 6.17 shows the normalized Cu-edge XANES and their first derivatives from treatment in nitrogen oxide with decreasing temperature (500 - 65 °C). A vertical line at 8985 eV is drawn figures 6.16 and 6.17 to distinguish the Cu(I) and Cu(II) pre-edge features.

Each and all XANES spectra collected during helium flow and heating exhibit a low intensity peak at about 8977 eV. This feature confirms that Cu(II) is initially present in the sample. At 155 °C, a weak shoulder above 8985 eV appears. This is even more visible in the 160 °C XANES, especially in its derivative. Resembling to a certain degree the one of copper(II) oxide, it might indicate a heterogeneous distribution of copper species in $Ag^{0.5}Cu^{0.5}$-Y and presence of small amounts of CuO.

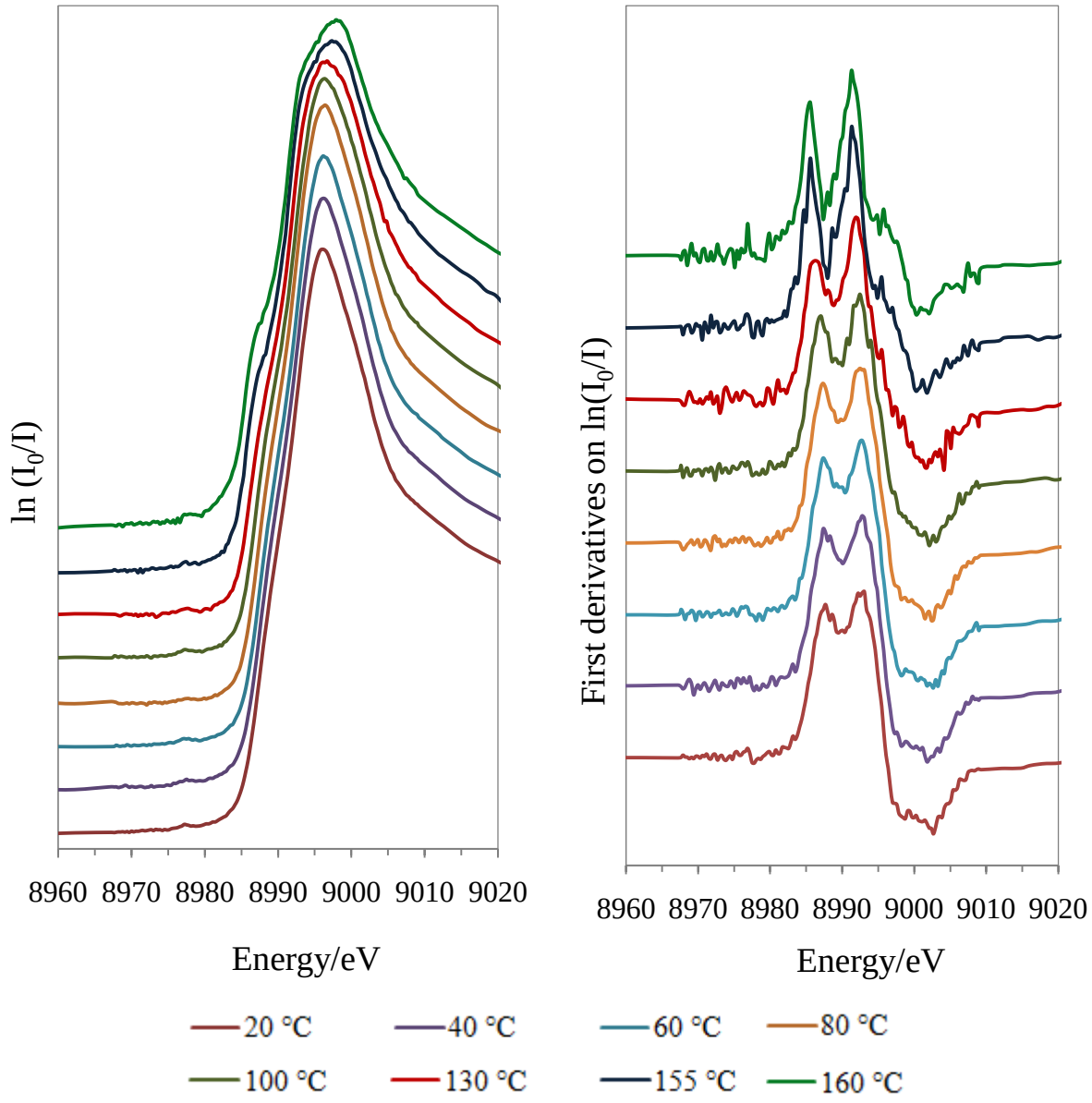

Figure 6.15 Normalized Cu-edge XANES and first derivatives of $Ag^{0.5}Cu^{0.5}$-Y during thermal treatment in helium (20 – 160 °C).

Moving on to the XANES collected during hydrogen flow and heating, the low intensity 8977 eV peak is observable up to 165 °C. As this feature vanishes, a small shoulder emerges below 8985 eV at the 180 °C XANES. This is explained by reduction of some Cu(II) to Cu(I). The intensity of this shoulder increases with rising temperature, evidencing a growing fraction of Cu(I) in the sample. Formation of metallic copper may as well be assumed from the shape of the 500 °C XANES. The profiles of this XANES and XANES of copper foil above 8985 eV (Figure 6.4 c)) are to a certain extent similar.

The Cu(I) pre-edge emerges at lower temperature in XANES of $Ag^{0.5}Cu^{0.5}$-Y than in XANES of Cu-Y. As mentioned earlier, XANES show that Cu(I) formation in Cu-Y starts after 190 °C. For $Ag^{0.5}Cu^{0.5}$-Y, XANES indicates formation of Cu(I) already at 165 °C. In addition, no evidence for metallic copper was found in XANES of Cu-Y. Thus, larger fraction of Cu(II) seems to be reduced in the silver containing sample. This is further examined in EXAFS and quantitative XANES analysis later (sections 6.4.4 and 6.5).

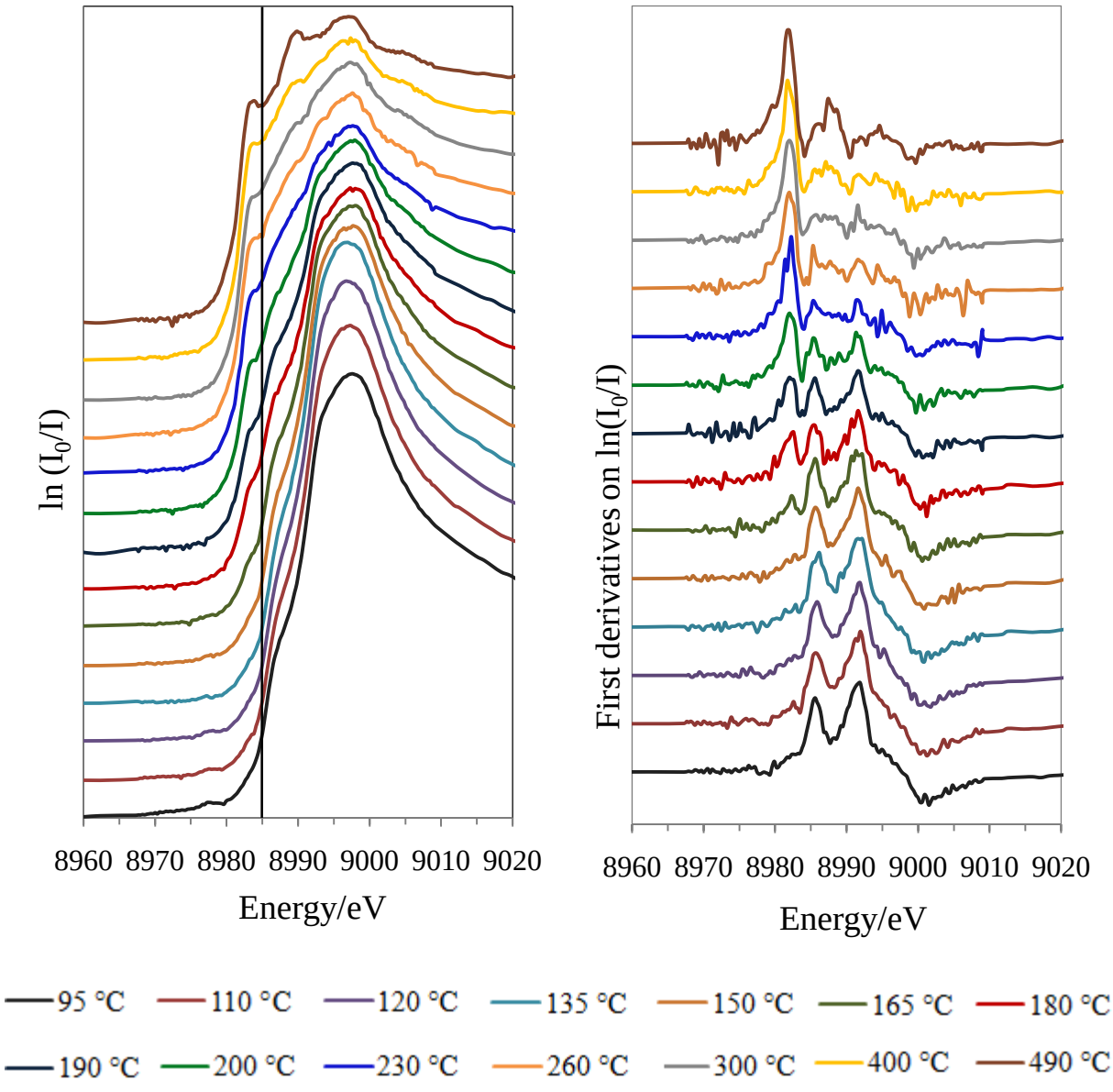

Figure 6.16 Normalized Cu-edge XANES and first derivatives of $Ag^{0.5}Cu^{0.5}$-Y during thermal treatment in hydrogen (95 – 490 °C).

The normalized XANES spectra from cooling in NO are shown in Figure 6.17. As the temperature decreases, emergence of several pre-edge features is noticeable on the absorption edge of all XANES. The shoulder at about 8983 eV in the final XANES (65 °C), even though very weak, can be explained by remaining copper(I), possibly copper(I) oxide. The feature above 8985 eV is probably due to formation of copper(II) oxide, as the XANES of 65 °C and its derivative match the ones of CuO (Figure 6.4 b)) to a certain degree. In the same spectrum the weak rise in absorption at 8977 eV, which vanished upon heating in hydrogen, reappears demonstrating re-oxidation of copper to the divalent state.

In contrast to XANES of $Ag^{0.5}Cu^{0.5}$-Y, no residual Cu(I) was observable at the final NO XANES of Cu-Y. Neither did the derivative of the latter resemble the one of CuO. This might point toward less formation of CuO in Cu-Y than in $Ag^{0.5}Cu^{0.5}$-Y during cooling in NO.

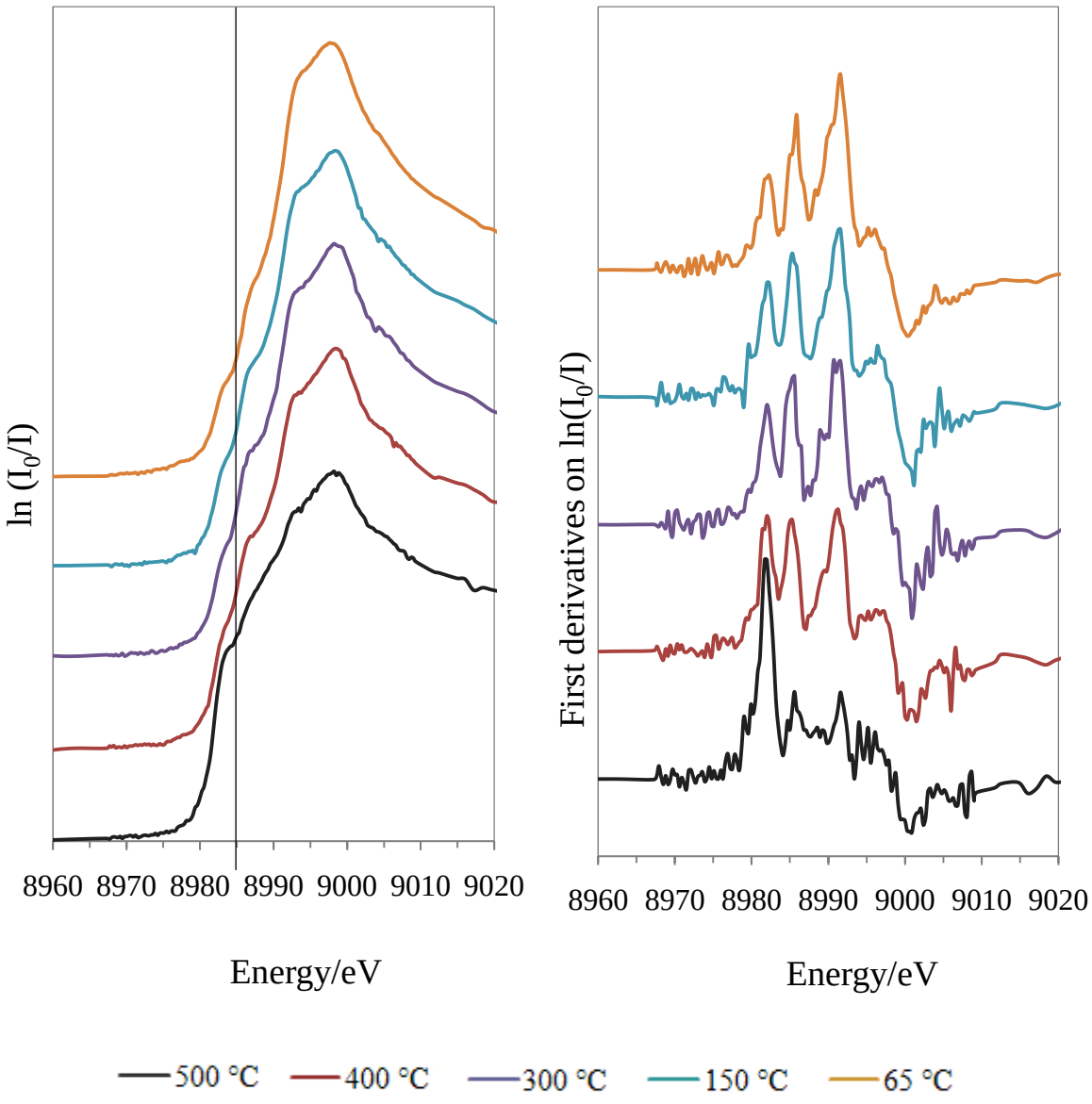

Figure 6.17 Normalized Cu-edge XANES and first derivatives of $Ag^{0.5}Cu^{0.5}$-Y during cooling in NO with (500 – 65 °C).

6.4.3 Quantitative analysis of XANES from in-situ measurements of Cu-Y

Hydrogen stage

The linear combination method seeks to reproduce the pre-edge XANES of the sample with XANES of reference compounds [9]. XANES from the hydrogen stage of Cu-Y were analyzed by the method to determine quantities of different copper species during reduction. Reference

compounds were chosen to be copper(II)–Tutton salt, diamminecopper(I) and copper foil. In addition, the XANES from helium at 20 °C was used, as it showed copper to be in the divalent state before treatment with hydrogen. Normalization range for all spectra was set to 30-150 eV in the relative energy scale. Results from the linear combinations for Cu-Y are displayed in Figure 6.18 a). XANES from the helium 20 °C is referred to as "original sample". The R-factor for each linear combination is given in Table 6.4.

The calculated fraction of Cu(I) at 150 °C is ~15%. From the corresponding XANES in Figure 6.13 there is not much evidence of Cu(I) at this relatively low temperature. A distinctive difference between 190 °C and 270 °C XANES of Cu-Y was observed in the qualitative analysis. The Cu(I) pre-edge at 8983 eV was absent in the former and present in the latter (Figure 6.13). Based on these XANES profiles, an abrupt increase in the Cu(I) fraction when going from 190 °C to 270 °C was expected from the linear combinations. However, linear combinations estimate a constant Cu(I) fraction up to 325 °C (~ 20%), reaching a maximum value of ~ 32% at 500 °C. However, the reliability of these estimates can be put in question, as the R-factors (Table 6.4) are very high.

Formation of metallic copper is estimated to start at 490 °C, with a maximum value of ~ 7% at 500 °C. Occurrence of metallic copper in Cu-Y was not obvious from the XANES of the hydrogen stage. But the estimated value is so small, and cannot be expected to be observable in the XANES.

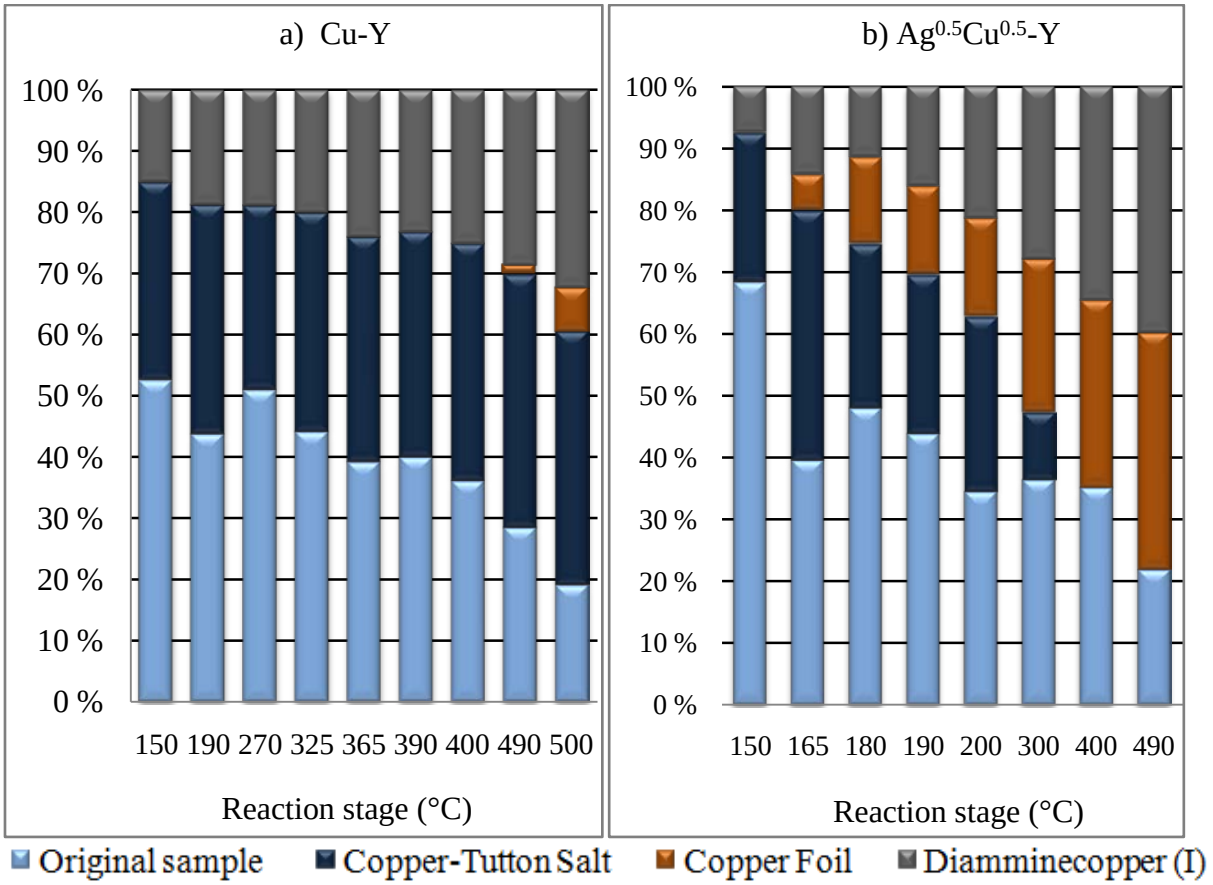

Figure 6.18 Results from linear combination of XANES from thermal treatment in hydrogen with reference compounds. a) Cu-Y and b) $Ag^{0.5}Cu^{0.5}$-Y.

Table 6.4 R-factors of the Linear Combinations to Reproduce XANES from the Hydrogen Stage of $Ag^{0.5}Cu^{0.5}$-Y and Cu-Y. The values are multiplied by 100.

Reaction stage (°C)	R-factor (Cu-Y)	R-factor ($Ag^{0.5}Cu^{0.5}$-Y)
150	0,0969	0,033
165		0,0962
180		0,1047
190	0,1382	0,0729
200		0,0447
270	0,1019	
300		0,0267
325	0,0996	
365	0,0737	
390	0,0802	
400	0,0711	0,0446
490	0,05	0,3252
500	0,0392	

NO stage

In linear combination fit of the XANES from the NO stage of Cu-Y, reference compounds used were copper(II) oxide, copper(I) oxide and copper foil. The XANES from helium at 20 °C of Cu-Y was also included to examine amount of re-oxidized copper. Results from the least-square minimization are shown in Figure 6.19 a). XANES from helium at 20 °C is referred to as “original sample”. The R-factor for each linear combination is given in Table 6.5.

The linear combination results are to a high degree in agreement with the corresponding XANES profiles in Figure 6.14. Presence of multiple valence states can be seen in the XANES of 500 °C, 400 °C and 300 °C. These observations are confirmed by the fitting method, yielding both copper(II) oxide and copper(I) oxide at 500 °C, 400 °C and 300 °C. It was also seen that the Cu(I) pre-edge at 8983 disappeared in the XANES of 65 °C and 20 °C. This is consistent with the results obtained with linear combination fitting, showing no copper(I) oxide at 65 °C and 20 °C. A noticeable outcome from the fitting of the 65 °C and 20 °C XANES is the growing fraction of the original sample at expense of copper(I) oxide. In the qualitative analysis it was noticed for the XANES of 20 °C in NO (and especially its derivative) to bear closer resemblance with the XANES of 20 °C in helium than that of CuO. This leads to a statement that a relatively large fraction of copper is reversed the divalent state.

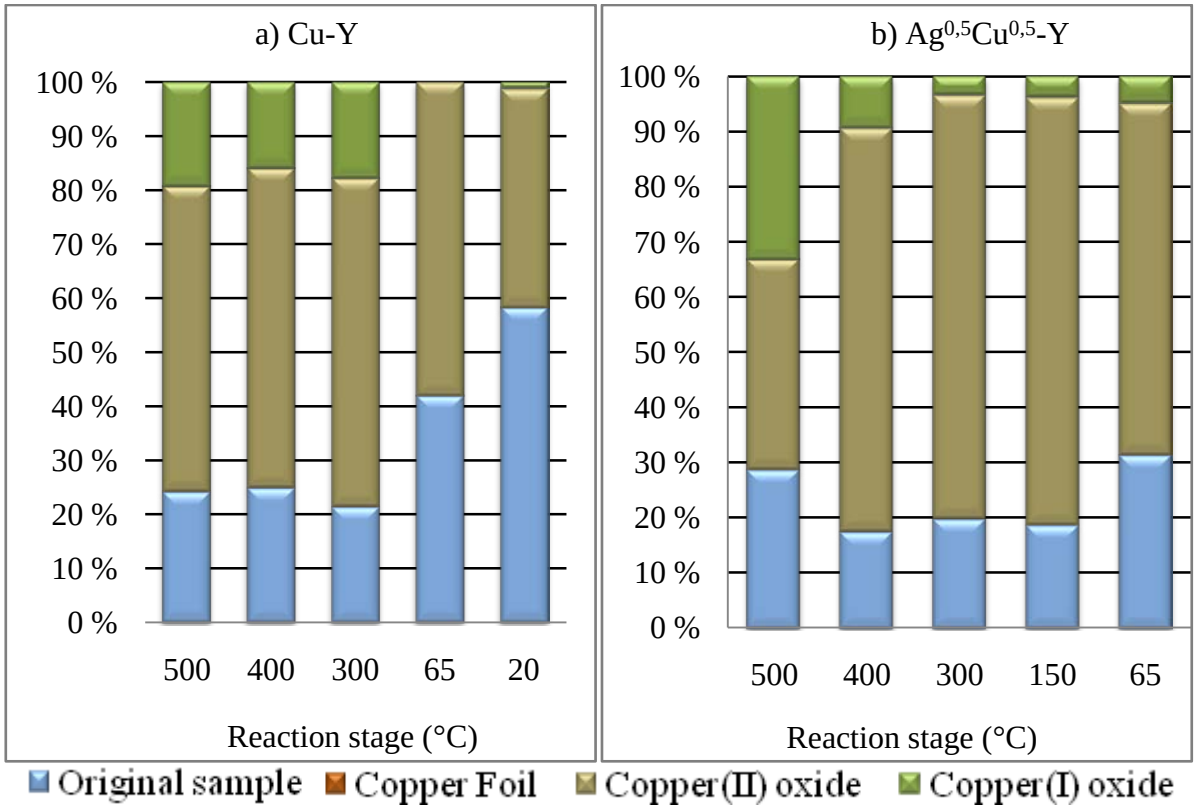

Figure 6.19 Results from linear combination of XANES from cooling in NO with reference compounds; a) Cu-Y and b) $Ag^{0.5}Cu^{0.5}$-Y.

Table 6.5 R-factors of the Linear Combinations to Reproduce XANES from the NO Stage of $Ag^{0.5}Cu^{0.5}$-Y and Cu-Y. The values are multiplied by 100.

Reaction stage (°C)	R-factor (Cu-Y)	R-factor ($Ag^{0.5}Cu^{0.5}$-Y)
500	0,0896	0,1122
400	0,0783	0,0446
300	0,0949	0,0818
150		0,091
65	0,0939	0,15
20	0,0377	

6.4.4 Quantitative analysis of the XANES from in-situ measurements of $Ag^{0.5}Cu^{0.5}$-Y

Hydrogen stage

Upon reproduction of each XANES spectrum from the hydrogen stage by linear combination, reference compounds used were copper(II)–Tutton salt, Cu metal and diamminecopper(I). As for the former linear combinations, the XANES of $Ag^{0.5}Cu^{0.5}$-Y from helium at 20 °C was also used in order to examine how much of the initial Cu(II) was reduced to Cu(I) and/or metallic copper. Results are shown in Figure 6.18 b).

The linear combination results show a trend in Cu(I) formation. The fraction of Cu(I) increases with increasing temperature. The value is estimated to ~15% Cu(I) at 150 °C. At the most, the linear combination fit yields a fraction of ~40% Cu(I) in $Ag^{0.5}Cu^{0.5}$-Y (at 500 °C). At the exact same stage for Cu-Y, the Cu(I) fraction was calculated to ~30%.

In the qualitative analysis it was observed a similarity between XANES of $Ag^{0.5}Cu^{0.5}$-Y at 500 °C and XANES of copper foil above 8985 eV (Figure 6.16 and 6.4 c). This is mirrored in the linear combinations, showing a remarkable growth of metallic copper fraction in the sample. As the temperature reaches 500 °C the calculations result in 38% metallic copper. According to the results from linear combinations, there is a significant difference between the $Ag^{0.5}Cu^{0.5}$-Y and Cu-Y samples when it comes to formation of metallic copper. For Cu-Y, formation of metallic copper is first observed at 490 °C, with a maximum value of ~ 7% at 500 °C. These results agree with the qualitative XANES analyses of the two samples during hydrogen treatment, where it was assumed for copper to be more reduced in the silver containing sample than in Cu-Y.

Minor contradictories between the qualitative and this quantitative analysis are found in the data of 180 - 200 °C of $Ag^{0.5}Cu^{0.5}$-Y. Looking at the linear combination fits in this temperature range in Figure 6.18 b), the dominating fraction is that of Cu(II). From the XANES of the same range in 6.13, it rather seems as Cu(I) species dominate due to disappearance of the weak Cu(II) peak at 8979 eV and the appearance of the Cu(I) peak at 8983 eV. However, the mathematical results are more trustworthy. It is unreasonable to expect large Cu(I) fractions at this relatively low temperature rang.

At 300 °C the linear combinations estimate the Cu(II) fraction to be under 50%, with Cu(I) and metallic copper starting to dominate. This change is most pronounced at 490 °C where the Cu(II) fraction is calculated to ~20%. The same is observed in XANES of this temperature range in Figure 6.16, with little support of Cu(II) present.

NO stage

The results from linear combination fit of CuO, Cu_2O, Cu metal and the 20 °C helium XANES to reproduce the XANES spectra from the NO stage of $Ag^{0.5}Cu^{0.5}$-Y, are shown in Figure 6.19 b). The 20 °C helium XANES is referred to as "original sample", and was included to examine fractions of reversed copper valence.

The results from linear combination fit at 500 °C are in agreement with the observations of the corresponding XANES in Figure 6.17. Both show occurrence of Cu(I) and Cu(II). Calculated fractions of copper(I) oxide and copper(II) oxide in the sample are ~0,33% and ~0,38%, respectively.

The linear combination fit of 400 °C XANES yields a large fraction of CuO (~70%), mainly at the expense of Cu(I). Validation of this result is found in the corresponding XANES in Figure 6.17, as a shoulder appears at the absorption edge petering out below 8985 eV. This is the same feature seen in CuO XANES (Figure 6.4 b)), confirming formation of CuO in $Ag^{0.5}Cu^{0.5}$-Y when cooled in NO.

Comparing the results of Cu-Y and $Ag^{0.5}Cu^{0.5}$-Y in figure 6.19 a) and b), it can be seen that formation of copper(II) oxide is greater than in the latter. This is in accordance with qualitative analysis. At the final temperatures in NO, XANES of Cu-Y did not exhibit the characteristic CuO pre-edge, in contrast to the XANES of $Ag^{0.5}Cu^{0.5}$-Y, as described in the section above.

6.4.5 Edge position versus oxidation state

The position of the Cu K absorption edge depends on the oxidation state of the element. Positive metal ions have a higher energy threshold than the corresponding neutral atom, since core electrons in the first are more tightly bound to the nucleus due to effective nuclear charge. In order to investigate how the position of the Cu K absorption edge varies during the in-situ measurements, the edge energy E_0 was determined in each spectrum recorded during heating of the sample in hydrogen and cooling in NO. This is illustrated in Figure 6.17 for both the Cu-Y and $Ag^{0.5}Cu^{0.5}$-Y sample.

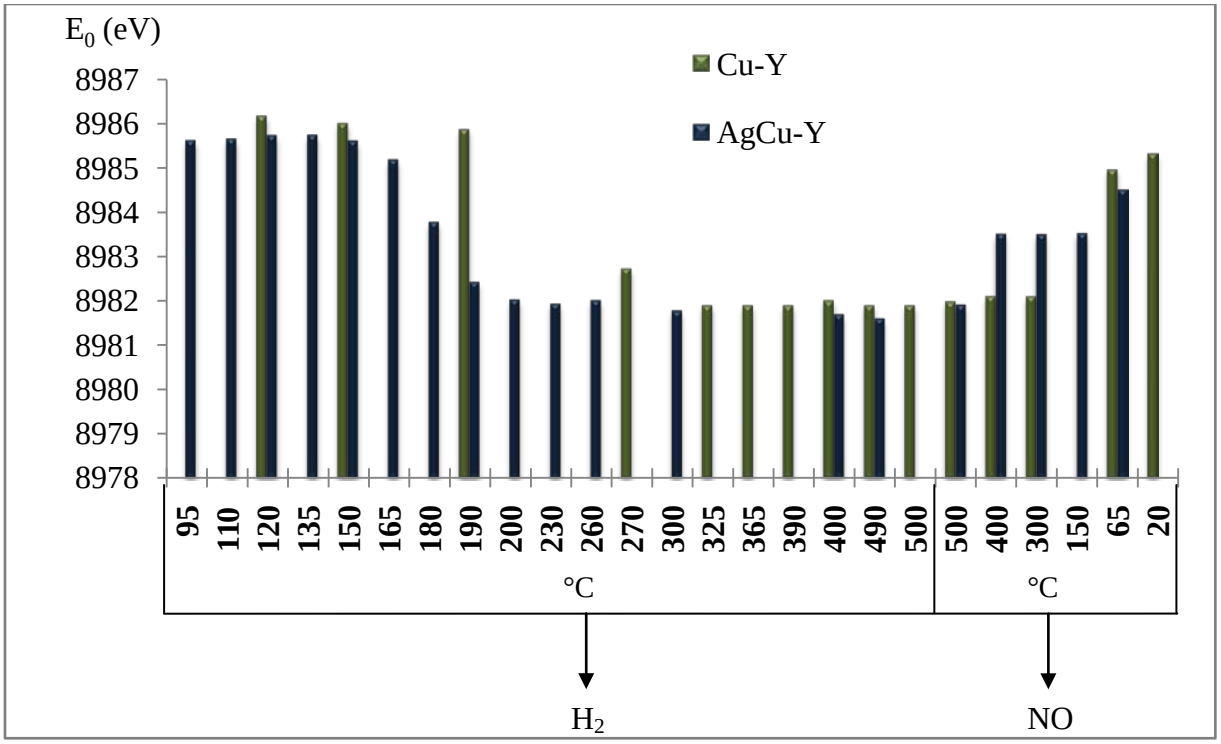

Figure 6.20 Variation in edge energy of copper in Cu-Y and $Ag^{0.5}Cu^{0.5}$-Y when heated in H_2 and cooled in NO.

The edge energy E_0 in each recorded spectrum was determined in ATHENA as the first peak of the first derivative of $\mu(E)$. As seen from the results of XANES analysis in sections above, some spectra were dominated by several pre-edge features due to presence of multiple valence states. In the derivatives of these spectra, the pre-edges might be mistaken as E_0. To avoid incorrect values, E_0 was set to the position of half the edge step height in the normalized $\mu(E)$. This procedure is illustrated in Figure 6.18.

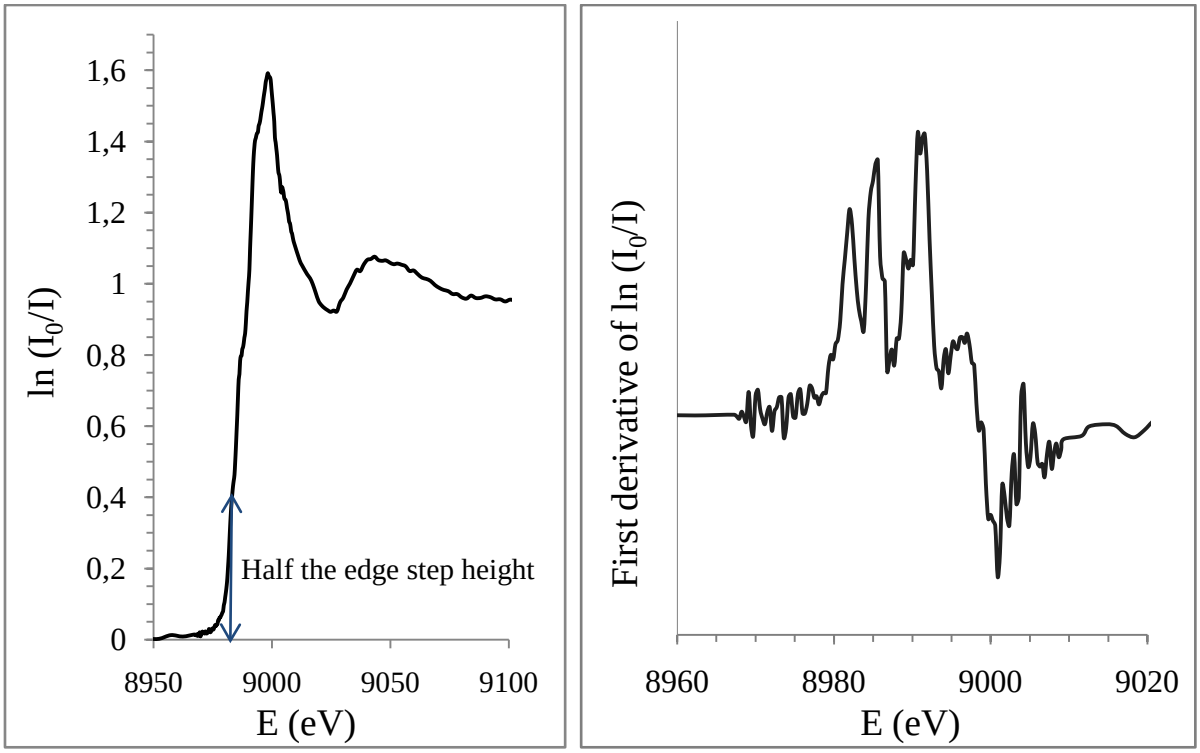

Figure 6.22 Determination of E_0 from half the edge step height (left) in normalized XANES. Determination from the derivative (left) may lead to erroneous E_0 values.

In the XANES analyses in previous sections, all results pointed towards higher reducibility of copper in $Ag^{0.5}Cu^{0.5}$-Y than in Cu-Y. Position of the edge energy confirms these observations. As seen in Figure 6.17, the edge energies are lower for the $Ag^{0.5}Cu^{0.5}$-Y sample than Cu-Y when thermally treated in hydrogen. At the final temperatures in NO, Cu-Y has higher edge energy values than $Ag^{0.5}Cu^{0.5}$-Y, indicating a larger fraction of reversed copper valence.

The largest difference occurs at 190 °C in hydrogen. Normalized XANES from 190 °C of these two samples are plotted in Figure 6.19. The pre-edge at 8983 eV in XANES of $Ag^{0.5}Cu^{0.5}$-Y is evidence of Cu(I) formation. In XANES of Cu-Y, this feature is absent. These observations imply that copper is more reduced in presence than absence of silver when thermally treated in hydrogen. On the hand, more copper is reversed in Cu-Y than in $Ag^{0.5}Cu^{0.5}$-Y when cooled in NO.

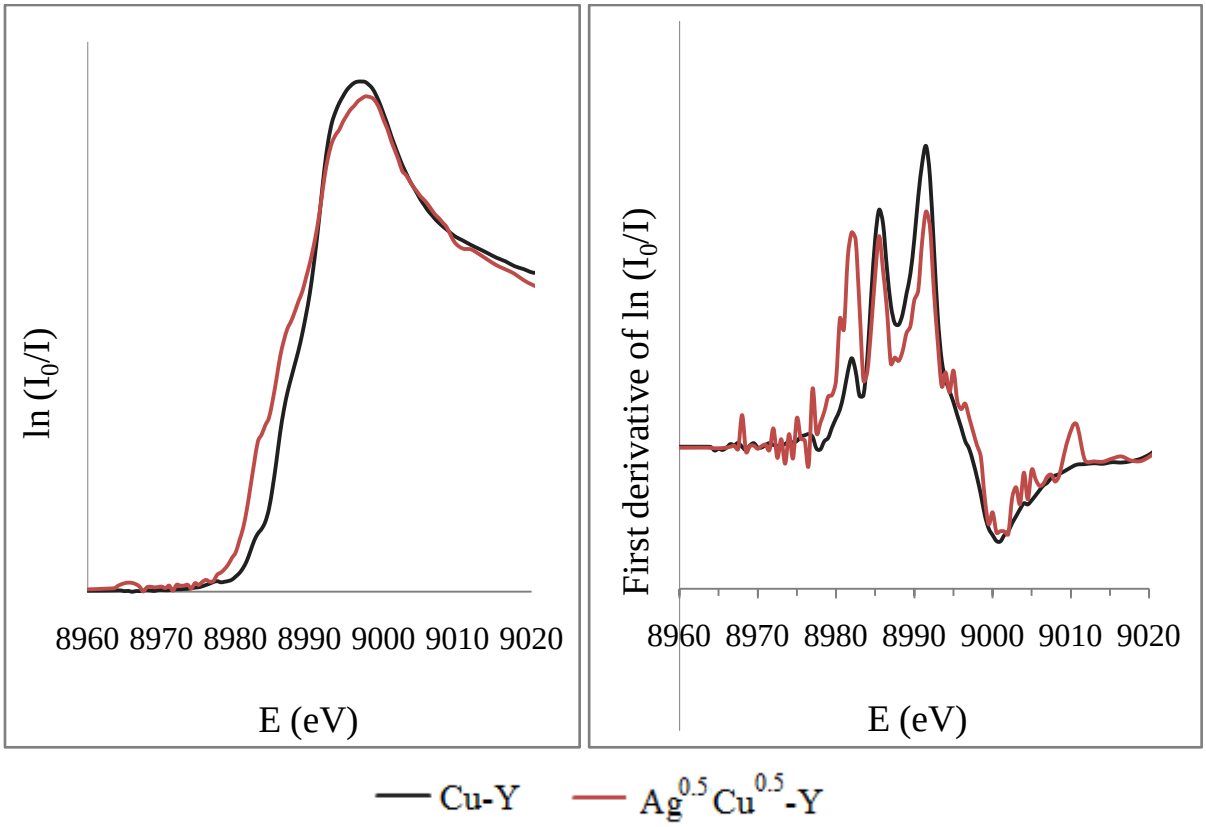

Figure 6.23 Normalized Cu-edge XANES and first derivatives of $Ag^{0.5}Cu^{0.5}$-Y and Cu-Y at 190 °C in hydrogen.

6.5 EXAFS of Cu-Y and $Ag^{0.5}Cu^{0.5}$-Y (In-situ)

6.5.1 Cu-Y

XAS data were collected at three different temperature steps in reducing environment to examine change in multiplicity and bondlengths of copper in Cu-Y. The steps are listed in Table 6.6 together with the corresponding figure number of the extracted k^3-weighted and least squares fitted EXAFS spectra with its Fourier transform.

Table 6.6 Overview of the temperature stages during thermal treatment in hydrogen at which EXAFS were recorded, with the corresponding figure number of the k^3-weighted and least squares fitted EXAFS spectra and its Fourier transform.

Reaction stage	k^3-weighted and least squares fitted EXAFS spectra with its Fourier transform
325 °C in hydrogen	Figure 6.24
400 °C in hydrogen	Figure 6.25
490 °C in hydrogen	Figure 6.26

Results from the least squares fitting are listed in Table 6.7. Recalling the results from room temperature EXAFS of Cu-Y (Section 6.3), the Cu–O bond distance was found to be 1.946(7) with a multiplicity of 2.8(2). Heating the sample in hydrogen leads to lengthening of the Cu–O bonds, from 1.967 (7) Å at 325 °C, to 1.983(8) Å at 490 °C. Multiplicity is 2.9(2) at the 325 °C stage and 2.3(2) at 490 °C. This small change in the immediate coordination about copper indicates that just a minor fraction of Cu(II) is reduced to Cu(I). The same observations were made in the XANES analyses of Cu-Y, where it was apparent that Cu(II) was dominant at 490 °C in hydrogen.

Table 6.7 Parameters from the Least Squares EXAFS analysis and Fractions of copper valences for Cu-Y at Different Temperature Stages upon Heating in Hydrogen [a,b]

Sample	Reaction stage *(Gas and T/ °C)*	Shell	N	r (Å)	$2\sigma^2$ (Å^2)	R (%)	Cu^0	Cu^I	Cu^{II}
CuY	H_2 (325)	Cu–O	2.9(2)	1.967 (7)	0.016(3)	27.16	-	0.35	0.65
		Cu···Cu	3(1)	2.99 (2)	0.04(1)				
	H_2 (400)	Cu–O	3(3)	1.958(7)	0.020(3)	28.89	-	0.22	0.78
		Cu···Cu	2(1)	2.97(1)	0.037(8)				
	H_2 (490)	Cu–O	2.3(2)	1.983(8)	0.019(3)	32.90	0.02	0.32	0.66
		Cu···Cu	2(1)	2.98(1)	0.03(1)				

a) k – range: 2 – 10 Å^{-1}. b) Standard deviation in the last significant digit as calculated by EXCURV 98 is given in parentheses.

A second peak is seen in the Fourier transform of EXAFS at 325 °C. It was fitted to 3(1) Cu···Cu distances at 2.99(2) Å. The same peak is present in Fourier transform of EXAFS at 400 °C and 490 °C. The Cu···Cu bond distance values are as in EXAFS of 325 °C. At all three stages, these multiplicities are low with high standard deviations. The Cu···Cu distances (2.98 Å) are not comparable to copper foil (2.55 Å). Therefore, it is doubtable that formation of metallic copper in Cu-Y occurs. These findings are consistent with the XANES analyses, where only small amounts of metallic copper were calculated for the XANES of 490 °C in hydrogen.

In addition to linear combination fitting, valence fractions for each reaction stage can also be calculated from the refined distances and multiplicities using Vegard relationship (Equation 6.1) [10];

$$R_{Cu(I)}\,x + R_{Cu(II)}\,(1 - x) = R_{EXAFS} \qquad (6.1)$$

Here, x is the fraction of copper(I), $R_{Cu(I)}$ is a Cu(I)–O of 2.0 Å derived by Mathisen et.al [11] in a fully reduced Cu:ZSM-5 sample. $R_{Cu(II)}$ is the distance of as-prepared sample (1.946 Å) and R_{EXAFS} is the refined Cu(I)–O value at each reaction stage.

In order to verify formation of metallic copper during whilst heating the Cu-Y sample in hydrogen, fractions are calculated in three steps [9]. First, the Cu(I) and Cu(II) fractions were calculated as described above. Second, the theoretical multiplicity (Equation 6.2) of the Cu–O shell was calculated using coordination number of 2 for Cu(I) (from the model) and coordination number of 3 (the refined value of Cu-Y as prepared);

$$2x + 3(1-x) = N_{Theory} \qquad (6.2)$$

Here, x and (1-x) are the values obtained from Equation 6.1.

Third, the theoretically expected multiplicity was compared to that of Cu–O extracted from the refinement for each reaction stage, since this multiplicity should decrease upon metallic copper formation;

$$(N_{Theory} / N_{EXAFS}) - 1 = y \qquad (6.3)$$

Thus, y gives the fraction of metallic copper. Fractions of Cu(I) and Cu(II) were then calculated from the remaining fraction, i.e. 1 – y using the values from Equation 6.1. Example of a calculation using Vegard relationship is given in Appendix A.

The copper valence fractions calculated with Vegard relationship for each reaction stage step is given in Table 6.7. The value of Cu(I) from the 325 °C stage (35 %) differs from the estimation of linear combination (20%). The value from the fitting method is more reliable for this stage, as Vegard relationship gives a lower fraction of Cu(I) at 400 °C. Decreasing Cu(I) fraction is not probable with increasing temperature. However, both methods give the same Cu(I) fractions for the 400 °C and 490 °C stages, with a maximum Cu(I) fraction of ~ 30 %.

Metallic copper fraction is calculated to 2 % by Vegard relation for the 490 °C stage. Linear combination estimates the fraction of metallic copper to ~ 7 % for the same stage. In either case, the values are relatively low.

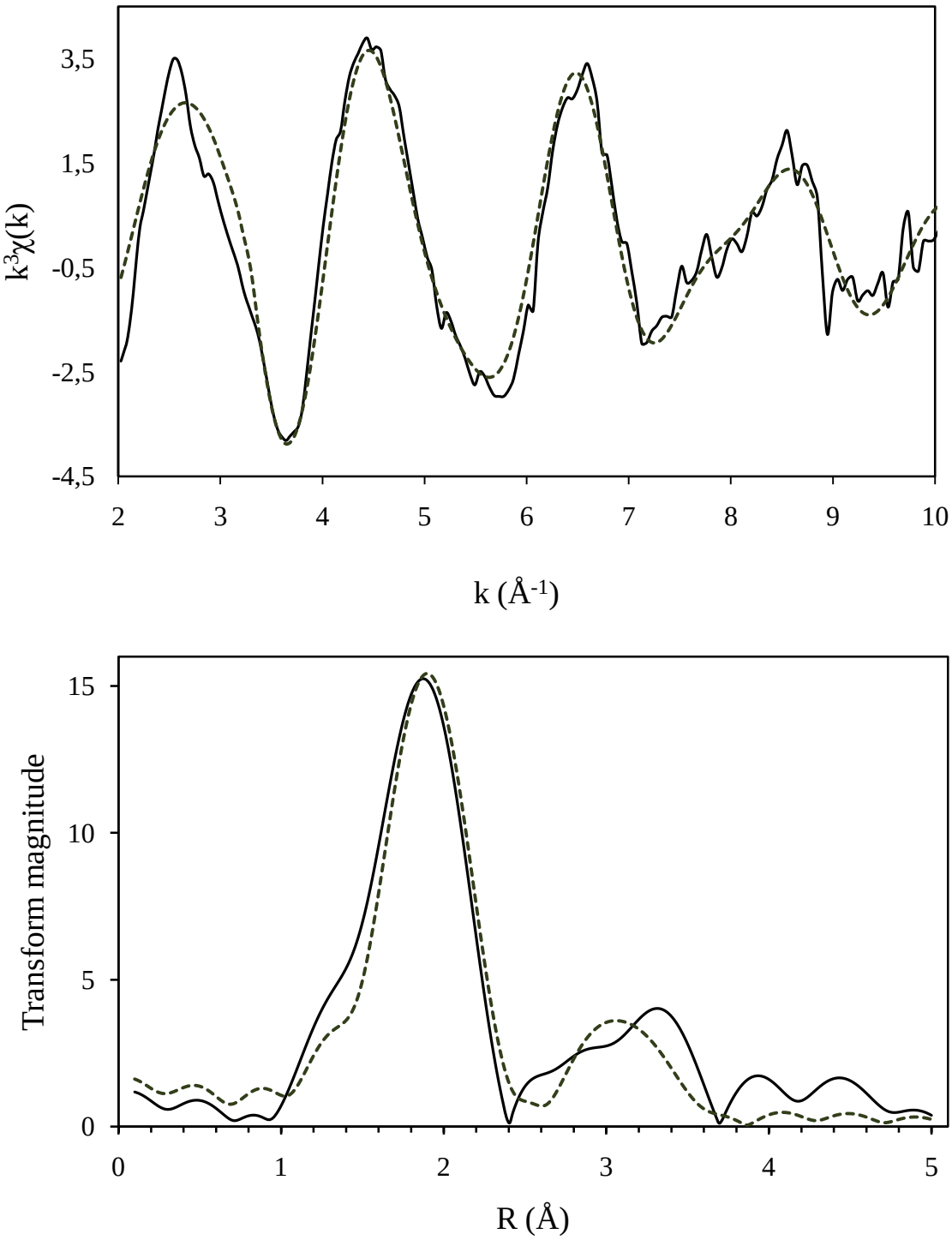

Figure 6.24 Experimental (—) and calculated (---) k^3-weighted EXAFS and its Fourier transform for Cu-Y in hydrogen at 325 °C.

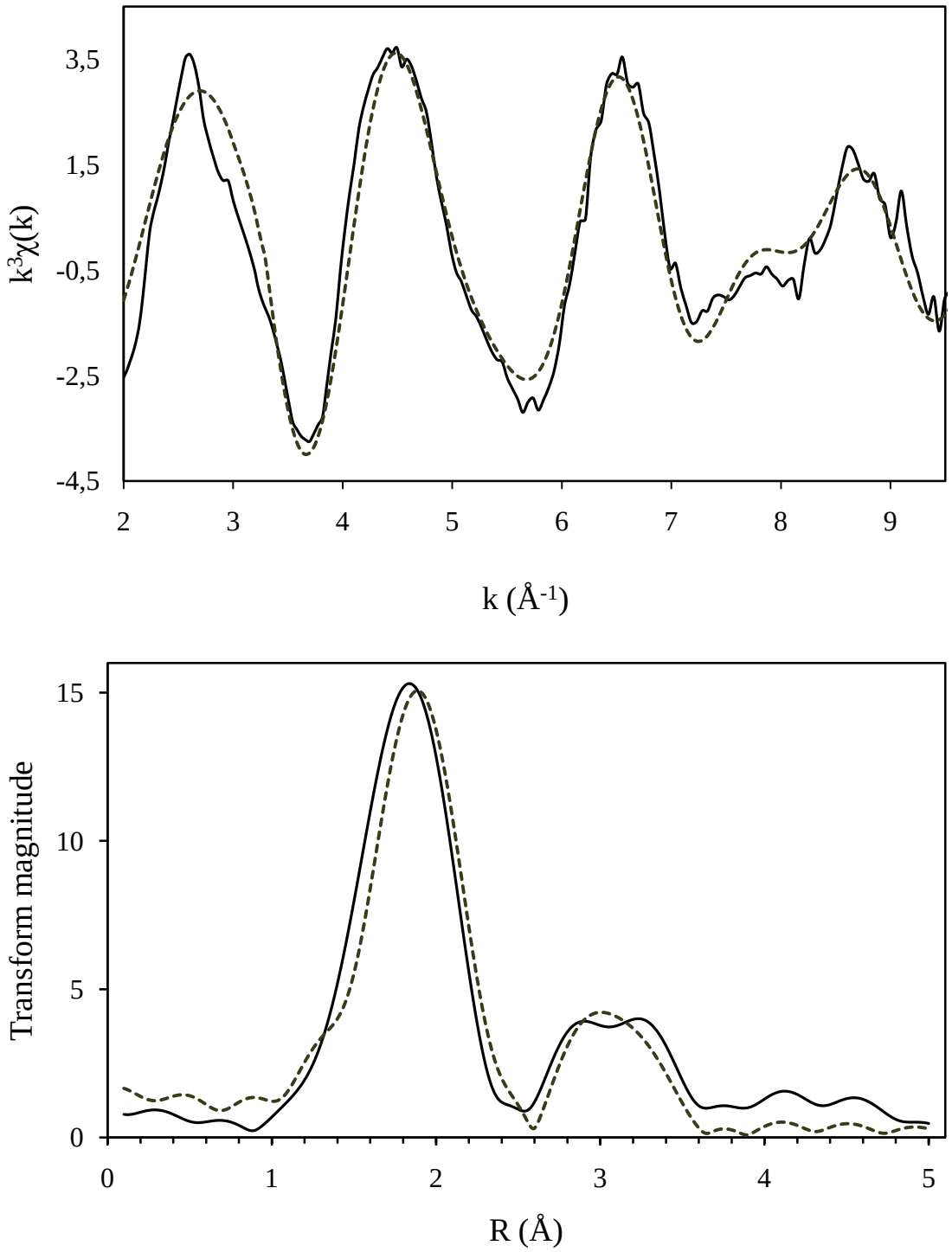

Figure 6.25 Experimental (—) and calculated (---) k^3-weighted EXAFS and its Fourier transform for Cu-Y in hydrogen at 400 °C.

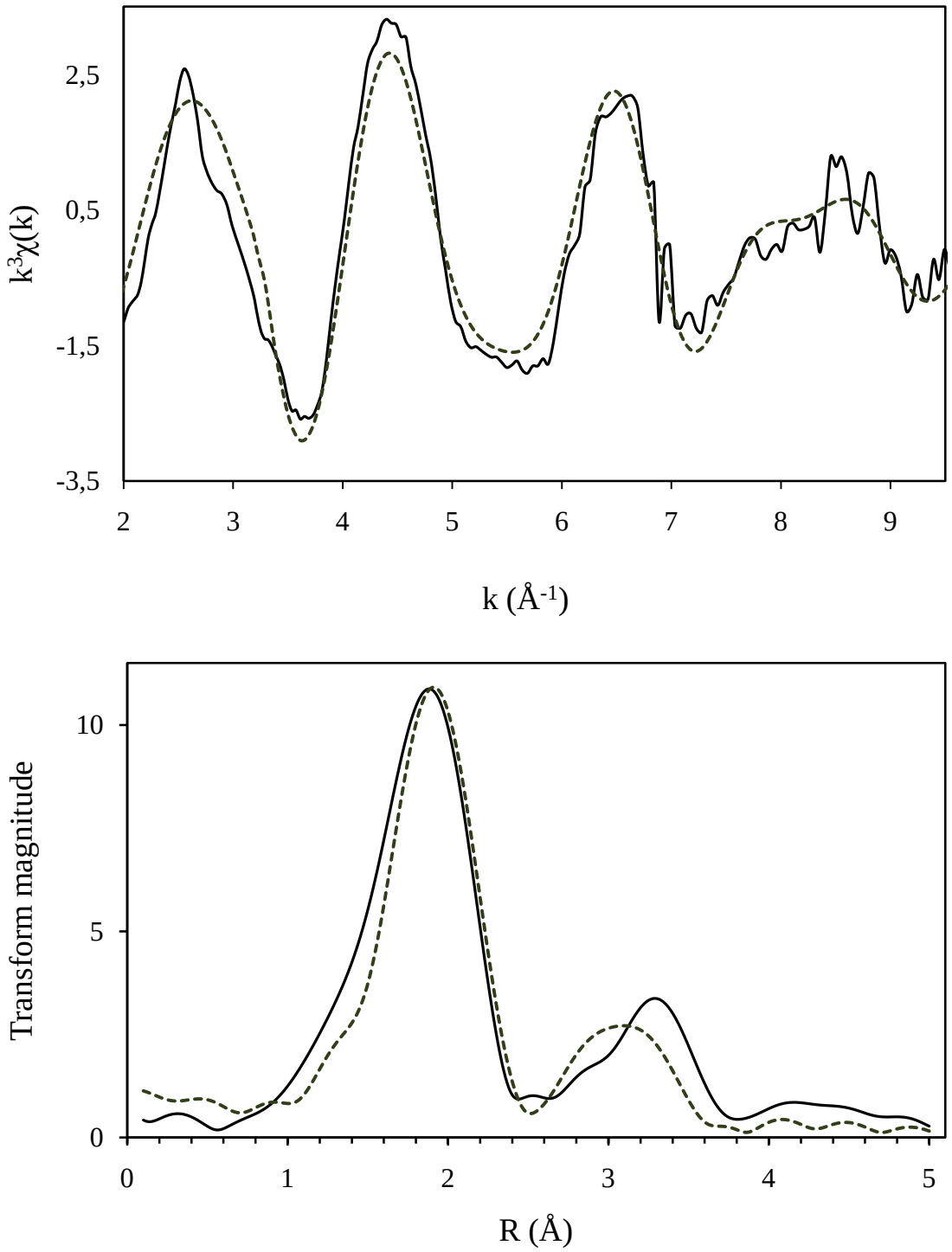

Figure 6.26 Experimental (—) and calculated (---) k^3-weighted EXAFS and its Fourier transform for Cu-Y in hydrogen at 490 °C.

6.5.2 $Ag^{0.5}Cu^{0.5}$-Y

XAS data were collected at three different temperature steps in reducing environment to examine change in multiplicity and bondlengths of copper in $Ag^{0.5}Cu^{0.5}$-Y. The steps are listed in Table 6.8 together with the corresponding figure number of the extracted k^3-weighted and least squares fitted EXAFS spectra with its Fourier transform.

Table 6.8 Overview of the temperature stages during thermal treatment in hydrogen at which EXAFS were recorded, with the corresponding figure number of the k^3-weighted and least squares fitted EXAFS spectra and its Fourier transform.

Reaction stage	(k^3-weighted and least squares fitted EXAFS spectra with its Fourier transform)
110 °C in hydrogen	Figure 6.23
200 °C in hydrogen	Figure 6.24
300 °C in hydrogen	Figure 6.25
400 °C in hydrogen	Figure 6.26
500 °C in hydrogen	Figure 6.27

Results from the least-square analyses are listed in Table 6.9, including interatomic distances, multiplicities and Debye–Waller factors ($2\sigma^2$). EXAFS of the as-prepared $Ag^{0.5}Cu^{0.5}$-Y showed 4.6(3) Cu–O distances at 1.948(5) Å. Treatment in hydrogen at increasing temperature causes lengthening of the Cu–O bond, accompanied by a decrease in multiplicity. In the final stage of the hydrogen treatment (500 °C), EXAFS shows 1.5(2) Cu–O distances of 1.993(9) Å. The change in the coordination of copper is significant, and can be ascribed to reduction of Cu(II) to Cu(I) and metallic copper. This is consistent with observations in XANES spectra and the linear combinations.

Table 6.9 Parameters from the Least Squares EXAFS analysis and Fractions of copper valences for $Ag^{0.5}Cu^{0.5}$-Y at Different Temperature Stages upon Heating in Hydrogen [a,b]

Sample	Reaction stage *Gas(T/°C)*	Shell	N	r (Å)	$2\sigma^2$ (Å^2)	R (%)	Cu^0	Cu^I	Cu^{II}
AgCuY	H_2 (110)	Cu–O	4.5(3)	1.955(6)	0.016(2)	20.72	0	0.13	0.87
	H_2 (200)	Cu–O	3.4(3)	1.965(9)	0.01(3)	31.08	0	0.33	0.67
		Cu⋯Cu	3(1)	2.98(2)	0.03(1)				
	H_2 (300)	Cu–O	3.0 (3)	1.979 (9)	0.026(4)	36.73	0	0.60	0.40
		Cu⋯Cu	3(1)	2.93 (2)	0.04(1)				
	H_2 (400)	Cu–O	2.4(2)	1.995(9)	0.023(4)	33.68	0.02	0.89	0.09
		Cu⋯Cu	5(1)	2.91(2)	0.05(1)				
	H_2 (500)	Cu–O	1.5(2)	1.993(9)	0.013(4)	42.89	0.57	0.37	0.6
		Cu⋯Cu	5(1)	2.89(2)	0.06(1)				

a) k – range: 2.3 – 10 Å^{-1}. b) Standard deviation in the last significant digit as calculated by EXCURV 98 is given in parentheses.

As for Cu-Y, valence fractions for each reaction stage of $Ag^{0.5}Cu^{0.5}$-Y were calculated from the refined distances and multiplicities using Vegard relationship (Equation 6.1). $R_{Cu(I)}$ was set to the Cu(I)–O distance of 2.0 Å derived by Mathisen et.al [11] in a fully reduced Cu:ZSM-5 sample. $R_{Cu(II)}$ is the distance of as-prepared $Ag^{0.5}Cu^{0.5}$-Y sample (1.948 Å) and R_{EXAFS} is the refined Cu(I)–O value at each reaction stage. The theoretical multiplicity (Equation 6.2) of the Cu–O shell was calculated using coordination number of 2 for Cu(I) (from the model) and coordination number of 4.6 (the refined value of $Ag^{0.5}Cu^{0.5}$-Y as prepared). Results from Vegard's method are listed in Table 6.9.

At each temperature stage, the calculated Cu(I) fractions are larger than in linear combinations. The values of 60 % and 89 % at 300 °C and 400 °C, respectively, are very high and doubtful. For these stages, reliability is put on the results from the fitting method (~ 30 % Cu(I)), as they are more reasonable. However, both methods show the same trend, where the fraction of Cu(I) gradually increases with increasing temperature.

Cu⋯Cu interactions are evident in the second peak in Fourier transform of EXAFS at the hydrogen stage at 200 °C (Figure 6.28). The corresponding bond length is of 2.98(2) Å with a

multiplicity of 3(1). During the course of hydrogen treatment with increasing temperature, the Cu···Cu distance stays unchanged, while the multiplicity reaches a value of 5(1) at 400 °C and 500 °C. Calculations by Vegard relationship result in a sudden increase of metallic copper at the final hydrogen stage, with a fraction of 57 %. In contrast, linear combinations show a gradually increasing fraction of metallic copper from 165 °C to 500 °C, reaching a maximum value of ~ 40 % (Figure 6.18 b)). Appearance of the second peak in Fourier transform of EXAFS already at 200 °C evidences formation of metallic copper below 500 °C. Hence, estimations from the fitting method are more reliable.

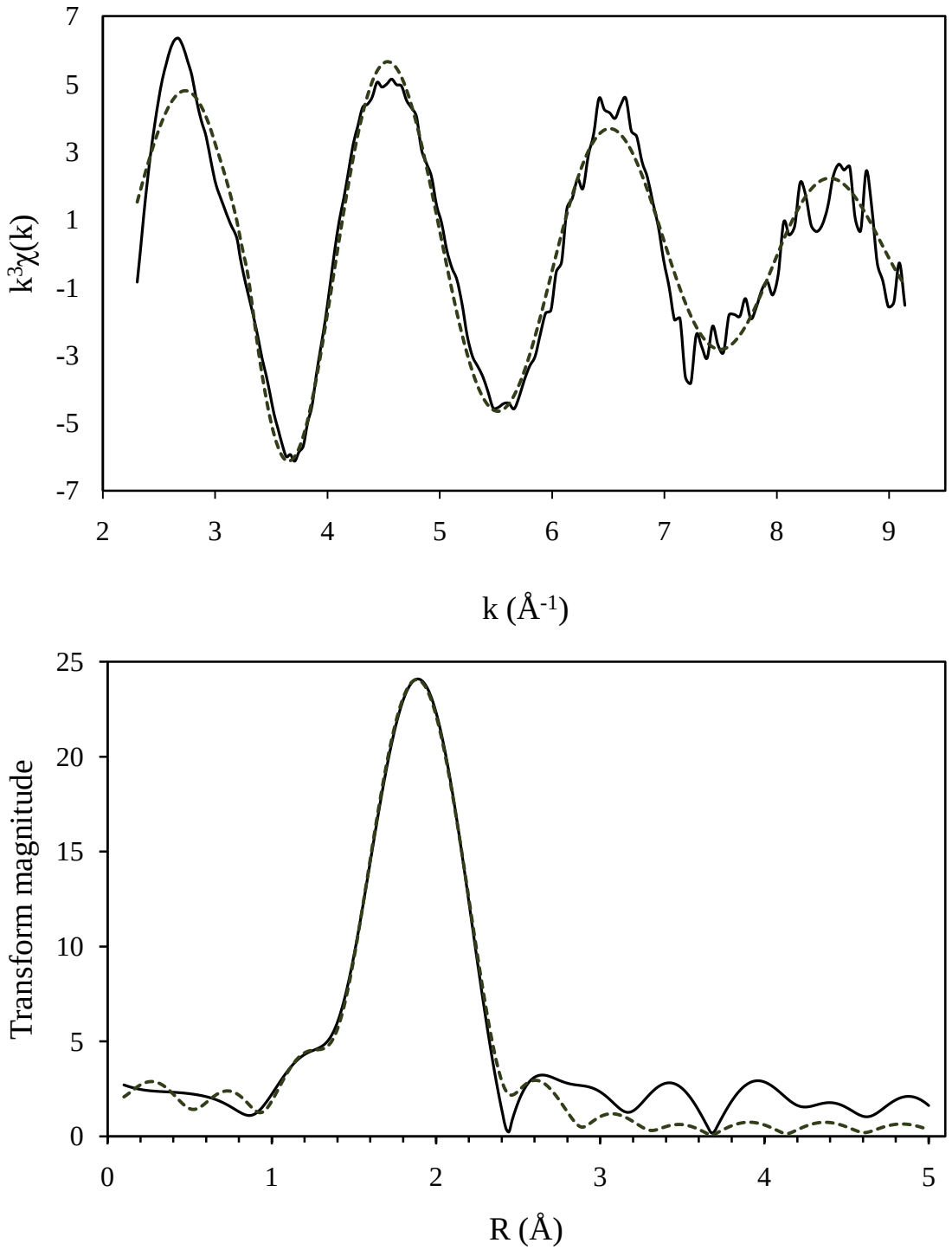

Figure 6.27 Experimental (—) and calculated (---) k^3-weighted EXAFS and its Fourier transform for $Ag^{0.5}Cu^{0.5}$-Y in hydrogen at 110 ℃.

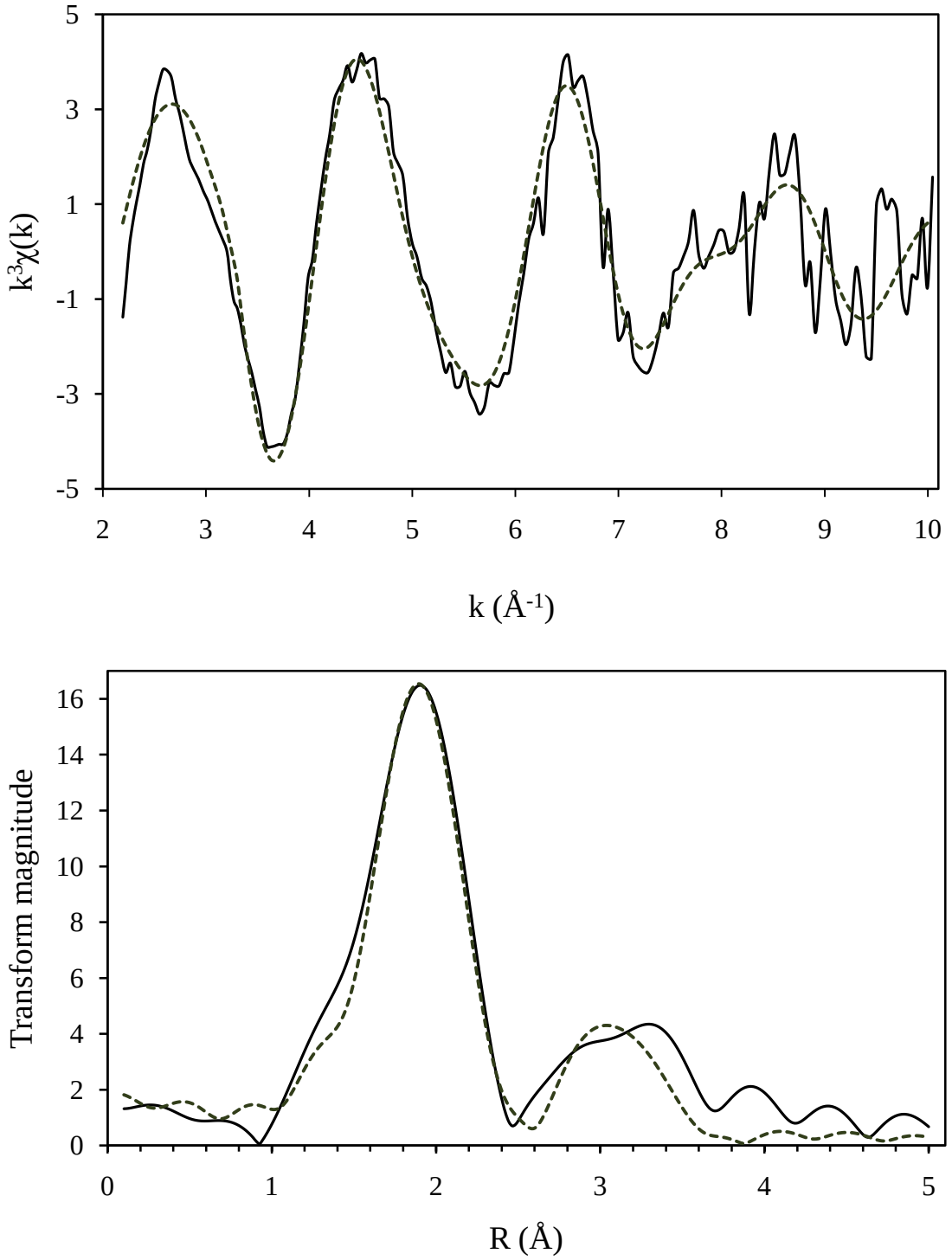

Figure 6.28 Experimental (—) and calculated (---) k^3-weighted EXAFS and its Fourier transform for $Ag^{0.5}Cu^{0.5}$-Y in hydrogen at 200 °C.

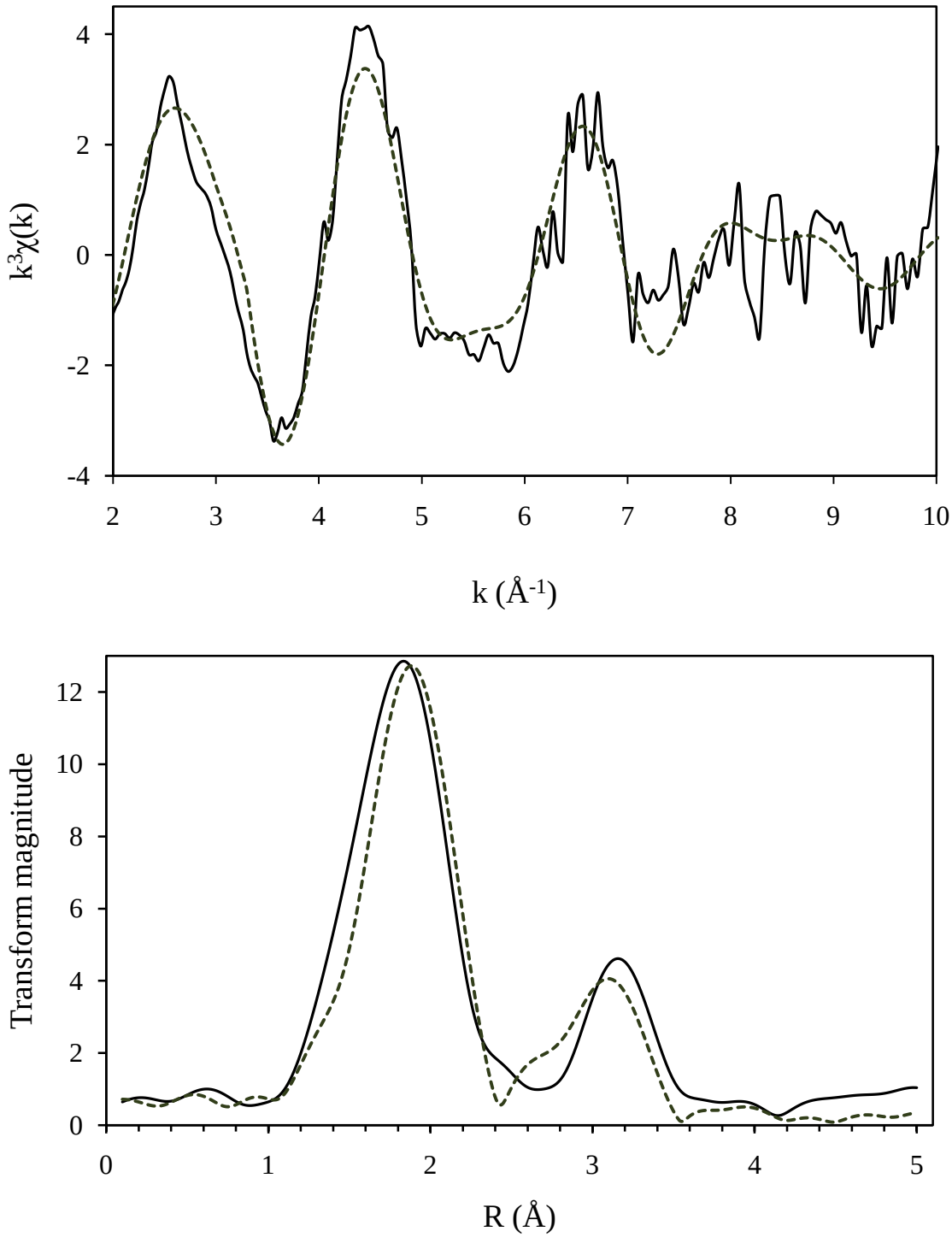

Figure 6.29 Experimental (—) and calculated (---) k^3-weighted EXAFS and its Fourier transform for $Ag^{0.5}Cu^{0.5}$-Y in hydrogen at 300 °C.

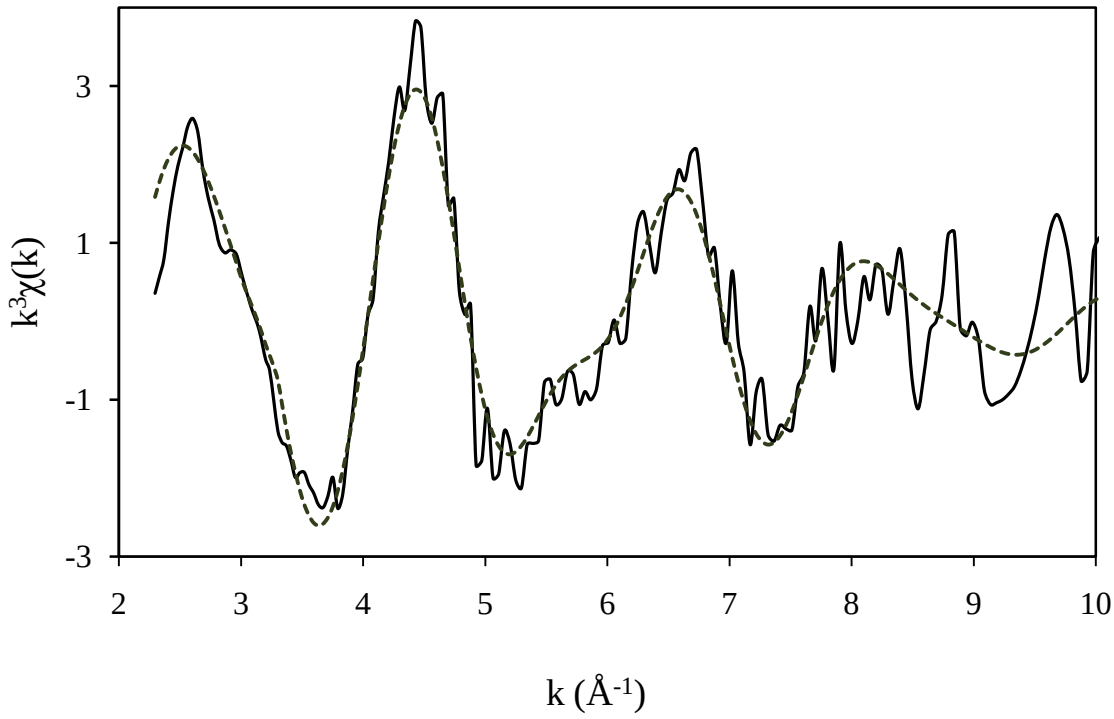

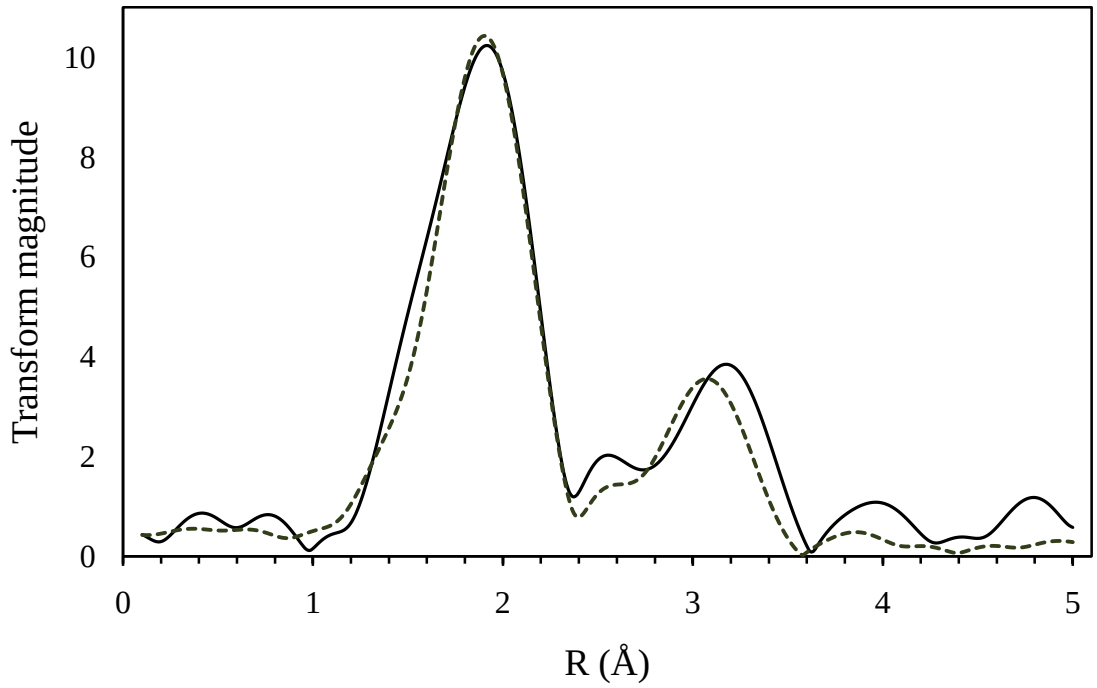

Figure 6.30 Experimental (—) and calculated (---) k^3-weighted EXAFS and its Fourier transform for $Ag^{0.5}Cu^{0.5}$-Y in hydrogen at 400 °C.

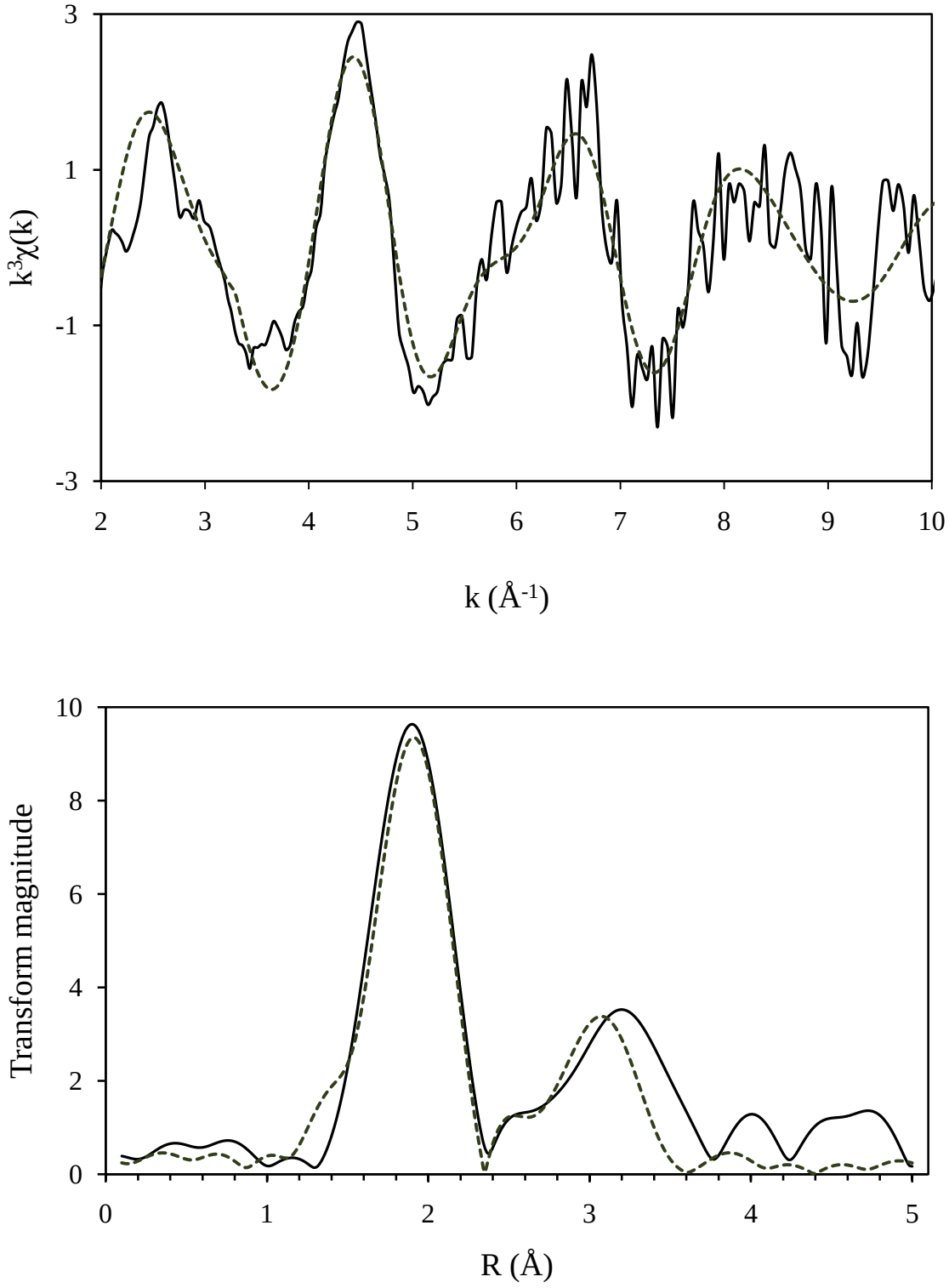

Figure 6.31 Experimental (—) and calculated (---) k^3-weighted EXAFS and its Fourier transform for $Ag^{0.5}Cu^{0.5}$-Y in hydrogen at 500 °C.

References

1. Karina Mathisen, *"Doctoral Thesis; X-ray absorption spectroscopic studies on active metal sites in zeotypes during the selective catalytic reduction of NO_x with propene in an oxygen rich atmosphere"*, NTNU, Trondheim, June 2005, Chapter 2

2. L. S. Kau, D.J. Spira-Solomon, J.E. Penner-Hahn, K.O. Hodgson and E.I. Solomon, *J. Am. Chem. Soc.* 1987, **109**, 6433–6442

3. C. Lamberti, G. Spoto, D. Scarano, C. Paze, M.Salvalaggio, S. Bordiga, A. Zecchina, G. Turnes Palomino, F. D'Acapito, *Chem. Phys. Letters*, 1997, **269**, 500-508

4. K. Mathisen, D. Nicholson, A.N. Fitch and M. Stockenhuber, *J. Mater. Chem.*, 2005, **15**, 204–217

5. G. Lamble, A. Moen and D.G. Nicholson, *J. Chem. Soc. Faraday Trans.*, 1994, **90**, 2211-221

6. S. Åsbrink and L.-J. Norrby, *Acta Cryst.*, 1970, B **26**, 8-15

7. S G. T. Palomino, S. Bordiga, and A. Zecchina, G. L. Marra, C. Lamberti, *J. Phys. Chem. B*, 2000, **104**, 8641-8651

8. H. Yahiro and M. Iwamoto, Applied Catalysis A: General, 2001, **222**, 163-181

9. K. Mathisen, M. Stockenhuber, D.G. Nicholson, Phys. Chem. Chem. Phys., 2009 (DOI: 10.1039/b902491c)

10. P.A. Barret, G. Sankar, C.R.A. Catlow and J.M. Thomas, *J. Phys. Chem.*, 1996, **100** (21), 8977-8985

11. K. Mathisen, D. Nicholson, A.M. Beale, M. Sanchez-Sanchez, G. Sankar, W. Bras and S. Nikitenko, *J. Phys. Chem*. C, 2007, **111**, 3130-3138

7 RESULTS FROM XRD AND SEM

Experimental details about data collection by X-ray Powder Diffraction and Scanning Electron Microscopy are given in section 7.1. Results from XRD are presented in section 7.2 and from SEM in section 7.3.

7.1 Experimental section

7.1.1 X-ray Powder Diffraction

X-ray Powder Diffraction analyses were performed using a Bruker-AXD D8-focus with CuKα radiation. Spectra were collected in the 2θ-range of 5-50° with a step size of 0.0164° and counting time of 11 seconds per step.

7.1.2 Scanning Electron Microscopy

Scanning electron micrographs were collected on a Zeiss Ultra FEG scanning electron microscope with Zeiss in-lens detector. The samples were dispersed on a double-side carbon tape attached to a sample holder.

7.2 XRD Results

X-ray powder diffractograms were collected for the as-prepared and calcined $Ag^{0.5}Cu^{0.5}$-Y sample, before and after the sample had been through in-situ measurements with gas and thermal treatments. In Figure 7.3 they are denoted as "$Ag^{0.5}Cu^{0.5}$-Y prior reaction" and "$Ag^{0.5}Cu^{0.5}$-Y post reaction".

The as-synthesized sample was exposed to a maximum temperature of 550 °C when calcined. During the in-situ measurements, the maximum temperature was 500 °C, meaning that the crystallinity of the sample only could be affected by the gas treatments. As seen from Figure 7.3 the diffraction patterns are very much alike. Thus, zeolite Y tolerates the gas and thermal treatments it was exposed to during in-situ, without collapse of the structure. Amounts of copper and silver are too small to be detected by XRD.

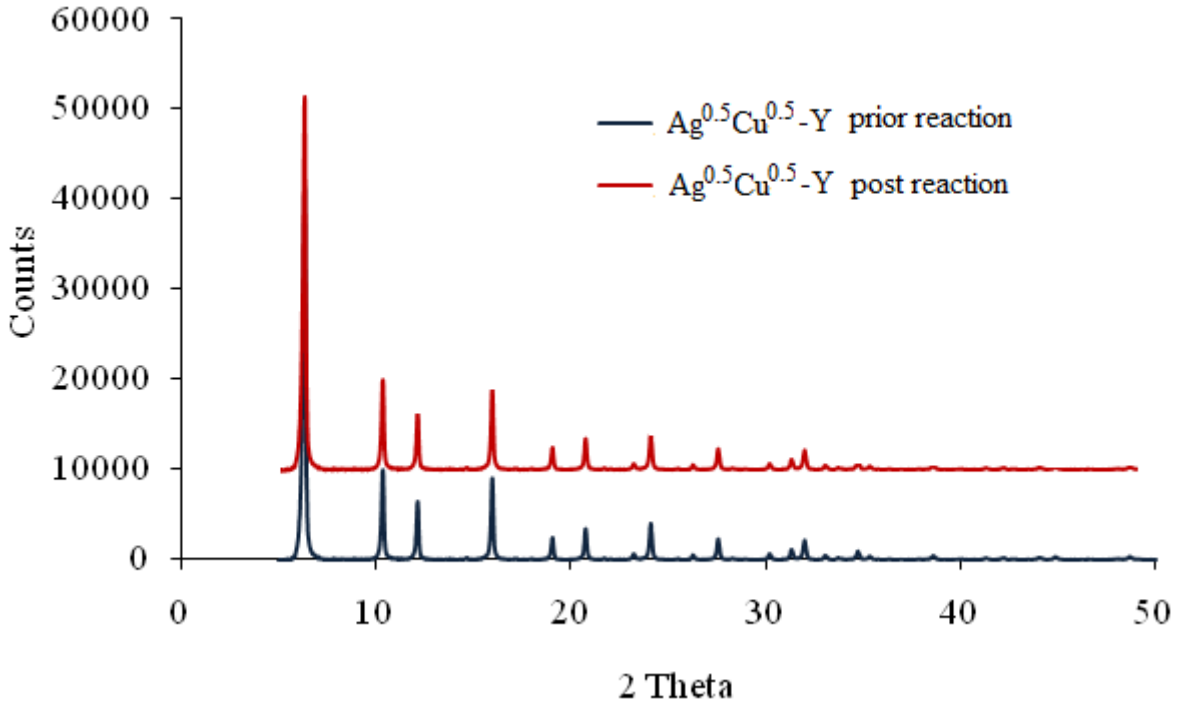

Figure 7.3 X-ray powder diffractograms of $Ag^{0.5}Cu^{0.5}$-Y prior to and post in-situ measurements.

7.3 SEM Results

Scanning electron micrographs of zeolite H-Y, Cu-Y as-prepared, $Ag^{0.5}Cu^{0.5}$-Y as-prepared and $Ag^{0.5}Cu^{0.5}$-Y after the in-situ measurements are shown in Figure 7.4. The images reveal the characteristic triangular pyramid morphology of zeolite Y [1] and a particle size in the range of 0.2-0.5 µm in all samples. Both the shapes and the size of the particles seem to be unchanged when zeolite H-Y is ion-exchanged and put through thermal and gas treatments. Some white particles of irregular shape can be seen in the micrograph of $Ag^{0.5}Cu^{0.5}$-Y after the in-situ measurements (Figure 7.4 d)). These are probably quarts wool residues, as quarts wool was used in the sample container of the in-situ cell (see section 6.11).

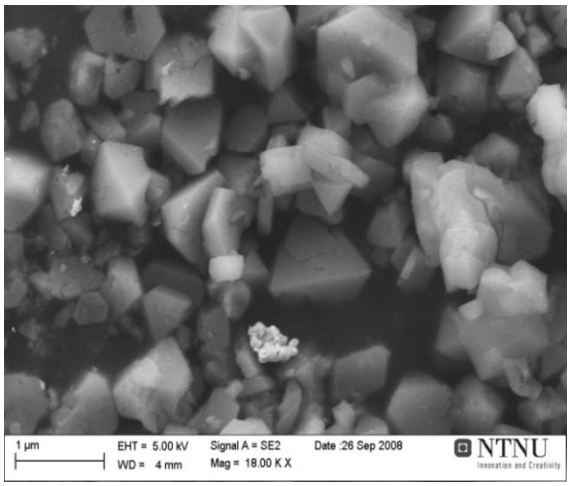

a) Zeolite H-Y

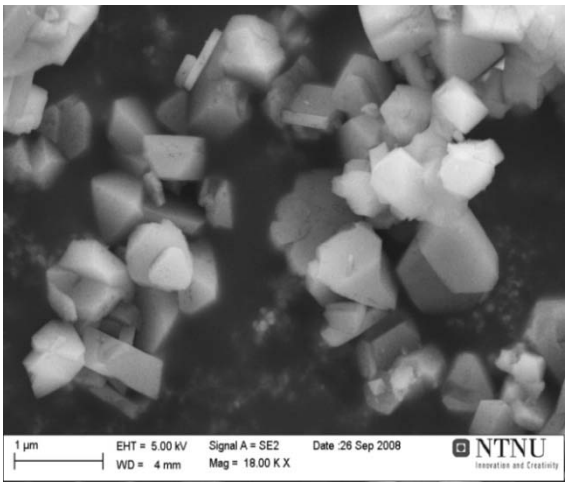

b) Cu-Y as-prepared

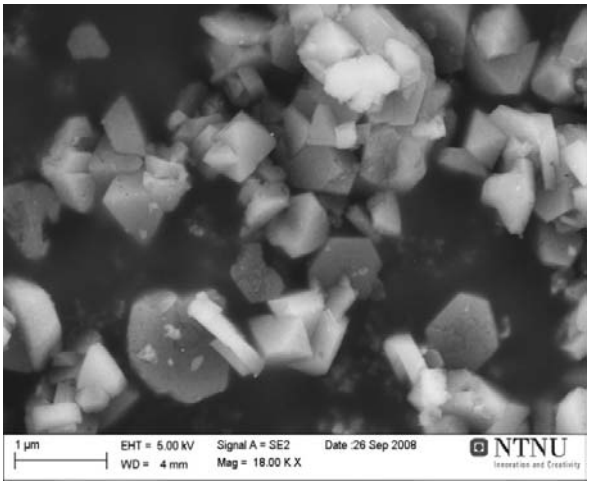

c) $Ag^{0.5}Cu^{0.5}$-Y as-prepared

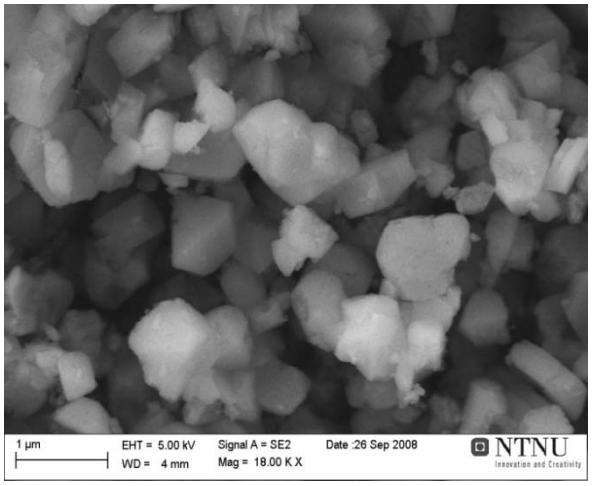

d) $Ag^{0.5}Cu^{0.5}$-Y post in-situ measurements

Figure 7.4 Scanning electron micrographs of a) Zeolite H-Y, b) Cu-Y as-prepared, c) $Ag^{0.5}Cu^{0.5}$-Y as-prepared and d) $Ag^{0.5}Cu^{0.5}$-Y post in-situ measurements.

References

1. T. Kuzniatsova, Y. Kim, K. Shqau, P. K. Dutta, H. Verweij, *Microporous and Mesoporous Materials*, 2007, **103**, 102–107

8 NO_X CONVERSION

Experimental details about the NOx measurements are given in section 8.1. Results are presented in section 8.2.

8.1 Experimental section

The experimental rig used for conversion measurements was located at Department of Chemical Engineering, University of Newcastle, Australia. A schematic illustration of the set-up is shown in Figure 7.1. The continuous flow microreactor is placed inside a furnace, with connection to four flow meters for controlled mixing of the feed gases. The gas flow can be directed through a by-pass line for measurement of NO concentrations before passing through the reactor.

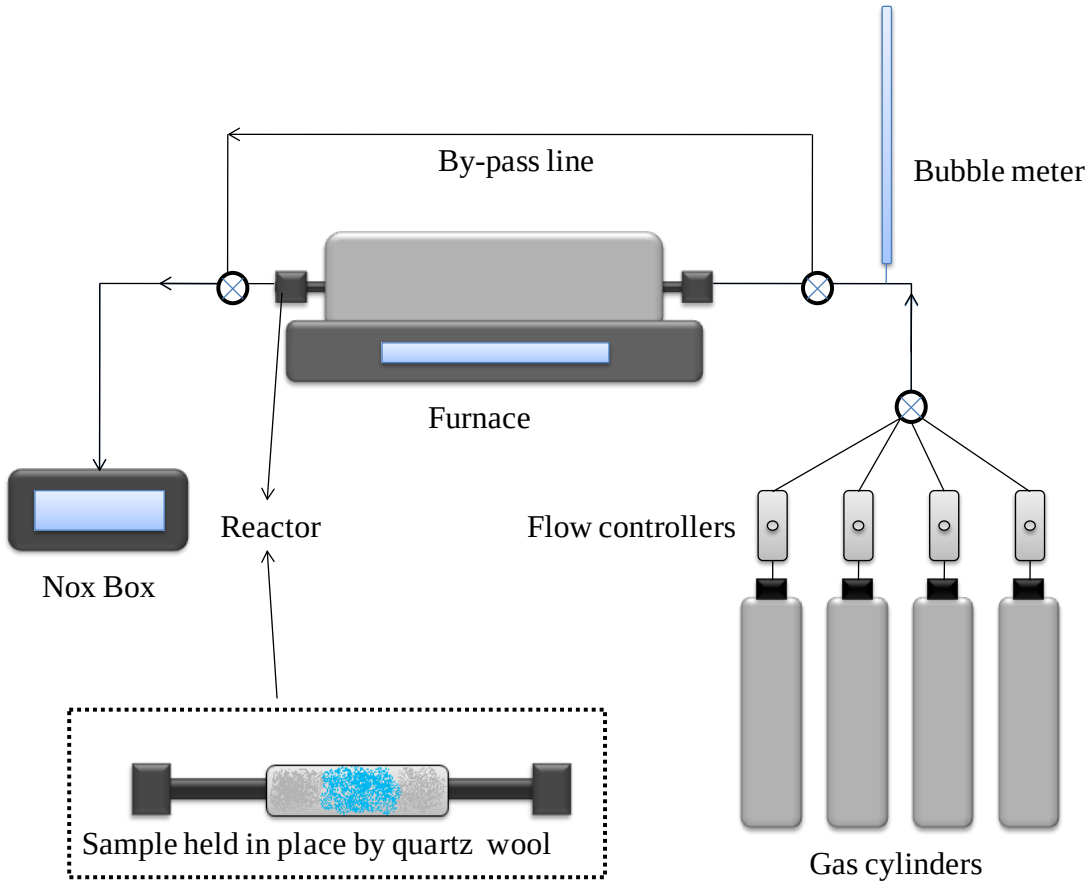

Figure 7.1 Schematic set-up for measurement of NO_x conversion

The powdered catalysts (0.28 g) were mortared, pressed to pellets and meshed to particle size range of 325-400 µm, before placed into the glass-lined stainless steel reactor. Quartz wool on each side of the catalyst particles ensured that the whole diameter of the reactor was filled. Both catalysts were degassed in helium flow (15 ml/min), by heating to 120 °C with a ramp rate of 5 °C/min, followed by heating to 500 °C with a ramp rate of 10 °C/min and finally cooling to 250 °C. The gas flow rate was adjusted using a simple bobble meter attached to the feed-gas line, and a stop watch.

Conversion of NO was measured over a temperature range of 250 – 500 °C, with 50 °C intervals. The feed gas consisted of 2000 ppm NO, 20 000 ppm O_2 and 1200 ppm propane, with a helium balance to give a total flow of 300 ml/min. At each temperature stage, the feed gas was allowed to flow for 30 minutes through the reactor, before the values from the NO_x box were read. The NO_x box was a Signal Instruments Model 4000. Ideally, a chromatograph should be stationed between the output from the detector and NO_x box. In this way, product gases from the reactor could be identified, in addition to the NO concentration before and after passing through reactor. However, a chromatograph was not available at the time measurements were performed.

The NO_x box detects the NO concentration automatically. NO conversion was calculated by Equation 6.4[1];

$$\text{NO conversion (\%)} = \frac{[\text{NO}]_{\text{By-pass}} - [\text{NO}]_{\text{Reactor}}}{[\text{NO}]_{\text{By-pass}}} \cdot 100 \qquad (7.1)$$

Here, $[NO]_{By\text{-}pass}$ is the NO concentration before passing through the rector and $[NO]_{Reactor}$ is the NO concentration after passing through the reactor. NO_x measurements were also performed on empty reactor, and the obtained values were subtracted from the values of the samples to correct the measurements.

8.2 Results from deNOx measurements

Obtained conversion of NO by Cu-Y and $Ag^{0.5}Cu^{0.5}$-Y are shown in Figure 7.2. There is no significant difference for the two samples, both giving a low conversion of ~ 4%. Thus, the co-cation effect does not improve the activity towards reducing NO. A possible explanation for the lacking of activity is poisoning of the catalyst. The as-prepared Cu-Y and $Ag^{0.5}Cu^{0.5}$-Y samples were light blue. After the thermal treatment and reaction with the feed gases upon NO_x measurements, both samples changed colour to black. This may indicate that the catalysts have been deactivated by carbonaceous deposits on the internal surface.

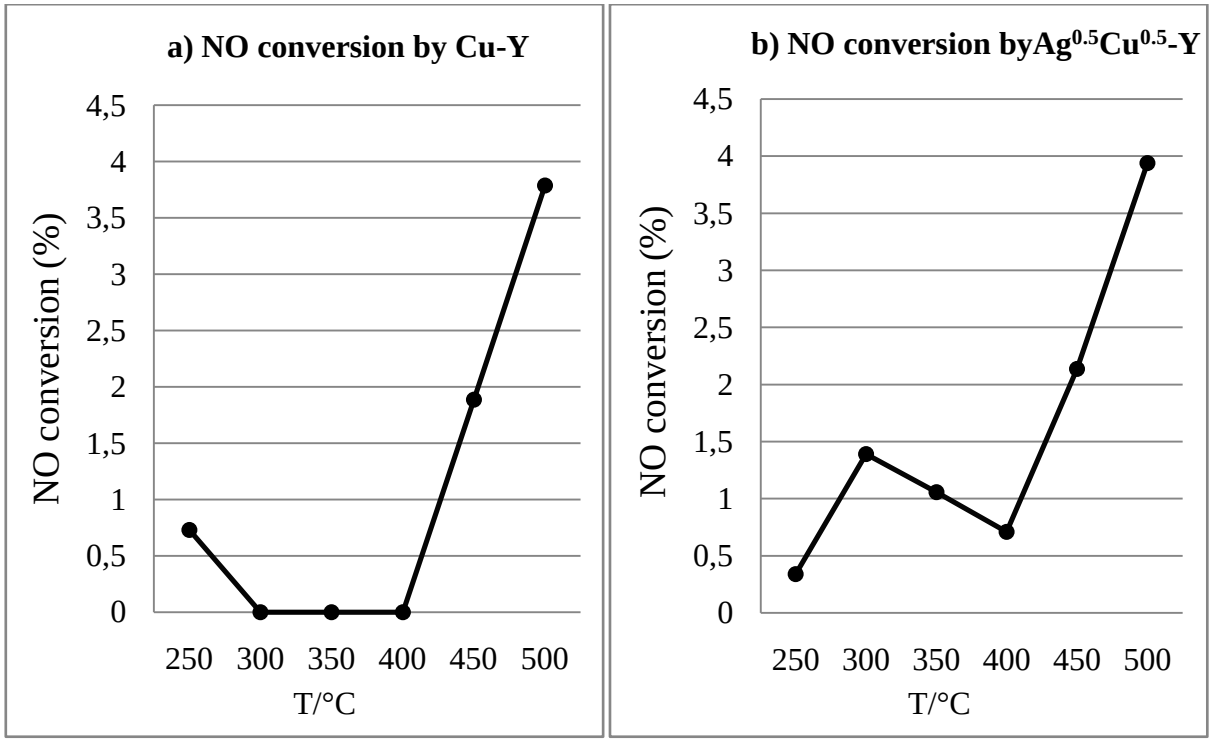

Figure 7.2 Conversion of NO over a) Cu-Y and b) $Ag^{0.5}Cu^{0.5}$-Y

References

1. Karina Mathisen, "*Doctoral Thesis; X-ray absorption spectroscopic studies on active metal sites in zeotypes during the selective catalytic reduction of NO_x with propene in an oxygen rich atmosphere"*, NTNU, Trondheim, June 2005, Chapter 2

9 DISCUSSION

9.1 ICP-MS results

The ratio of silver(I) nitrate/copper(II) nitrate solutions differs from the resulting silver/copper weight percentage in ion-exchanged zeolite Y. Each Al(III) in the silicate framework of the zeolite leads to one excess negative charge. Upon ion-exchange silver and copper are charge compensating ions. According to Equation 1-1, the univalent extra-framework silver ion is situated at one framework aluminum atom and the divalent extra-framework copper ion is preferentially located at two framework aluminum atoms. Thus, a larger fraction of silver than copper is expected after ion-exchange of the zeolite. However, the element analyses show that it is necessary to use solutions of silver(I) nitrate and copper(II) nitrate with equal concentrations in a ratio 4:1 to obtain approximately equal weight percentages of silver and copper in zeolite Y, as in the $Ag^{0.5}Cu^{0.5}$-Y sample. I.e., smaller quantity of copper(II) nitrate than silver(I) nitrate solution is needed to obtain equal weight percentage of the ions in zeolite Y. Interaction between the copper ions and the framework aluminum atom is probably more favorable compared to the silver ion. Higher affinity with copper ions explains why less copper(II) nitrate is needed to obtain the Ag/Cu ratio as in $Ag^{0.5}Cu^{0.5}$-Y.

9.2 XAS results

EXAFS analyses showed that the immediate coordination of copper is changed by simultaneous presence of silver ions in zeolite Y. In presence of copper ions only (sample Cu-Y), one or several of the three-coordinated sites (I', II and/or II') were occupied, while no copper was found to occupy site III, one of the most accessible sites to NO. The situation is changed in presence of silver, where the site III could possibly be occupied by copper. Sites that would normally be occupied by copper ions are probably taken by silver ions. Thus, direction of copper ions to possibly more active and more accessible sites can be accomplished by utilization of the silver co-cation. The exact position of the ions cannot be determined by these results only. More information about copper location can be obtained by examination of aluminum environment in the samples using EXAFS. As mentioned earlier, this was unfortunately not performed in this thesis.

No differences were found for coordination of copper in samples of different copper and silver loading. Thus, to change the coordination of copper in zeolite Y, only a small amount of silver compared to copper is needed.

Yahiro and Iwamoto [1] suggest that the redox properties of copper-zeolites can be attributed to their catalytic activity in the decomposition/reduction of NO_x, where the Cu(I) species participate in the reaction. The redox properties of copper in Cu-Y and $Ag^{0.5}Cu^{0.5}$-Y samples were examined by in-situ XAS, by exposing the samples to hydrogen and subsequently to NO. Thermal treatment in hydrogen leads to elongation of the Cu–O bond in both samples. Same is observed for ion-exchanged ZSM-5 [2]. I.e. reduction of extra-framework copper is not restricted by the surrounding framework.

Two methods were used to find copper valences formed during reduction. Linear combination fit utilizes the pre-edge and XANES region of XAS spectrum, while Vegard's relationship relates the derived bond distanced from EXAFS to valence states of copper. Results from both methods show that Cu(II) in the $Ag^{0.5}Cu^{0.5}$-Y sample is more prone to reduction than copper in the Cu-Y sample. The Cu(I) fraction increased gradually in both samples during the course of thermal treatment in hydrogen. The estimated fractions were higher in $Ag^{0.5}Cu^{0.5}$-Y than Cu-Y; ~ 40 % and ~ 30 % respectively. Higher fraction of Cu(I) in $Ag^{0.5}Cu^{0.5}$-Y can be attributed to location of copper in sites more accessible to hydrogen.

During reduction of Cu(II) in the $Ag^{0.5}Cu^{0.5}$-Y and Cu-Y samples, the most pronounced difference was found in formation of metallic copper. While only small amounts of Cu(0) were present in Cu-Y, a fraction of as much as ~ 40 % was estimated for the $Ag^{0.5}Cu^{0.5}$-Y at the highest temperatures. There are two possible routes for formation of metallic copper; direct reduction of copper(II) (Equation 8-1) or reduction to copper(I) followed by disproportion to Cu(0) and Cu(II) (Equation 8-2)[2]:

$$Cu(II) + 2e^- \rightarrow Cu(0) \qquad (8\text{-}1)$$

$$2Cu(II) + 2e^- \rightarrow 2Cu(I) \rightarrow Cu(0) + Cu(II) \qquad (8\text{-}2)$$

Since significant fractions of Cu(I) were observed in both samples, metallic copper was presumably formed by Equation (8-2). J. Kecht et.al. [3] also deduced that the disproportion reaction is expected to dominate upon reduction of copper in zeolite Y.

At the final temperature stage of hydrogen treatment of $Ag^{0.5}Cu^{0.5}$-Y, multiplicity of the Cu···Cu shell was found to be 5. The metal particles are presumably small nanoclusters. In the Cu-Y sample, 2.3 Cu–O distances of 1.983 Å were found from EXAFS of the highest temperature in reducing environment. From the same EXAFS 2(1) Cu···Cu distances of 2.98 Å were derived. The Cu···Cu distance is considerably stretched with respect to Cu metal (2.56 Å). This is a composite product, and it is likely that the Cu-O bonds arise from an outer shell of oxide covering a metal core. These results are consistent with findings of Mathisen et.al. [4] for a copper ion-exchanged zeotype exposed to reducing environment.

Treating the samples with NO after the hydrogen stage leads to formation of copper oxides. In Cu-Y the fraction of reversed copper(II) is larger than in $Ag^{0.5}Cu^{0.5}$-Y. In the latter, the estimated copper(II) oxide fraction was considerably greater than in Cu-Y. The role of silver to enhance copper(II) oxide formation in oxidizing environment cannot be ruled out. However, to confirm or disprove this presumption requires examination of silver by XAS as well.

The estimated values in the XANES analyses should not be emphasized as “true” values. First of all, the linear combination fitting is a mathematical method, with no concern to logics of chemistry. Second, the R-factor values are high (Table 6.4 and 6.5), which implies bad match between the XANES of reference compounds and XANES of the samples.

9.3 XRD and SEM results

XRD analyses confirmed that the crystallinity of zeolite Y is preserved when heated to 500 °C and treated with H_2 and NO. The framework structure is unaffected by reduction and re-oxidation of the copper species, with no evidence of collapse. These observations are further confirmed by scanning electron micrographs. The characteristic triangular pyramid morphology is apparent for zeolite H-Y, Cu-Y as-prepared, $Ag^{0.5}Cu^{0.5}$-Y as-prepared and $Ag^{0.5}Cu^{0.5}$-Y after the in-situ measurements. The particle size distribution is unchanged when

zeolite H-Y is ion-exchanged and put through thermal and gas treatment. These results confirm the stability of zeolite Y.

9.4 NO_x conversion

Even though XAS showed presence of considerably large Cu(I) fractions, the conversion of NO over $Ag^{0.5}Cu^{0.5}$-Y and Cu-Y samples was very low. The lacking activity might be attributed to several factors. Copper(I) was possibly located at sites inaccessible to NO adsorption. Nanocluster formation in the silver and copper containing sample might have blocked the pores of zeolite Y, thereby inhibiting diffusion of reactants to the surface. A prerequisite for deNO_x activity is stabilization of copper(I) within the structure, together with reversibility of the copper valence state [2]. From the in-situ measurements, significant fractions of copper oxides were estimated to be present at the final stages of NO treatment, which are known to induce inactivity toward the deNO_x reduction [2]. Another reasonable explanation is deactivation of the active sites by carbonaceous deposits on the internal surface. This statement is supported by the change in colour of the samples from light blue as fresh catalysts, to black after the NO_x measurements. Hydrocarbon coking of the active sites is a frequently reported source of deactivation in ion-exchanged zeolites [5].

References

1. H. Yahiro and M. Iwamoto, Applied Catalysis A: General, 2001, **222**, 163-181

2. K. Mathisen, D. Nicholson, A.M. Beale, M. Sanchez-Sanchez, G. Sankar, W. Bras and S. Nikitenko, *J. Phys. Chem*. C, 2007, **111**, 3130-3138

3. J. Kecht, Z. Tahri, V. De Waele, M. Mostafavi, S. Mintova and T. Bein, *Chem. Mater*. 2006, **18**, 3373-3380

4. K. Mathisen, M. Stockenhuber, D.G. Nicholson, Phys. Chem. Chem. Phys., 2009 (DOI: 10.1039/b902491c)

5. S. Bhattacharyya , R. K. Das, Catalytic Control of Automotive NO_x : A Review, *Int. J. Energy Res*.,1999, **23**, 351-369

10 CONCLUSIONS

Based on the results and discussion, the research questions put forth in Chapter 1.3 will here be answered. Taken together, the answers show most importantly, that the site occupation of copper cations in zeolite Y can be altered by silver co-cations. However, the catalysts were demonstrated to be inappropriate for NO_x conversion.

Question 1.1

What is the resulting weight percentage ratio of silver/copper when the silver(I)/ copper(II) solution ratio is varied upon simultaneous cation-exchange in zeolite H-Y?

The ratio of silver(I) nitrate/copper(II) nitrate solutions differs from the resulting silver/copper weight percentage in ion-exchanged zeolite Y. Less copper(II) nitrate than silver(I) nitrate is needed to obtain equal weight percentage of the ions in the zeolite. Interaction between the copper ions and the framework aluminum atom in zeolite Y is probably more favorable compared to the silver ion.

Question 1.2

Will the coordination of copper cations in zeolite Y be influenced by presence of silver co-cation? I.e. will copper cations occupy different sites in zeolite Y in presence compared to absence of silver co-cations? If changed, is the coordination dependent on the copper/silver weight percentage ratio?

EXAFS analyses showed that the immediate coordination of copper is changed by simultaneous presence of silver ions in zeolite Y. In the Cu-Y sample, copper is situated in one or more of the three-coordinated of sites (I', II and/or II'). Location of copper in $Ag^{0.5}Cu^{0.5}$-Y is more difficult. With the multiplicity of 4.6 in the Cu–O shell, assignment of site(s) is not possible on the basis of results in this thesis only. However, copper in the as prepared and calcined $Ag^{0.5}Cu^{0.5}$-Y is most likely situated at three-coordinated sites and the six-coordinated sites, as the average of these is 4.5. The coordination of copper is unaffected by the Ag/Cu weight percentage ratio in $Ag^{x}Cu^{z}$-Y samples. EXAFS results show that only a small Ag/Cu ratio is needed to change the location of copper.

Question 1.3

Do the redox properties of copper in zeolite Y change by presence of silver co-cations?

In-situ XAS results show that reduction of copper is not restricted by the surrounding framework neither in $Ag^{0.5}Cu^{0.5}$-Y nor Cu-Y sample, evident in the elongation of Cu–O bond in reducing environment. Reduction of Cu(II) to Cu(I) occurs in both samples. Estimation of more reduced copper in the $Ag^{0.5}Cu^{0.5}$-Y sample can be attributed to location of copper in sites more accessible to hydrogen.

A significantly larger metallic copper fraction was found in the $Ag^{0.5}Cu^{0.5}$-Y sample at the highest temperatures in reducing environment. From the multiplicity of 5 in the Cu⋯Cu shell, nanocluster formation is presumed. Under the same conditions for the Cu-Y sample, an oxide layer covering a metal core is assumed to be present. The disproportion reaction is expected to be the route for Cu(0) formation.

Exposing the samples to NO after hydrogen treatment leads to formation of copper oxides, more so in the $Ag^{0.5}Cu^{0.5}$-Y than in Cu-Y sample. In the latter, a larger fraction of reversed Cu(II) is found.

Question 1.4

Is the crystallinity and particle size of the ion-exchanged zeolite Y itself influenced by thermal treatment in reducing and oxidizing environments?

The structure and particle size distribution is unaffected of thermal and gas treatments. Thus, the stability of zeolite Y is confirmed.

Question 2.1

Is the catalytic activity for selective reduction of NO_x in presence of hydrocarbons (SCR-HC) improved by simultaneous presence of copper and silver in zeolite Y, compared to zeolite Y containing only copper?

The conversion of NO is very poor for both the samples. Thus, the co-cation effect does not improve catalytic activity towards NO reduction.

Question 2.2

Is the copper and silver ion-exchanged zeolite Y sufficiently active and durable to be considered for practical applications?

The low activity of the catalysts is most probably formation of copper oxides, and/or hydrocarbon coking of the active sites. The copper and silver containing zeolite Y are not considerable for practical applications.

11 FUTURE WORK

Even though the Cu-Y and $Ag^{0.5}Cu^{0.5}$-Y yield low conversion of NO_x, the finding of the changed coordination of copper in presence of silver is very important. It shows that it is possible to direct copper to other sites in zeolite Y, which would not be occupied by copper in absence of silver. To obtain more information on where copper is situated in the $Ag^{0.5}Cu^{0.5}$-Y, XAS should be used to investigate environment of the aluminium atoms in the zeolite. Incidentally, such investigation could also give information about the silver cations in $Ag^{0.5}Cu^{0.5}$-Y.

In order to correlate the hydrogen quantity for the reduction of copper in the samples, temperature programmed reduction (TPR) could possibly give useful results. Characterization by TPR was planned in this thesis, but was not available at the scheduled time.

Zeolite Y is just one of the 150+ different synthetic zeolites. The Ag^xCu^z combination might improve the catalytic activity when applied to other zeolites.

APPENDIX A

An example of copper valence fraction calculations by Vegard relationship

The values in this example are taken from Table 6.9 at the H_2 (500) stage. The Vegard relationship:

$\mathbf{R_{Cu(I)}\, x + R_{Cu(II)}\, (1 - x) = R_{EXAFS}}$

$R_{Cu(I)} = 2.00$ Å

$R_{Cu(II)} = 1.948$ Å

$R_{EXAFS} = 1.993$ Å

$2.00\ x + 1.948\ (1 - x) = 1.993$

x = 0,865 (Cu(I) fraction)

(1 – x) = 0,135 (Cu(II) fraction)

$2\ x + 4.6\ (1 - x) = N_{Theory} = 2 \cdot 0{,}865 + 4.6 \cdot 0{,}135 = 2.351$

$(N_{Theory} / N_{EXAFS}) - 1 = y = (2.351/1.5) - 1 =$ **$(Cu^0$ fraction) = 0.57**

(1-0.567) 100 = 0,433 = The rest

43.3 · 0.865/ 100 = 0.37 (Cu(I) fraction)

43.3 · 0.135/ 100 = 0.6 (Cu(II) fraction)